NTNU

Norwegian University of
Science and Technology

Improving Elastography using SURF Imaging for Suppression of Reverberations

Jørgen Grythe

Master of Science in Communication Technology

Submission date: February 2010

Supervisor: Ilangko Balasingham, IET
Co-supervisor: Svein-Erik Måsøy, ISB
Thor Andreas Tangen, ITK

Norwegian University of Science and Technology
Department of Electronics and Telecommunications

Problem Description

As difference in elasticity of tissue give rise to different tissue displacements, and hence different time shifts in the recorded radio frequency (RF) signals, these time shifts can be estimated and hence produce an ultrasound image of tissue with different elastic properties, also known as an elastogram. When estimating the tissue displacement, a window around the sample in range is used to improve the estimate. Most methods assume a constant displacement over this window while in fact the degree of local stretching and compression can be substantial and can degrade the estimates. An estimator for estimating locally variable delays has been developed which is a phase based approach and makes no assumption on the local delay variation. The method uses the phase difference and an estimate of the instantaneous frequency of the IQ demodulated signal, and has then the advantage of being able to locally represent delays in terms of phase difference. Any parametric model may be used to model the local delay variations, and for this thesis the first step has been in adapting the time-delay algorithm for elastography purposes, and examine the effects different parametric models have on the final image quality.

Secondly, multiple reflections, also known as reverberations, greatly impair the contrast resolution of the final image, as they appear as additive noise at deeper depths than their true originals are located. Also the estimation of time delays, which is critical for elastography, may be greatly reduced by these reverberations. The SURF Imaging method may be used to suppress these strong reflections. For this thesis it has been the main goal of using the phase based time delay algorithm, combined with SURF imaging with reverberation suppression, and prove the quality this approach has in reducing the effects of reverberations on the recorded RF signal, and then increase the quality of elastography recordings compared to other methods available at the time. This purpose then give the name of the paper as "Improving Elastography using SURF Imaging for Suppression of Reverberations".

Assignment given: 03. September 2009
Supervisor: Ilangko Balasingham, IET

The more you explain it, the more I don't understand it
- Mark Twain

Abstract

For some of the applications of the Second-order UltRasound Field (SURF) imaging technique, a real-time delay-estimation algorithm has been developed for estimating spatially range-varying delays in RF signals. This algorithm is a phase-based approach for subsample delay estimation, and makes no assumption on the local delay variation. Any parametric model can be used for modeling the local delay variation. The phase-based delay estimator uses estimates of the instantaneous frequency and the phase difference and the relationship between the two to estimate the delay. The estimated delay may be used to calculate an improved estimate of the instantaneous frequency, which in turn may be used to calculate new, updated values for the delay using an iterative scheme. Although an iterative scheme introduces a larger bias, the estimated delay values have a significantly lowered standard deviation in comparison to the original method. The delay estimator originally developed for estimating propagation delays for SURF imaging, can also be used for elastography purposes. By not being restricted to locally constant delays, the delay estimator is able to more robustly estimate sharp changes in tissue stiffness, and in estimating small differences in strain more closely. Two different parametric models for the local delay have been tried, one linear, and one polynomial of the first degree. The two various models have been tested on an elastography recording provided by the Ultrasonix company (Ultrasonix Medical Corporation, Vancouver, Canada), and in vitro. Using a polynomial of the second degree as parametric model for the delay is better than a linear model in detecting edges of inclusions located at a depth where the strain is lower than closer to the transducer surface. The differences may be further emphasized by performing spatial filtering with a median filter. The downside of updating the model is an increased computational time of $\sim 50\%$.

Multiple reflections, also known as reverberations, appear as acoustic noise in ultrasound images and may greatly impair time-delay estimation, particularly in elastography. Today reverberation suppression is achieved by second harmonic imaging, but this method has the disadvantage of low penetration, and little or no signal in the near field. The SURF imaging technique has the advantages of reverberation suppression in addition to imaging in the fundamental frequency. A reverberation model has been established, and the effect reverberations have on estimated elastography images is studied. When using a layered silicon plate as reverberation model, and imaging through this initial reverberation model placed on top of the imaging phantom, elastography images were not obtained as the quality of the recording was degraded as a result of power loss. By adding reverberations by computer simulations after a recording with a SURF probe with reverberation suppression was performed, a markedly difference between elastography estimates done on the image with reverberations, and the image with reverberations and reverberation suppression was observed. Estimating on a signal with reverberations, the phase-based time-delay algorithm was unable to distinguish any differences in elasticity at all. Estimating time delays on a signal with reverberations and SURF reverberation suppression however, the algorithm was able to clearly estimate differences in strain, and display the presence of an inclusion.

Preface

This report is the result of my master thesis at the Department of Electronics and Telecommunications (IET) of the Faculty of Information Technology, Mathematics and Electrical Engineering (IME) of the Norwegian University of Science and Technology (NTNU). It was supervised by Professor Bjørn A.J. Angelsen and co-supervised by Post. Doc Svein-Erik Måsøy and Ph.D. Thor Andreas Tangen. All work was carried out at the Department of Circulation and Medical Imaging (ISB) of the Faculty of Medicine (DMF). The report describes theoretical considerations, computer simulations and laboratory work carried out from September 2009 to February 2010.

The graduating class of 2009 of the 5-year Master of Science in Communication Technology at NTNU existed of 42 individuals - of which exactly one chose the specialization of Signal Processing in Medical Applications. Coming from a background focusing mainly on telematics and communication, this specialization choice had the effect of a rather harsh first encounter the fall of 2007 with the very first lesson on medical ultrasonography being on the complex inhomogeneous non-linear wave equation in 3D space. But also the added perks of being able to choose my project thesis and master thesis as I saw fit, in addition to getting my very own office - a room with a view nonetheless - at the 4th floor of the Medical Technical Research Centre. Coming from a certain background, it soon became clear to me that one can not really study medical ultrasound as one homogeneous subject, but rather as different fields intertwined. Fields such as mathematics, physics, acoustics, signal processing, computer programming, medicine, physiology and electronics, all within the framework of imaging organs beneath the skin using high frequency sound. In order to understand the various theoretical aspects, perform my own research and develop solutions and results, it has then been of importance to acquire knowledge and skills beyond that of my own study program. This has been a process over the last two years that has involved a lot of reading, a lot of thinking, and first and foremost, a lot of questions. Being situated at St. Olavs hospital far from my classmates, I have been so fortunate as to become part of the people who compose the ultrasound technology group at the Department of Circulation and Medical Imaging. Among which I have been able to learn from, and work in close collaboration with, some of the most talented and experienced individuals within the field of medical ultrasound technology. In addition to their extensive knowledge on all the different aspects of medical ultrasound, they have also been a great inspiration and help.

Acknowledgments

Thanks to Prof. Bjørn A.J. Angelsen for getting me interested in medical ultrasound in the first place by attending his course in medical imaging during the fall of 2007. Also I greatly appreciate him allowing me to conduct my project under his supervision. Svein-Erik Måsøy's enthusiasm

since the very beginning of my career at the department has been a great motivational factor for me. His ability of explaining the complex areas of ultrasound in a down to earth language easily understandable has also been invaluable. By always being available for assistance, showing such great interest in my work, and always being of high spirits, he has been one of the main factors for my well-being while working on my thesis. Thor Andreas Tangen eats C and Matlab code for breakfast, and compiles them while taking lunch. He has been the person to turn to whenever I can't figure out strange and unexplainable artifacts appearing in my simulations. He has also been the one to go to whenever I needed a physical, easily explainable, drawing of the solutions to my questions concerning the thesis - on top of a quick mathematical proof of course. Thanks goes out to Prof. Hans Torp for being kind enough to let me come on board for a summer job at the department in June and July of 2008. Also it was of great interest for me in taking part in his course in signal processing in medical imaging during the spring of 2008, and the advanced course during the fall of 2009. Torbjørn Hergum must be mentioned as he probably was the first person that made me understand what the mathematical formulas describing the different aspects of ultrasound really meant in the physical world, and thus helped me reach a higher degree of understanding. As I started working on my summer job and later my thesis, he has also always been available when I have problems figuring out how to get my Macbook Pro functioning properly, in addition to his extensive knowledge of unix commands. And last, but certainly not least, thanks to all the fantastic people I have met during these five years being a student in Trondheim, some of whom I have come to consider close personal friends. Their constant encouragement and friendship has been a great support that has made the motivationally challenging moments in rainy Trondheim go by much easier.

Trondheim
February 3, 2010

Jørgen Grythe

Contents

1 Introduction **1**
- 1.1 Background . . . 1
- 1.2 Motivation . . . 4
- 1.3 Purpose of this study . . . 4
- 1.4 Structure of this paper . . . 5

2 Estimation and tracking of locally variable delays **7**
- 2.1 Phase-based time-delay estimation . . . 7
  - 2.1.1 Signal model . . . 7
  - 2.1.2 Estimation of the phase difference ψ . . . 8
  - 2.1.3 Estimation of the instantaneous frequency θ . . . 9
  - 2.1.4 Modeling and finding the delay τ . . . 9
- 2.2 Linear least squares . . . 10
  - 2.2.1 The general case . . . 11
  - 2.2.2 Weighted least squares . . . 11
  - 2.2.3 $f(x_k, \beta)$ as a linear model . . . 12
  - 2.2.4 $f(x_k, \beta)$ as a polynomial of second order . . . 13
- 2.3 Linear least squares for phase-based time-delay estimator . . . 14
  - 2.3.1 The general case . . . 14
  - 2.3.2 Weighted least squares . . . 15
  - 2.3.3 $\hat{\tau}$ as a linear model . . . 16
  - 2.3.4 $\hat{\tau}$ as a polynomial of second order . . . 17
- 2.4 Differences in modulating phase when estimating θ and ψ . . . 18
- 2.5 Iterative scheme to find optimal values of the instantaneous frequency . . . 20
- 2.6 Analytical characterization of instantaneous frequency iteration algorithm . . . 22

3 Estimating tissue elasticity **29**
- 3.1 Sonoelasticity imaging . . . 29
- 3.2 Transient elastography . . . 30
- 3.3 Elastography . . . 30
- 3.4 Relations of tissue displacement and tissue elasticity . . . 32

4 Impacts on elastogram quality for linear and nonlinear model of $\hat{\tau}$ **35**
- 4.1 Choice of window length for phase based estimator . . . 36
- 4.2 Comparison of linear and non-linear model of $\hat{\tau}$ used on elastography data . . . 38
- 4.3 Improved noise suppression and edge detection by use of median filter for spatial filtering . . . 43

5 SURF imaging **47**

5.1 Principles of SURF imaging . . . 47
5.2 Homogeneous linear wave equation . . . 48
5.3 Nonlinear wave propagation . . . 49
5.4 Homogeneous nonlinear wave equation . . . 51
5.5 Sound propagation and time delays as a function of acoustic pressure . . . 53

6 Reverberations **57**
6.1 Theory of multiple scattering . . . 57
6.2 Reverberation classes . . . 58
6.3 Mimicking multiple reflections . . . 59
6.3.1 Bacon as reverberation model . . . 59
6.3.2 Water and silicon plate as reverberation model . . . 60
6.3.3 Computer simulations of reverberations . . . 60
6.4 Effects of reverberations on recorded B-mode images . . . 61
6.5 Effects of reverberations on estimated elastography images . . . 61

7 Reverberation suppression capabilities of SURF **63**
7.1 Signal model without reverberation suppression . . . 63
7.2 Reverberation suppression method of SURF imaging . . . 63
7.3 Signal model with reverberation suppression . . . 65

8 Effects of reverberations and reverberation suppression in elastography images **67**
8.1 Elastography recordings made with a 7.5 MHz Ultrasonix transducer . . . 67
8.2 Elastography recordings made with 6.5 MHz SURF transducer "Viglen" . . . 69
8.3 Elastography recordings made with 6.5 MHz SURF transducer "Viglen" with reverberation suppression . . . 71
8.4 Introducing reverberations in the signal, and the effect of reverberation suppression for B-mode and elastography images . . . 73
8.5 Elastography images computed from in vivo recordings of the lower arm . . . 77

9 Discussion **79**

10 Conclusion **81**

11 Further work **83**

Appendix A Matlab code for phase-based time-delay estimator **85**

Appendix B Matlab code for making elastogram **89**

Bibliography **93**

List of Figures

2.1 Inaccurate estimate of the time delay τ found by dividing the phase difference ψ by the instantaneous frequency θ . . . 10
2.2 Fitting data points by the linear least squares method with a linear model 13
2.3 Fitting data points by the linear least squares method with a non-linear model . 14
2.4 Correct estimate of the time delay τ found from the phase based approach choosing a linear model of $\hat{\tau}$ within a window of length 3.4 mm . . . 17
2.5 Difference of the derivate of the modulating phase $\varphi_1'(k)$ and $\varphi_2'(k)$ when estimating phase difference and the instantaneous frequency . . . 19
2.6 Interpolation scheme to determine non-existing values at the start of the estimated time delay . . . 22
2.7 Difference of the derivate of the modulating phase $\varphi_1'(k)$ and $\varphi_2'(k)$ when estimating phase difference and the instantaneous frequency after one iteration of the minimum phase difference algorithm . . . 23
2.8 Maximum detectable delay in nanoseconds as a function of center frequency when estimating with the phase-based time-delay estimator . . . 24
2.9 Two RF signals delayed in respect to each other with linearly increasing delay and center frequency $f_c = 7$ MHz, sampling frequency $f_s = 40$ MHz and 50% relative bandwidth . . . 24
2.10 Maximum estimated delay by the phase-based time-delay estimator as a function of the actual delay for linear and polynomial model. Simulated with center frequency $f_c = 7$ MHz, sampling frequency $f_s = 40$ MHz, 50% relative bandwidth and $n = 1000$. . . . 25
2.11 Bias and standard deviation for linear and polynomial model when estimated by the phase-based time-delay estimator as a function of the actual delay. Simulated with center frequency $f_c = 7$ MHz, sampling frequency $f_s = 40$ MHz, 50% relative bandwidth and $n = 1000$. . . . 25
2.12 One sided normalized frequency spectrum of a band limited signal with Nyquist limits f_N and various minimum sampling frequencies $f_{s,min}$ for various bandwidths. Simulated with center frequency $f_c = 7$ MHz, sampling frequency $f_s =$ 40 MHz, 50% relative bandwidth. . . . 26
2.13 Maximum estimated delay by the phase-based time-delay estimator using a linear model as a function of the actual delay for different bandwidths and sampling frequencies. Simulated with center frequency $f_c = 7$ MHz and 50% relative bandwidth. 27
2.14 Bias and standard deviation in samples by the phase-based time-delay estimator using a linear model as a function of the actual delay for different bandwidths and sampling frequencies. Simulated with center frequency $f_c = 7$ MHz and 50% relative bandwidth. . . . 28

3.1 Basic principle behind elastography [1] . . . 31

3.2 Cross-correlation within a sample window between two different frames . The peak of the function will yield the corresponding time delay 32
3.3 Elastogram made by using the phase-based time-delay algorithm with a non-linear model of $\hat{\tau}(k)$ as described by Eq. (2.60) within a window of size 3.4 mm. Recording made with a 10 MHz probe and a demodulation frequency of 6 MHz . 33

4.1 CIRS Model 049 ultrasound phantom used for elasticity imaging [2]. The phantom contains several spheres of different sizes and elasticity. The spheres will appear isoechoic to the background using conventional B-mode imaging 35
4.2 Elastogram made with different window lengths ranging from 2.2 mm to 4.4 mm. Recorded with a 10 MHz probe and a demodulation frequency of $f_d = 6$ MHz. Strain values estimated with a linear model for $\hat{\tau}(k)$ 36
4.3 Elastogram made with window lengths ranging from 3.8 mm to 6.0 mm. Recorded with a 10 MHz probe and a demodulation frequency of $f_d = 4$ MHz. Strain values estimated with a linear model for $\hat{\tau}(k)$ 37
4.4 Number of wavelengths as a function of window length in millimeter for fixed frequency of 6 MHz and 4 MHz, and window length in millimeter as a function of demodulation frequency, both with fixed speed of sound as 1540 m/s 37
4.5 Computational time as a function of window length for the phase-based time-delay algorithm with a linear model. The first data-set consists of 30 frames with a demodulation frequency $f_d = 6$ MHz, whereas the second data-set consists of 50 frames with a demodulation frequency $f_d = 4$ MHz 38
4.6 Sequence of frames from estimated elastogram with a linear model of $\hat{\tau}(k)$ (top row), and a polynomial model of $\hat{\tau}(k)$ (bottom row) 39
4.7 Various region of interests for elastogram estimated by a linear model (top row), and a polynomial model (bottom row). The first ROI displays how the two different models adapt to noise, whereas the last two ROIs displays edge detection for the two models 40
4.8 Estimated time delay $\tau(k)$, local rate of change ε, and final elastogram values for a single line through the image from top to bottom for the two different models of $\hat{\tau}(k)$ 41
4.9 Final elastogram values for a single line through the image from top to bottom for the two different models of $\hat{\tau}(k)$ 42
4.10 Sequence of frames from estimated elastogram with a linear model of $\hat{\tau}(k)$ (top row), and a polynomial model of $\hat{\tau}(k)$ (bottom row) and both sequences filtered by a median filter 43
4.11 Various region of interests for median filtered elastogram estimated by a linear model (top row), and a polynomial model (bottom row). The first ROI displays how the two different models adapt to noise, whereas the last two ROIs displays edge detection for the two models 44
4.12 Various regions of interest for median filtered elastogram estimated by a polynomial model. The first ROI displays the inclusion on the top right, the second ROI displays the inclusion on the bottom left, and the third ROI displays the inclusion on the bottom right 45
4.13 Computational time as a function of window length for the same data-set and for two models of $\hat{\tau}(k)$. The computational time for a polynomial model of the first degree is displayed in red, and the computational time for the linear model is displayed in blue 45

5.1 Illustration of two different SURF-pulse complexes with the high-frequency imaging pulse first placed in a compression phase of the low-frequency manipulation pulse, and then in a rarefaction phase 47
5.2 Effects of nonlinear propagation; distortion of the acoustic waveform, and the generation of components at harmonic frequencies of the fundamental [3] 49
5.3 Estimated time-delay by the phase-based time-delay estimation algorithm from the most basic SURF pulsing scheme; a two-pulse setting with the imaging pulse first placed in a compression phase of the manipulation pulse, and then in a rarefaction phase 54

6.1 Physical structure of the body wall consisting of layered tissue close to the skin, and irregular mixtures of muscles, fat and connective tissue. 57
6.2 Direct wave propagation (upmost path) and reverberations of class 1, 2, and 3 (2nd to 4th path). Figure adapted from [4] 58
6.3 Tissue from a pig as reverberation model 59
6.4 Imaging on phantom with bacon as reverberation model 60
6.5 Silicon plate as reverberation model 60
6.6 Simulating reverberations in Matlab 61
6.7 B-mode image of phantom with and without reverberation model 61
6.8 Elastography recordings with Ultrasonix method with reverberations 62

7.1 On axis pressure field from SURF and ordinary ultrasound pulse 65

8.1 Frequency spectrum of RF data recorded with a 10 MHz Ultrasonix probe and a sampling frequency $f_s = 40$ MHz. FIR bandpass filter with cut-off frequencies of 2.5 and 9 MHz is plotted in red, and the filtered spectrum of the RF signal is plotted in green 68
8.2 Ordinary B-mode image, estimated time delay values, strain rate values, and elastogram made with a 7.5 MHz Ultrasonix probe, a frame rate of 27 Hz and a demodulation frequency $f_d = 5$ MHz. Time delay values were estimated by a linear model of $\hat{\tau}$ within a window size of 4.1 mm 68
8.3 Estimated time delay values in nanoseconds, local rate of change, i.e. strain rate values, and final elastogram values for a single line running from top to bottom of a single frame as seen in the second, third an fourth frame of Figure 8.2 69
8.4 Frequency spectrum of RF data recorded with a 6.5 MHz SURF probe "Viglen" and a sampling frequency $f_s = 40$ MHz. FIR bandpass filter with cut-off frequencies of 3 and 9 MHz is plotted in red, and the filtered spectrum of the RF signal is plotted in green 70
8.5 Ordinary B-mode image, estimated time delay values, strain rate values, and elastogram made with a 6,5 MHz SURF probe "Viglen", a frame rate of 26 Hz and a demodulation frequency $f_d = 6$ MHz. Time delay values were estimated by a linear model of $\hat{\tau}$ within a window size of 3.4 mm 70
8.6 Estimated time delay values in nanoseconds, local rate of change, i.e. strain rate values, and final elastogram values for a single line running from top to bottom of a single frame as seen in the second, third an fourth frame of Figure 8.5 71
8.7 Frequency spectrum of RF data recorded with a 6.5 MHz SURF probe "Viglen" and a sampling frequency $f_s = 40$ MHz. FIR bandpass filter with cut-off frequencies of 3 and 9 MHz is plotted in red, and the filtered spectrum of the RF signal is plotted in green 72

8.8 Ordinary B-mode image, estimated time delay values, strain rate values, and elastogram made with a 6.5 MHz SURF probe "Viglen", a frame rate of 26 Hz and a demodulation frequency $f_d = 6$ MHz. Time delay values were estimated by a linear model of $\hat{\tau}$ within a window size of 3.4 mm 72
8.9 B-mode image of CIRS model 050 near field phantom [5] with reverberation model applied. Ordinary B-mode image on the left hand side, and reverberation suppression processed image on the right hand side 73
8.10 Frequency spectrum of RF data recorded with a 6.5 MHz SURF probe "Viglen" and a sampling frequency $f_s = 40$ MHz. FIR bandpass filter with cut-off frequencies of 3 and 9 MHz is plotted in red, and the filtered spectrum of the RF signal is plotted in green. Recording made with reverberation model applied to the phantom 74
8.11 Ordinary B-mode image, estimated time delay values, strain rate values, and elastogram made with a 6.5 MHz SURF probe "Viglen", a frame rate of 26 Hz and a demodulation frequency $f_d = 6$ MHz. Time delay values were estimated by a linear model of $\hat{\tau}$ within a window size of 3.4 mm. Recording done with both reverberation model and reverberation suppression 74
8.12 Ordinary B-mode image, image with simulated reverberations, image with simulated reverberations and reverberation suppression. 75
8.13 Ordinary B-mode image and corresponding elastogram, same frame with simulated reverberations and elastogram with reverberations, and same frame with simulated reverberations and reverberation suppression and corresponding elastogram. Recorded with a 6.5 MHz SURF probe "Viglen". FIR bandpass filtered with cut-off frequencies of 3 and 9 MHz. Frame rate 26 Hz, and demodulation frequency $f_d = 6$ MHz. Time delay values were estimated by a linear model of $\hat{\tau}$ within a window size of 3.4 mm 76
8.14 Transversal recording on the lower arm with estimated strain values on the left hand side, and the ordinary B-mode image on the right hand side. Recording made with a 7.5 MHz Ultrasonix transducer, and filtered by a FIR bandpass filter with cut off frequencies of 3 MHz and 9 MHz. Data demodulated with a demodulation frequency $f_d = 6$ MHz. Time delay values were estimated by a linear model of $\hat{\tau}$ within a window size of 3.4 mm 77

List of Tables

2.1 Various bandwidth parameters when simulating with a center frequency $f_c = 7$ MHz 27

5.1 Nonlinearity parameter β_n and other acoustic parameters for typical soft tissues [6] 51
5.2 Theoretical values of time delays in nanoseconds per centimeter as a function of manipulation pressure assuming $\beta_n \backsim 5$, $\kappa \backsim 450 \cdot 10^{-12}$ Pa^{-1} and a constant sound velocity of $c = 1540$ m/s 55

6.1 Reverberation classes with total path length $2z_i$ in all cases. Adapted from [4] . . 59

List of Abbreviations

DMF	Faculty of Medicine, page iii
FIR	Finite Impulse Response, page 67
HF	High Frequency, page 47
IET	Department of Electronics and Telecommunications, page iii
IME	Faculty of Information Technology, Mathematics and Electrical Engineering, page iii
ISB	Department of Circulation and Medical Imaging, page iii
LF	Low Frequency, page 47
NTNU	Norwegian University of Science and Technology, page iii
RF	Radio Frequency, page 4
ROI	Region Of Interest, page 31
SNR	Signal-to-Noise Ratio, page 32
SONAR	Sound Navigation And Ranging, page 1
SURF	Second-order UltRasound Field, page 47
TDE	Time Delay Estimation, page 7
THI	Tissue Harmonic Imaging, page 2
WLS	Weighted Least Squares, page 10

Chapter 1

Introduction

1.1 Background

According to naval terms, "to sound" means to measure the depth of water at sea. The ancient Greeks probed the depths of seas with a "sounding machine", which was a long rope knotted on regular intervals with a lead weight at the end. Recalling his experiences working on Mississippi riverboats as a young man, American author and humorist Samuel Clemens chose his pseudonym Mark Twain from the second knot on such a line, where two fathoms, a depth indicating safe water for passage of boats, was measured on the sounding line. These lines were widely used in navigation until the development of echo sounding, from which the words "to sound" set the basis for the use of actual sound for the same purpose.

A young, healthy human is capable of hearing sounds over the frequency range of 20 Hz to 20 kHz, with this upper frequency limit for humans caused by the middle ear, which acts as a low-pass filter. An ultrasound wave describes an acoustic wave with a frequency above this threshold of human hearing, and ultrasonics have already been in use for thousands of years in the natural world by animals such as bats and dolphins. Bats are for instance known to emit pulses in the 30 kHz to 120 kHz range, and it has been hypothesized that they judge range by sensing the time delay between an emitted ultrasound pulse and the echo. This principle of detecting objects based on the time delay and strength of the echo would first be exploited by humans after the sinking of the Titanic in 1913. Within a month of the accident a patent to detect icebergs with underwater echo ranging was filed, and the development of sound navigation and ranging (SONAR), which is the basis for ultrasound for medical purposes, can be traced back to this incident. In the late 1940s and early 1950s new emerging technological advances paved way for the use of ultrasound applied to the human body, and a new world of possibilities for medical diagnosis was born. In Sweden in 1953, Dr. I. Edler and Professor C. H. Hertz detected heart motions, and began what later was called "echocardiography", the application of ultrasound to characterize and image the heart [7]. In 1955 experiments with Doppler-shifted ultrasound signals produced by heart motion were reported, and by 1966 pulsed spectral Doppler was possible. In the early 1980s color flow imaging techniques for visualizing the flow of blood in real time were developed [8], and many other signal processing methods for imaging and calculation became available. During the 1980s transducer technology underwent tremendous growth, and concurrently sonar systems evolved to such a point that the Titanic was discovered at the bottom of the sea with sonar and video equipment in 1986 [9]. Around this period a technique which injects the blood with gas filled micro bubbles with a typical diameter of a

few microns, so called contrast agents, were introduced to enhance the ultrasound images. As the nonlinear nature of bubble dynamics introduces nonlinear distortion, this also produces harmonic (and subharmonic) energy in the propagating signal. This effect was then exploited by filtering out the second harmonic component of the received pulse, which is narrower and has lower sidelobe levels than the fundamental beam, making it ideal for imaging purposes. An interesting discovery was made when it turned out that ordinary ultrasound images also experienced a vastly improved image contrast when imaging in the harmonic frequency, and a new technique known as tissue harmonic imaging (THI), or simply harmonic imaging, was born [10, 11]. By the late 1990s, near real-time three-dimensional imaging became possible due to the emergence of special image-processing techniques and the advances in computer processing capabilities. With further development in computer science and electronics, miniaturization of ultrasound equipment has become a reality, and the first hand-held ultrasound device weighing in at just 390 grams was made commercially available at the start of 2010. Due to the advantages of being cheap, fast, relatively low-tech, non-invasive, harmless and more portable than other techniques, it is likely that medical ultrasound technology will continue to have an impact in the future.

Since the early beginnings of medical practice, the estimation of tissue hardness has been practiced through palpation, i.e. the act of feeling or pushing on various parts of a patient's body to determine medical conditions. Palpation has been an important tool to detect abnormalities in the body, mainly because the mechanical properties of diseased tissue are typically different than that of the healthy tissue surrounding it. A tumor or a suspicious cancerous growth is normally much stiffer than the background of normal soft tissue [12]. The basic relationship between tissue elasticity and hardness to palpability then follows the relationship that in order to be palpable, the object must be harder than the tissue surrounding it. However in many cases despite the differences in stiffness, the small size of a pathological lesion makes it harder to detect, and lesions located at deeper depths than the fingers are able to to sense preclude its detection and characterization. Palpation is then limited to the detection of abnormalities and tumors which are close to the skin. Ordinary ultrasound has the advantage of imaging deep inside the body, but is virtually unable to differ between tissue of various hardness and elasticity, and there has been a consistent interest in tissue hardness, motion and vibration over the years.

As early as 1952 Oestreicher et. al. studied the physics of vibration in soft tissue, showing that impedance of tissue increases with frequency over audio frequencies [13]. Initial experiments in differentiating between normal soft tissues and hard lesions using ultrasound were conducted around 1986, but it was not until Lerner et. al. presented a method named "sonoelasticity imaging" in 1989 the concept had any practical implications [14, 15]. The method consisted of mechanical inducing tissue with low frequency (20 - 1000 Hz) acoustic vibrations in the audible range, and measure and display the corresponding Doppler spectrum of various regions within the tissue. Since the velocity of propagation is a function of the elastic properties of tissue, measurement of the velocity of a propagating mechanical vibration in tissue will yield the differences in elasticity. The concept is that stiff tissues will respond differently to an applied mechanical vibration than normal tissue. Areas, or tissue, of increased stiffness will experience less or decreased vibrations which can be seen as a "void" in the Doppler sonoelasticity image. The main advantage of this technique is the ability to view the in vivo results in real time, as the signal processing involved is basically equivalent to already well established Doppler methods.

The term "elastography" was coined by Ophir et. al. in 1991 as a quantitative method of imaging

the elasticity of biological tissue by direct imaging of the strain and the Young's modulus of tissue [16]. Up until this point displacement of tissue were analyzed by doppler velocity measurements, cross-correlation techniques to quantify motions in tissues, and visual inspection of M-mode and B-mode images. One of the main difficulties in these methods was the lack of definition of the magnitude and direction of the driving force, which limited the ability of the methods to provide quantitative information about the elastic properties of the tissue under investigation. The elastography method is based on external tissue compression, with subsequent computation of the strain profile along the transducer axis, and differs in other methods in several important aspects. The force applied to the tissue is not vibratory, but rather considered quasi-static, thus reducing the complexity of the generalized viscoelastic equation of forced motion to the much simpler Hook's equation. The average levels of strain evoked in the tissue are very small, and perhaps most importantly, elastography is capable of producing high resolution images [17]. The strain is derived by analysis of pre-compression and post-compression A-line pairs, and several techniques are available for estimating the displacement in tissues. It is for instance possible to estimate displacement in soft tissues by analyzing the degree of correlation that remains between the pre-compression and post-compression signals after the displacement has occurred. A second similar approach is to estimate the actual time delay by estimating the shift of the peak of the cross-correlation function. However when the signal-to-noise ratio (SNR) is low, the probability of making errors in the estimation of the peak increases dramatically. Also another disadvantage using cross-correlation techniques include the sensitivity of cross-correlations to amplitude variations in the presence of small signal distortions. A different approach is to use the phase of the two signals to compute the delay. Wilson and Robinson described a method for phase tracking of wideband ultrasonic signals as early as 1982, and were able to measure displacement and deformation waveforms for displacements less than 0.1 cm [18]. At the start of 2008, Lindop et. al. presented a theoretical analysis and experimental results from an investigation of phase-based ultrasonic deformation estimators [19]. They were able to demonstrate their application to in vivo freehand strain imaging, and showed quantitatively that the approach offered a wider range of scanning conditions than adaptive methods based on correlation coefficients or sum of absolute differences.

A different approach called transient elastography was presented by Sandir et. al. in 1999 [20]. This method relies on the observation of the propagation of a transient, i.e. pulsed, shear wave to determine the elastic properties of tissue. The local shear wave speed is directly linked to the local Young's modulus of the medium, and a shear elasticity map of the medium may be computed using an inversion algorithm. Because the shear waves propagate through the medium in less than 0.1 s, the displacements induced by the shear wave are measured with an ultrasonic array connected to an ultrafast imaging system able to reach frame rates up to 6000 Hz. Transient elastography then has the advantages of being insensitive to patient motion and boundary condition artifacts because of its real-time capabilities with an acquisition time in less than 20 ms [21]. Bercoff et. al. demonstrated in vivo breast tumor detection using transient elastography in 2002 [22], thus reporting the first in vivo validation of the method. However, the patients chosen had tumors that were palpable (usually more than 15 mm in diameter) and visible on echographic scans. A different technique with close resemblance to transient elastography known as supersonic shear imaging (SSI) was presented by Bercoff et. al in 2004 [23]. In SSI the source radiates low-frequency shear waves inside the tissue, but makes the shear source move with supersonic speed to create quasiplane shear waves of stronger amplitude. Such a shear source which moves faster than the shear waves can be created by successively focusing the ultrasonic "pushing" beam at different depths. All resulting shear waves will interfere constructively along a Mach cone, creating two intense quasiplane shear

waves propagating in opposite directions.

1.2 Motivation

Malignant tumors are generally present as hard nodules, e.g. scirrhous carcinoma of the breast [12]. Although this type of lesion constitutes about three fourths of all breast cancer, other type of breast cancers are soft, and may not be detected by palpation alone, which suggests a need for other quantitative methods such as elastography. Since the echogenicity and the stiffness of tissue are generally uncorrelated, it is expected that imaging tissue stiffness will provide new information that is related to tissue structure and pathology. Elasticity imaging has for instance been reported to be useful for the diagnosis and characterization of various tumors, which are usually stiffer than normal tissue [24]. For example, tumors of the prostate or the breast may be invisible or barely visible in standard ultrasound examinations, yet are much stiffer than the surrounding tissue [25]. However, ultrasound elastography as a potential new imaging technology for breast cancer detection has been classified by the American cancer society as "preclinical data suggest possible promise, but clinical data are sparse or nonexistent, and more study is needed" [26]. This may suggest that taking the leap from the laboratories into the physical world for elastography imaging modalities still presents a great challenge. It is likely that one of the main obstacles is the added complexity of the irregular mixtures of muscles, fat and connective tissue of the body wall, which presents a source of image artifacts known as multiple scattering or reverberations. Reverberations are especially visible in the near field and imaging through the body wall due to the layered structure of the tissue close to the skin, and the presence of these reverberations is a source of artifacts that can hinder the correct analysis of ultrasound signals and images. Besides adding additive noise to the final image, they can also introduce errors in quantitative parameter estimation in fields such as biological tissue characterization by shadowing or enhancing existing biological structures. The problem of reverberations in acoustics has been known from back in the 1940s, in the area of sea bottom mapping, and a lot of work has been done on the subject. Despite the number of papers on the reverberation problem, not much seems to have been done in the biomedical field for its identification and removal [27]. A method that is able to reduce or remove these reflections could improve the quality of ultrasound images, as well as the precision and accuracy in quantitative results such as the estimation of tissue elasticity. Although tissue harmonic imaging has proved to be very effective in reducing reverberations when the first scattering takes place within the near field [10, 11], the method has the disadvantage of having a lower amplitude than than the fundamental beam. This makes the SNR lower and may limit the benefits of the modality, e.g. because of penetration depth decrease.

1.3 Purpose of this study

As difference in elasticity of tissue give rise to different tissue displacements, and hence different time shifts in the recorded radio frequency (RF) signals, these time shifts can be estimated and hence produce an ultrasound image of tissue with different elastic properties, also known as an elastogram. When estimating the tissue displacement, a window around the sample in range is used to improve the estimate. Most methods assume a constant displacement over this window while in fact the degree of local stretching and compression can be substantial and can degrade the estimates. An estimator for estimating locally variable delays has been developed which is a

phase based approach and makes no assumption on the local delay variation [28]. The method uses the phase difference and an estimate of the instantaneous frequency of the IQ demodulated signal, and has then the advantage of being able to locally represent delays in terms of phase difference. Any parametric model may be used to model the local delay variations, and for this thesis the first step has been in adapting the time-delay algorithm for elastography purposes, and examine the effects different parametric models have on the final image quality.

Secondly, multiple reflections, also known as reverberations, greatly impair the contrast resolution of the final image, as they appear as additive noise at deeper depths than their true originals are located. Also the estimation of time delays, which is critical for elastography, may be greatly reduced by these reverberations. The SURF Imaging method may be used to suppress these strong reflections [4]. For this thesis it has been the main goal of using the phase-based time-delay algorithm, combined with SURF imaging with reverberation suppression, and prove the quality this approach has in reducing the effects of reverberations on the recorded RF signal, and then increase the quality of elastography recordings compared to other methods available at the time. This purpose then give the name of the paper as

Improving Elastography using SURF Imaging for Suppression of Reverberations

1.4 Structure of this paper

Chapter 2 gives a mathematical description of the time delay algorithm developed at the department, including an iterative scheme to update the estimates of the instantaneous frequency and the estimated time delays. Also this iterative scheme is characterized analytically. Chapter 3 gives an introduction to the principles of estimating tissue displacement and tissue elasticity. Chapter 4 displays the impact choosing different models for the estimation of the local delay has on the final image quality. Chapter 5 explains the concept of nonlinear propagation, its applications to the SURF imaging method, and the generation of time delays in the RF signal as a consequence of nonlinear wave propagation. Chapter 6 gives a theory on multiple scattering, and describes attempts of mimicking a multiple layered tissue in order to create reverberations and how this can be performed. Chapter 7 gives a mathematical, and theoretical description of the reverberation suppression capabilities of the SURF imaging method. Chapter 8 displays the effect both reverberations and the SURF reverberation suppression technique have on the quality of estimated elastography images. Process and results are discussed in Chapter 9, and some general conclusions are given in Chapter 10.

Chapter 2

Estimation and tracking of locally variable delays

Time delay estimation (TDE) has plenty of applications as diverse as radar, sonar, seismology, ultrasonics and communications. When the delay is varying with time it is also often known as delay tracking [29]. In medical imaging it is important for several ultrasound imaging methods, such as doppler, elastography and SURF imaging. In this paper it is the problem of estimating the range varying delays between two signals sent in the same direction which is of interest, and a phase based approach for estimating this delay is presented.

2.1 Phase-based time-delay estimation

The method to be presented is originally developed by Øyvind Standal [28] at the Department of Circulation and Medical Imaging (ISB) at NTNU. In the method a phase based approach which makes no assumption on the local delay variation is used, and the relationship between the instantaneous frequency of two signals and their phase difference is used to determine the delay. The method assumes a complex analytic signal, which can be computed by passing the real signal through the Hilbert transform.

2.1.1 Signal model

A complex band-limited 1D signal with real positive amplitude, a, centre frequency, ω_c, and modulating phase, φ, may be described as

$$s(t) = a(t) \exp\{i[\varphi(t) + \omega_c t]\} \tag{2.1}$$

The instantaneous frequency $\theta(t)$ of the signal $s(t)$ is defined as the time derivative of the argument, i.e. $\theta(t) = \frac{d}{dt} \arg\{s(t)\}$. Then considering the definition of our signal from Eq. (2.1), we may state the instantaneous frequency as

$$\theta(t) = \frac{\mathrm{d}}{\mathrm{d}t} \{\varphi(t) + \omega_c t\} = \varphi'(t) + \omega_c \tag{2.2}$$

where $\varphi'(t)$ is the derivate of the modulating phase. Now, defining a time varying subsample delay, $\tau(t)$, without loss of generality we assume symmetric delay and discretely sampled signals as

$$x(k) = s(k + \frac{1}{2}\tau(k)) = a(k + \frac{1}{2}\tau(k)) \exp\left\{ i \left[\varphi(k + \frac{1}{2}\tau(k)) + \omega_c k + \frac{1}{2}\omega_c \tau(k) \right] \right\} \tag{2.3}$$

$$y(k) = s(k - \frac{1}{2}\tau(k)) = a(k - \frac{1}{2}\tau(k)) \exp\left\{ i \left[\varphi(k - \frac{1}{2}\tau(k)) + \omega_c k - \frac{1}{2}\omega_c \tau(k) \right] \right\} \tag{2.4}$$

That is $x(k)$ has a positive delay of half a sample, and $y(k)$ has a negative delay of half a sample in respect to the original non-delayed signal $s(k)$.

2.1.2 Estimation of the phase difference ψ

Calculating the cross multiplication of $x(k)$ and $y(k)$ we get

$$x(k)y^*(k) = a(k + \frac{1}{2}\tau)a(k - \frac{1}{2}\tau) \exp\left\{ i \left[\varphi(k + \frac{1}{2}\tau) + \omega_c k + \frac{1}{2}\omega_c \tau \right] - i \left[\varphi(k - \frac{1}{2}\tau) + \omega_c k - \frac{1}{2}\omega_c \tau \right] \right\} \tag{2.5}$$

$$= a(k + \frac{1}{2}\tau)a(k - \frac{1}{2}\tau) \exp\left\{ i \left[\varphi(k + \frac{1}{2}\tau) - \varphi(k - \frac{1}{2}\tau) + \omega_c \tau \right] \right\} \tag{2.6}$$

where y^* denotes the complex conjugate of y and the dependence on k for $\tau(k)$ is dropped for notational convenience. The phase difference between the two signals can then be estimated as the argument of the cross multiplication as

$$\psi(k) = \arg\{x(k)y^*(k)\} = \varphi(k + \frac{1}{2}\tau(k)) - \varphi(k - \frac{1}{2}\tau(k)) + \omega_c \tau(k) \tag{2.7}$$

For narrowband signals φ is usually much smaller than ω_c, and an estimate of τ could be found by dividing Eq. (2.7) by ω_c. But in ultrasound a bandwidth of 50%-100% is common, so this narrowband approximation is seldom good enough [30]. Now, remembering the definition for derivation as

$$f'(x) = \lim_{\Delta x \to 0} \frac{f(x + \frac{1}{2}\Delta x) - f(x - \frac{1}{2}\Delta x)}{\Delta x} \tag{2.8}$$

we can approximate the first two parts in the last expression of Eq. (2.7) in the same manner, such that they can be stated as $\tau(k)\varphi'(k)$, and use the approximation that phase difference and delay is linearly related through the instantaneous frequency $\theta(k)$ as

$$\psi(k) \approx \tau(k)\varphi'(k) + \omega_c \tau(k) = [\varphi'(k) + \omega_c]\tau(k) = \theta(k)\tau(k) \tag{2.9}$$

The value of ω_c is relatively known, but we can't really say much of the phase φ. Instead we can try to estimate the instantaneous frequency, stated in Eq. (2.2), and for discretely sampled signals given as $\theta(k) = \varphi'(k) + \omega_c$, and we need an approximation for this expression as well.

2.1.3 Estimation of the instantaneous frequency θ

First calculating the phase of $x(k)$ we get

$$\begin{aligned}&\arg\{x(k+1)x^*(k-1)\}\\&= \varphi\left(k+1+\frac{1}{2}\tau(k+1)\right) - \varphi\left(k-1+\frac{1}{2}\tau(k-1)\right) + 2\omega_c + \frac{1}{2}\omega_c\tau(k+1) - \frac{1}{2}\omega_c\tau(k-1)\end{aligned} \tag{2.10}$$

This result may be simplified by using the same derivation approximation as in Eq. (2.9) such that the first two parts of Eq. (2.10) may be stated as $2\varphi'(k)$, and the phase of $x(k)$ is

$$\arg\{x(k+1)x^*(k-1)\} \approx 2\varphi'(k) + 2\omega_c + \frac{1}{2}\omega_c\tau(k+1) - \frac{1}{2}\omega_c\tau(k-1) \tag{2.11}$$

Likewise the expression for the phase of $y(k)$ may be derived in the same way yielding the result

$$\arg\{y(k+1)y^*(k-1)\} \approx 2\varphi'(k) + 2\omega_c - \frac{1}{2}\omega_c\tau(k+1) + \frac{1}{2}\omega_c\tau(k-1) \tag{2.12}$$

Then we can finally estimate the instantaneous frequency as

$$\theta(k) = \frac{1}{4}\left[\arg\{x(k+1)x^*(k-1)\} + \arg\{y(k+1)y^*(k-1)\}\right] \tag{2.13}$$

$$\approx \frac{1}{4}\left[2\varphi'(k) + 2\omega_c + \frac{1}{2}\omega_c\tau(k+1) - \frac{1}{2}\omega_c\tau(k-1) + 2\varphi'(k) + 2\omega_c - \frac{1}{2}\omega_c\tau(k+1) + \frac{1}{2}\omega_c\tau(k-1)\right] \tag{2.14}$$

$$= \frac{1}{4}\left[2\varphi'(k) + 2\omega_c + 2\varphi'(k) + 2\omega_c\right] \tag{2.15}$$

$$= \varphi'(k) + \omega_c \tag{2.16}$$

which is the discretely sampled equivalent of Eq. (2.2).

2.1.4 Modeling and finding the delay τ

We can estimate the phase difference $\psi(k)$ and the instantaneous frequency $\theta(k)$ through the equations

$$\psi(k) = \arg\{x(k)y^*(k)\} \approx [\varphi'(k) + \omega_c]\tau(k) \tag{2.17}$$

$$\theta(k) = \frac{1}{4}\left[\arg\{x(k+1)x^*(k-1)\} + \arg\{y(k+1)y^*(k-1)\}\right] \approx \varphi'(k) + \omega_c \tag{2.18}$$

and we have the relationship that phase difference and delay is linearly related through the instantaneous frequency as $\psi(k) \approx \theta(k)\tau(k)$. Thus an intuitive approach would be to divide the

phase difference by the instantaneous frequency to find the delay, but since both θ and τ are corrupted by noise, and θ has zero crossings, this would lead to inaccurate estimates as shown in Figure 2.1.

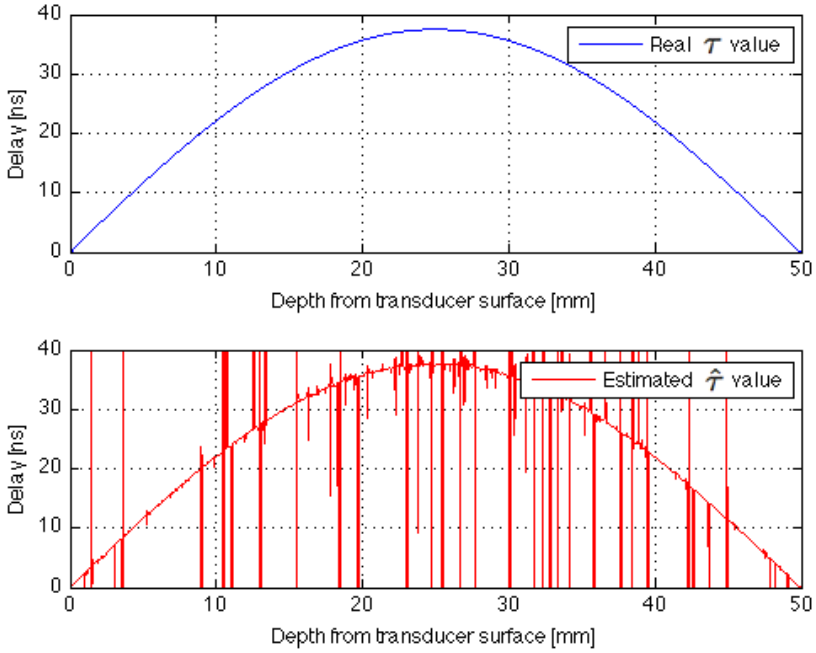

Figure 2.1: Inaccurate estimate of the time delay τ found by dividing the phase difference ψ by the instantaneous frequency θ

The challenge will be to find an adaption of $\theta(k)\tau(k)$ to $\psi(k)$ which is optimal in some sense. We choose a model for $\hat{\tau}(k)$ and try to minimize the difference between $\theta(k)\hat{\tau}(k)$ and $\psi(k)$ to find the optimal values of the model. That is we need to find the values that minimize

$$Q([\tau_k(n)] = \sum_n |\psi(n) - \theta(n)\tau_k(n))|^2 c(n)w(k) \tag{2.19}$$

where c is a weight function equal to the magnitude of the cross product of the two signals, w is a window function and k represents the depth of space. Finding the values that minimize Eq. (2.19) is a well known problem known as Weighted Least Squares (WLS).

2.2 Linear least squares

Least squares can be interpreted as a method of fitting data. The best fit, between modeled and observed data, in the least-squares sense is that instance of the model for which the sum of squared residuals has its least value. A residual being the difference between an observed value and the value given by the model.

2.2.1 The general case

A model $f(x_k, \beta)$ should be fitted through the given points $(x_1, y_1), ..., (x_n, y_n)$ so that the sum of the squares of the distances of those points from the line of the model is minimum, where the distance is measured in the vertical direction (the y-direction), and β are the parameters of the model. The sum of squares is expressed as

$$Q = \sum_{k=1}^{n} (y_k - f(x_k, \beta))^2 \tag{2.20}$$

The least squares method defines best as when the sum, Q, of squared residuals is a minimum. This is obtained by setting the partial derivates of Q with respect to the model parameters β equal zero.

$$\min Q = \frac{\partial Q}{\partial \beta} = -2 \sum_{k=1}^{n} (y_k - f(x_k, \beta)) \frac{\partial f(x_k, \beta)}{\partial \beta} = 0 \tag{2.21}$$

Writing in vector notation the above expression for the sum of squares as stated in Eq. (2.20) may be expressed as

$$Q = (Y - X\beta)^2 = (Y - X\beta)(Y - X\beta)^T \tag{2.22}$$

and we may find the minimum values by setting the partial derivates of Q equal to zero

$$\frac{\partial Q}{\partial \beta} = -2(Y - X\beta)X^T = 0 \tag{2.23}$$

$$X^T Y - X^T X\beta = 0 \tag{2.24}$$

$$X^T X\beta = X^T Y \tag{2.25}$$

$$\hat{\beta} = (X^T X)^{-1} X^T Y \tag{2.26}$$

The caret above $\hat{\beta}$ is to denote that it is a least squares estimate of the parameters in β, rather than its true value.

2.2.2 Weighted least squares

The expressions given above are based on the implicit assumption that the errors are uncorrelated with each other and with the independent variables and have equal variance. If, however, the measurements are uncorrelated but have different uncertainties, a modified approach might be adopted. The observations may be weighted, if for example they are not equally reliable, to give us the weighted sum of squares as

$$Q = \sum_{k=1}^{n} w_k (y_k - f(x_k, \beta))^2 \tag{2.27}$$

where $w_k > 0$. The diagonal weight matrix is most common the inverse of the variance-covariance matrix, but can also have any values as seen fit for the problem at hand.

$$W = \begin{bmatrix} w_1 & 0 & \dots & 0 \\ 0 & w_2 & \dots & 0 \\ \vdots & \vdots & \ddots & \vdots \\ 0 & 0 & \dots & w_n \end{bmatrix} \tag{2.28}$$

The weighted sum of squares may then be stated in vector notation as

$$Q = W(Y - X\beta)^2 = W(Y - X\beta)(Y - X\beta)^T \tag{2.29}$$

and the minimum values can be found by setting the partial derivate equal to zero.

$$\frac{\partial Q}{\partial \beta} = -2W(Y - X\beta)X^T = 0 \tag{2.30}$$

$$X^T WY - X^T WX\beta = 0 \tag{2.31}$$

$$X^T WX\beta = X^T WY \tag{2.32}$$

$$\hat{\beta} = (X^T WX)^{-1} X^T WY \tag{2.33}$$

2.2.3 $f(x_k, \beta)$ as a linear model

Now choosing a model as a first order polynomial, ie. a straight line

$$f(x_k, \beta) = a + bx_k \tag{2.34}$$

the sum of squares can be expressed as

$$Q = \sum_{k=1}^{n} (y_k - (a + bx_k))^2 = \sum_{k=1}^{n} (y_k - a - bx_k)^2 \tag{2.35}$$

Finding the minimum values consists of first taking the partial derivates of Q with respect to a and b, and setting each partial derivative to zero, then solving the resulting system of two equations with two unknowns

$$\frac{\partial Q}{\partial a} = -2 \sum_{k=1}^{n} (y_k - a - bx_k) = 0 \tag{2.36}$$

$$\frac{\partial Q}{\partial b} = -2 \sum_{k=1}^{n} (y_k - a - bx_k)x_k = 0 \tag{2.37}$$

Writing each sum as three sums will lead to the normal equations of the problem as

$$an + b\sum_{k=1}^{n} x_k = \sum_{k=1}^{n} y_k \tag{2.38}$$

$$a\sum_{k=1}^{n} x_k + b\sum_{k=1}^{n} x_k^2 = \sum_{k=1}^{n} x_k y_k \tag{2.39}$$

or in vector notation as

$$\begin{pmatrix} n & \sum_{k=1}^{n} x_k \\ \sum_{k=1}^{n} x_k & \sum_{k=1}^{n} x_k^2 \end{pmatrix} \begin{pmatrix} a \\ b \end{pmatrix} = \begin{pmatrix} \sum_{k=1}^{n} y_k \\ \sum_{k=1}^{n} x_k y_k \end{pmatrix} \tag{2.40}$$

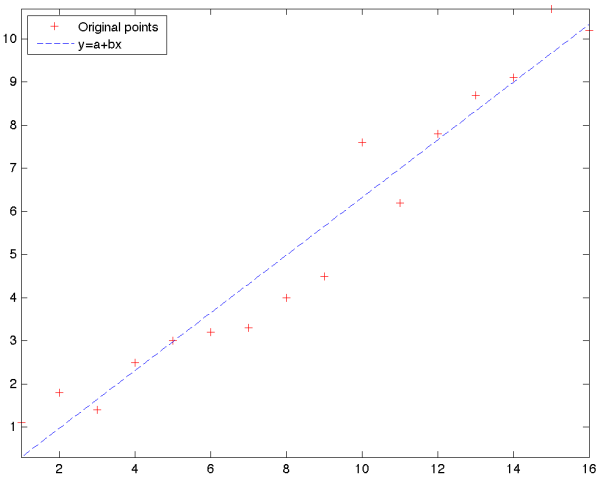

Figure 2.2: Fitting data points by the linear least squares method with a linear model

This result can also be expressed by defining the different matrices

$$X = \begin{bmatrix} 1 & x_1 \\ 1 & x_2 \\ \vdots & \vdots \\ 1 & x_n \end{bmatrix}, Y = \begin{bmatrix} y_1 \\ y_2 \\ \vdots \\ y_n \end{bmatrix}, \beta = \begin{bmatrix} a \\ b \end{bmatrix} \tag{2.41}$$

Comparing with Eq. (2.20), the sum of squares may be expressed in vector notation as in Eq. (2.22). Setting the partial derivate of Q to zero will yield the minimum values as in Eq. (2.26). Comparing Eq. (2.40) and Eq. (2.25) we see that the first matrix on the left hand side of Eq. (2.40) equals the matrix $X^T X$.

2.2.4 $f(x_k, \beta)$ as a polynomial of second order

Now trying to fit the data points with a second order polynomial as

$$f(x_k, \beta) = a + bx_k + cx_k^2 \tag{2.42}$$

yields the following expression for the sum of squares.

$$Q = \sum_{k=1}^{n} \left(y_k - (a + bx_k + cx_k^2)\right)^2 = \sum_{k=1}^{n} (y_k - a - bx_k - cx_k^2)^2 \tag{2.43}$$

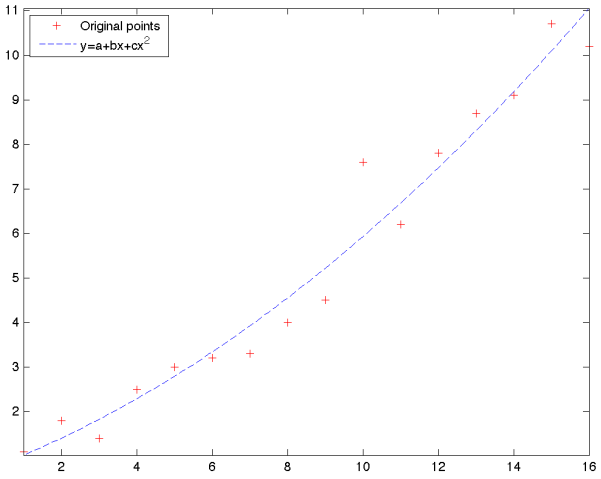

Figure 2.3: Fitting data points by the linear least squares method with a non-linear model

Writing in vector notation we have the following matrices for the computations

$$A = \begin{bmatrix} 1 & x_1 & x_1^2 \\ 1 & x_2 & x_2^2 \\ \vdots & \vdots & \vdots \\ 1 & x_n & x_n^2 \end{bmatrix}, Y = \begin{bmatrix} y_1 \\ y_2 \\ \vdots \\ y_n \end{bmatrix}, \beta = \begin{bmatrix} a \\ b \\ c \end{bmatrix} \tag{2.44}$$

which has the same solution as Eq. (2.26).

2.3 Linear least squares for phase-based time-delay estimator

2.3.1 The general case

When estimating time delays, a window around the sample in range is used to improve the estimates. Most methods assume a constant displacement over this window, while in fact the degree of local stretching and compression can be substantial and can degrade the estimates. For the phase based approach any model of the delay $\hat{\tau}_{k,n}$ can be chosen, where k marks the depth in space of the signal, and n marks a sample within the sample window.

For the phase-based time-delay estimator two complex analytical signals are said to have a phase difference, ψ, and varying subsample delay, τ, that is linearly related through the instantaneous frequency θ. The phase difference can hence be stated as $\psi \approx \theta\tau$, and the challenge is to find an adaption of $\theta\tau$ to ψ which is optimal in some sense. This can also be seen on as a least squares problem where the sum of squares is expressed as

$$Q = \sum_{n=k-\frac{N}{2}}^{k+\frac{N}{2}} (\psi_n - \theta_n \hat{\tau}_{k,n})^2 \tag{2.45}$$

A window of N number of samples is used, and k marks the depth of the window where the delay is to be computed. Writing in vector notation the above expression may be stated as

$$Q = (\Psi - \Theta\beta)^2 = (\Psi - \Theta\beta)(\Psi - \Theta\beta)^T \tag{2.46}$$

which will give the optimum parameter values $\hat{\beta}$ in the least squares sense of the model $\hat{\tau}_{k,n}$ as

$$\hat{\beta} = (\Theta^T\Theta)^{-1}\Theta^T\Psi \tag{2.47}$$

2.3.2 Weighted least squares

Now adding a certain weight to each observation the sum of squares can be expanded to the weighted least squares case as

$$Q = \sum_{n=k-\frac{N}{2}}^{k+\frac{N}{2}} w_n(\psi_n - \theta_n \hat{\tau}_{k,n})^2 \tag{2.48}$$

The weight matrix in the phase based time delay estimation case is equal to the magnitude of the cross product of the two signals to be compared, i.e.

$$w = |x(k)y^*(k)| \tag{2.49}$$

Writing in vector notation the weight matrix is expressed as

$$W = \begin{bmatrix} w_{k-\frac{N}{2}} & 0 & \dots & 0 \\ 0 & w_{k-\frac{N}{2}+1} & \dots & 0 \\ \vdots & \vdots & \ddots & \vdots \\ 0 & 0 & \dots & w_{k+\frac{N}{2}} \end{bmatrix} \tag{2.50}$$

and the weighted sum of squares may be stated as

$$Q = W(\Psi - \Theta\beta)^2 = W(\Psi - \Theta\beta)(\Psi - \Theta\beta)^T \tag{2.51}$$

which has its minimum solution as

$$\hat{\beta} = (\Theta^T W\Theta)^{-1}\Theta^T W\Psi \tag{2.52}$$

where W is a weight matrix, Θ is the instantaneous frequency matrix, and Ψ is the phase difference matrix.

2.3.3 $\hat{\tau}$ as a linear model

First we may choose a locally linear model of the delay as $\hat{\tau}_{k,n} = a_k + b_k n$, where k marks the depth in space of the signal, and n a sample within the sample window. The goal is hence to model the delay τ not as constant within the sample window, but rather as a straight line $\hat{\tau}$, determined by the values of a_k and b_k which for the linear model will be constant within the sample range at depth k.

Although we are using N samples centered around the point at depth k to compute the values of a_k and b_k, i.e. N is the number of samples in the sample window, we are only interested in the value at the specific point k. Choosing to multiply b_k with $(n-k)$, rather than n, in the expression for $\hat{\tau}_{k,n}$, and making sure the of number of samples N used in the sample window is odd numbered, ensures that our running variable $(n-k)$ goes from $-\frac{N}{2}$ to $\frac{N}{2}$ to cover the entire window length, and at the same time have a center point of k. The sum of squares for the phase-based time-delay estimator with the linear model can then be stated as

$$\hat{\tau}_{k,n} = a_k + b_k(n-k) \tag{2.53}$$

$$Q = \sum_{n=k-\frac{N}{2}}^{k+\frac{N}{2}} w_n(\psi_n - \theta_n \hat{\tau}_{k,n})^2 \tag{2.54}$$

$$= \sum_{n=k-\frac{N}{2}}^{k+\frac{N}{2}} w_n(\psi_n - \theta_n(a_k + b_k(n-k)))^2 \tag{2.55}$$

$$= \sum_{n=k-\frac{N}{2}}^{k+\frac{N}{2}} w_n(\psi_n - \theta_n a_k - \theta_n b_k(n-k))^2 \tag{2.56}$$

where N marks the total number of samples in the sample window, and k the depth of space where the delay is to be computed.

The different matrices used in the computations are expressed as

$$\Theta = \begin{bmatrix} \theta_{k-\frac{N}{2}} & (-\frac{N}{2})\theta_{k-\frac{N}{2}} \\ \theta_{k-\frac{N}{2}+1} & (-\frac{N}{2}+1)\theta_{k-\frac{N}{2}+1} \\ \theta_{k-\frac{N}{2}+2} & (-\frac{N}{2}+2)\theta_{k-\frac{N}{2}+2} \\ \vdots & \vdots \\ \theta_{k+\frac{N}{2}-1} & (\frac{N}{2}-1)\theta_{k+\frac{N}{2}-1} \\ \theta_{k+\frac{N}{2}} & (\frac{N}{2})\theta_{k+\frac{N}{2}} \end{bmatrix}, \beta = \begin{bmatrix} a_k \\ b_k \end{bmatrix}, \Psi = \begin{bmatrix} \psi_{k-\frac{N}{2}} \\ \psi_{k-\frac{N}{2}+1} \\ \psi_{k-\frac{N}{2}+2} \\ \vdots \\ \psi_{k+\frac{N}{2}-1} \\ \psi_{k+\frac{N}{2}} \end{bmatrix} \tag{2.57}$$

and W is the same as in Eq. (2.50). The sum of squares may then be noted in vector notation as in Eq. (2.51) with the solution for the minimum values as in Eq. (2.52). As β equals the solution matrix, the solution for the time delays may be stated as

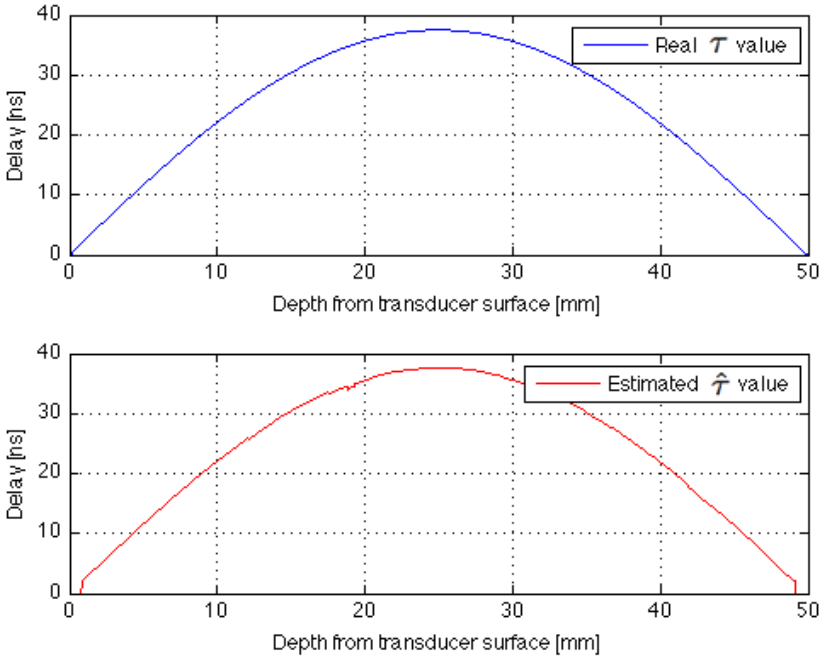

Figure 2.4: Correct estimate of the time delay τ found from the phase based approach choosing a linear model of $\hat{\tau}$ within a window of length 3.4 mm

$$\hat{\tau}(k) = a_k \tag{2.58}$$

$$\frac{\partial \hat{\tau}}{\partial k}(k) = b_k \tag{2.59}$$

That is a_k equals the smoothed estimate, and b_k equals the local rate of change of the model.

2.3.4 $\hat{\tau}$ as a polynomial of second order

Now, choosing to model the delay as a non-linear function, $\hat{\tau}_{k,n} = a_k + b_k n + c_k n^2$, we get the following weighted least squares expression for the phase-based time-delay estimation algorithm

$$\hat{\tau}_{k,n} = a_k + b_k(n-k) + c_k(n-k)^2 \tag{2.60}$$

$$Q = \sum_{n=k-\frac{N}{2}}^{k+\frac{N}{2}} w_k(\psi_n - \theta_n \hat{\tau}_{k,n})^2 \tag{2.61}$$

$$= \sum_{n=k-\frac{N}{2}}^{k+\frac{N}{2}} w_k(\psi_n - \theta_n(a_k + b_k(n-k) + c_k(n-k)^2))^2 \tag{2.62}$$

$$= \sum_{n=k-\frac{N}{2}}^{k+\frac{N}{2}} w_k(\psi_n - \theta_n a_k - \theta_n b_k(n-k) - \theta_n c_k(n-k)^2)^2 \tag{2.63}$$

The implication this alteration from a linear to a non-linear model of $\hat{\tau}$ has, is the shape of the instantaneous frequency matrix Θ, and the parameter matrix β now defined as

$$\Theta = \begin{bmatrix} \theta_{k-\frac{N}{2}} & (-\frac{N}{2})\theta_{k-\frac{N}{2}} & (-\frac{N}{2})^2\theta_{k-\frac{N}{2}} \\ \theta_{k-\frac{N}{2}+1} & (-\frac{N}{2}+1)\theta_{k-\frac{N}{2}+1} & (-\frac{N}{2}+1)^2\theta_{k-\frac{N}{2}+1} \\ \theta_{k-\frac{N}{2}+2} & (-\frac{N}{2}+2)\theta_{k-\frac{N}{2}+2} & (-\frac{N}{2}+2)^2\theta_{k-\frac{N}{2}+2} \\ \vdots & \vdots & \vdots \\ \theta_{k+\frac{N}{2}-1} & (\frac{N}{2}-1)\theta_{k+\frac{N}{2}-1} & (\frac{N}{2}-1)^2\theta_{k+\frac{N}{2}-1} \\ \theta_{k+\frac{N}{2}} & (\frac{N}{2})\theta_{k+\frac{N}{2}} & (\frac{N}{2})^2\theta_{k+\frac{N}{2}} \end{bmatrix}, \beta = \begin{bmatrix} a_k \\ b_k \\ c_k \end{bmatrix} \tag{2.64}$$

while the weight matrix W is the same as in Eq. (2.50), and the phase difference matrix Ψ is the same as Eq. (2.57). The solution for the parameters is expressed in Eq. (2.52).

2.4 Differences in modulating phase when estimating θ and ψ

When relating the phase difference $\psi(k)$ and the instantaneous frequency $\theta(k)$, we have used various approximations, especially regarding the modulating phase $\varphi(k)$ and the derivative of this $\varphi'(k)$. Throughout we are stating that $\varphi'(k)$ is equal both when estimating $\psi(k)$ and when estimating $\theta(k)$. The question remains however if this is a valid assumption. When estimating the phase difference we are using the approximation as stated in Section 2.1.2 for $\varphi'(k)$ as

$$\arg\{x(k)y^*(k)\} = \underbrace{\varphi(k+\frac{1}{2}\tau(k)) - \varphi(k-\frac{1}{2}\tau(k))}_{\tau(k)\varphi'(k)} + \omega_c\tau(k) \tag{2.65}$$

and when estimating the instantaneous frequency, the approximation as stated in Section 2.1.3 for $\varphi'(k)$ becomes

$$\arg\{x(k+1)x^*(k-1)\} = \underbrace{\varphi\left(k+1+\frac{1}{2}\tau(k+1)\right) - \varphi\left(k-1+\frac{1}{2}\tau(k-1)\right)}_{2\varphi'(k)} + \cdots \tag{2.66}$$

which in turn give us the relationships

$$\psi(k) = \arg\{x(k)y^*(k)\} \approx \varphi'(k)\tau(k) + \omega_c\tau(k) \tag{2.67}$$

$$\theta(k) = \frac{1}{4}\left[\arg\{x(k+1)x^*(k-1)\} + \arg\{y(k+1)y^*(k-1)\}\right] \approx \varphi'(k) + \omega_c \tag{2.68}$$

Now expressing the two different derivates of $\varphi(k)$ as $\varphi_1'(k)$ and $\varphi_2'(k)$ respectively, we have the following relationships

$$\psi(k) = \varphi_1'(k)\tau(k) + \omega_c\tau(k) \Rightarrow \varphi_1'(k) = \frac{\psi(k)}{\tau(k)} - \omega_c \tag{2.69}$$

$$\theta(k) = \varphi_2'(k) + \omega_c \Rightarrow \varphi_2'(k) = \theta(k) - \omega_c \tag{2.70}$$

Now calculating the values of $\varphi_1'(k)$ and $\varphi_2'(k)$ for a given signal, the two derivatives of the modulating phase can be plotted as seen on the top row of Figure 2.5 within a certain signal segment. As seen from the figure the two plots do indeed vary on several occasions. This may indicate that the generalization of the parameter $\varphi'(k)$ is somewhat inaccurate.

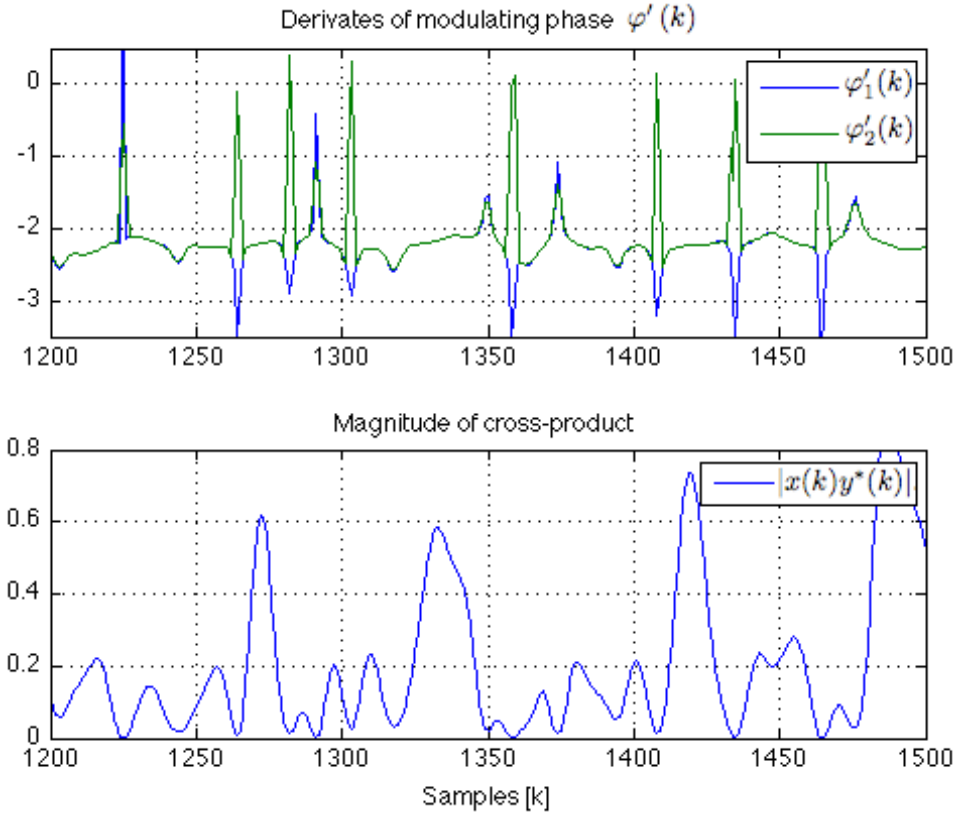

Figure 2.5: Difference of the derivate of the modulating phase $\varphi_1'(k)$ and $\varphi_2'(k)$ when estimating phase difference and the instantaneous frequency

Plotted on the bottom row of Figure 2.5 is the value of the weight matrix within the same signal segment. As stated in Section 2.3.2 the weight matrix is equal to the magnitude of the cross product of the two signals to be compared, i.e. $w = |x(k)y^*(k)|$. As seen from the figure there exists a strong correlation between the magnitude of the cross product and the similarity of the two modulating phase derivates $\varphi_1'(k)$ and $\varphi_2'(k)$. When the difference is large, the value of the weights are close or equal to zero, and when the signals are close to similar, the weights are large. This relationship is exploited in the weighted lest squares method by assigning a low weight to observations which are unreliable, as illustrated by Figure 2.5, thus minimizing the overall error.

2.5 Iterative scheme to find optimal values of the instantaneous frequency

Although the time delay is a part of the analytical model when estimating the instantaneous frequency as given in Eq. (2.10), it is omitted when approximating the derivate of the modulating phase as stated in Eq. (2.66). As discussed in Section 2.4 this introduces an error in the estimate. A different approach when estimating the instantaneous frequency would be in not spacing the two signals by one sample as $k+1$, but rather some other parameter to make the expression for the modulating phase as equal to that stated in Eq. (2.65). We begin by spacing the two delayed signals by two constants α_1 and α_2, and omit the dependence of k for τ for notational convenience

$$\hat{\theta}(k) = \arg\{x(k)x^*(k+\alpha_1)\} + \arg\{y(k+\alpha_2)y^*(k)\} \tag{2.71}$$

$$\begin{aligned} &= \varphi\left(k+\frac{\tau}{2}\right) + \omega_c\left[k+\frac{\tau}{2}\right] - \varphi\left(k+\frac{\tau}{2}+\alpha_1\right) - \omega_c\left[k+\frac{\tau}{2}+\alpha_1\right] \\ &+ \varphi\left(k-\frac{\tau}{2}+\alpha_2\right) + \omega_c\left[k-\frac{\tau}{2}+\alpha_2\right] - \varphi\left(k-\frac{\tau}{2}\right) - \omega_c\left[k-\frac{\tau}{2}\right] \end{aligned} \tag{2.72}$$

$$= \varphi\left(k+\frac{\tau}{2}\right) - \varphi\left(k+\frac{\tau}{2}+\alpha_1\right) - \omega_c\alpha_1 + \varphi\left(k-\frac{\tau}{2}+\alpha_2\right) - \varphi\left(k-\frac{\tau}{2}\right) + \omega_c\alpha_2 \tag{2.73}$$

Now by separating the phase of the signal that has a positive delay of half a sample and comparing with the expression for phase difference as given in Eq. (2.65), it is quite easy to deduce the value of the factor α_1

$$\arg\{x(k)x^*(k+\alpha_1)\} = \underbrace{\varphi\left(k+\frac{\tau}{2}\right) - \varphi\left(k+\frac{\tau}{2}+\alpha_1\right)}_{\alpha_1=-\tau} - \omega_c\alpha_1 \tag{2.74}$$

And likewise for the signal that has a negative delay of half a sample one can deduce the value of the factor α_2

$$\arg\{y(k+\alpha_2)y^*(k)\} = \underbrace{\varphi\left(k-\frac{\tau}{2}+\alpha_2\right) - \varphi\left(k-\frac{\tau}{2}\right)}_{\alpha_2=\tau} + \omega_c\alpha_2 \tag{2.75}$$

The result means that in order to minimize the difference of the modulating phase when calculating the phase difference and the instantaneous frequency, the correct approach when estimating the instantaneous frequency would be in not spacing the two signals by one sample as $k+1$, but rather by the delay itself. As the delay is unknown, an approach to this problem is to use the estimated delay $\hat{\tau}$, to space the signals by $k+\hat{\tau}$. The expression for the updated estimate of the instantaneous frequency then becomes

$$\hat{\theta}(k) = \arg\{x(k)x^*(k-\hat{\tau})\} + \arg\{y(k+\hat{\tau})y^*(k)\} \tag{2.76}$$

$$= \varphi\left(k+\frac{\tau}{2}\right) - \varphi\left(k+\frac{\tau}{2}-\hat{\tau}\right) + \varphi\left(k-\frac{\tau}{2}+\hat{\tau}\right) - \varphi\left(k-\frac{\tau}{2}\right) + 2\omega_c\hat{\tau} \tag{2.77}$$

Now if we assume the estimated delay $\hat{\tau}$ is equal to the original delay τ, the expression becomes

$$\hat{\theta}(k) = \underbrace{\varphi\left(k+\frac{\hat{\tau}}{2}\right) - \varphi\left(k-\frac{\hat{\tau}}{2}\right)}_{\hat{\tau}\varphi'(k)} + \underbrace{\varphi\left(k+\frac{\hat{\tau}}{2}\right) - \varphi\left(k-\frac{\hat{\tau}}{2}\right)}_{\hat{\tau}\varphi'(k)} + 2\omega_c\hat{\tau} \tag{2.78}$$

$$= 2\hat{\tau}\varphi'(k) + 2\omega_c\hat{\tau} \tag{2.79}$$

$$= 2\hat{\tau}[\varphi'(k) + \omega_c] = 2\hat{\tau}\theta(k) \Rightarrow \theta(k) = \frac{1}{2\hat{\tau}}\hat{\theta}(k) \tag{2.80}$$

This means that an optimal estimator for the instantaneous frequency can be expressed as

$$\hat{\theta}(k) = \frac{1}{2\hat{\tau}} \arg\{x(k)x^*(k-\hat{\tau})\} + \arg\{y(k+\hat{\tau})y^*(k)\} \tag{2.81}$$

or by again introducing the dependence of k for the delay, the estimator may be stated as

$$\hat{\theta}(k) = \frac{1}{2\hat{\tau}(k)} \arg\{x(k)x^*(k-\hat{\tau}(k))\} + \arg\{y(k+\hat{\tau}(k))y^*(k)\} \tag{2.82}$$

This can be implemented in an iterative scheme, which updates the values for the instantaneous frequency θ_{n+1} based on the estimated delays $\hat{\tau}_n$. First an initial estimate of the instantaneous frequency as described by Eq. (2.68) must be made, and the initial values for the estimated delay may be computed through Eq. (2.52). This initial estimate for the delay may again be used to calculate an updated estimate of the instantaneous frequency as given in Eq. (2.82), which again can be used to calculate a new updated estimate of the delay. The entire procedure may also be described in pseudocode as

$M \leftarrow$ number of iterations
$L \leftarrow$ number of samples
$\hat{\theta}_1 \leftarrow \frac{1}{4}\left[\arg\{x(k+1)x^*(k-1)\} + \arg\{y(k+1)y^*(k-1)\}\right]$
for $n = 1$ to M **do**
  for $k = 1$ to L **do**
    $\hat{\beta} \leftarrow (\hat{\Theta}_n^T W \hat{\Theta}_n)^{-1}\hat{\Theta}_n^T W \Psi$
    $\hat{\tau}_n(k) \leftarrow \hat{\beta}_1$
  end for
  $\hat{\theta}_{n+1} \leftarrow \frac{1}{2\hat{\tau}_n}\left[\arg\{x(k)x^*(k-\hat{\tau}_n)\} + \arg\{y(k+\hat{\tau}_n)y^*(k)\}\right]$
end for

As stated in Section 2.3.3 a window of N number of samples is used to improve the estimate, and the delay is calculated over this window. This introduces some problems however, as the estimated delay values will be set to zero over a range of $N/2$, or half the window length, at the start and the end of the estimated delay values. This again will introduce errors in the updated values for the instantaneous frequency using the iteration scheme. One solution to this problem is to assume zero delay at the start of the signal, and interpolate the values from this starting point up to the value of the first estimated delay $\hat{\tau}_s$, and assume the delay is linear over those samples as seen in Figure 2.6. The second assumption deals with the values at the end of the estimated delay signal, and these values are assumed to be constant equal to the value of the last estimated delay $\hat{\tau}_e$. A third problem arises if some of the estimated instantaneous frequency values after iteration are non-existent. Since these values are used to calculate the delay $\hat{\tau}_n$ a solution is to use existing calculated values.

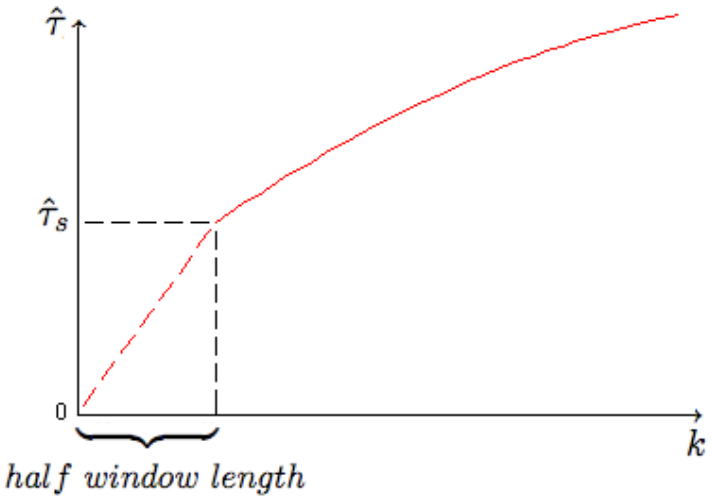

Figure 2.6: Interpolation scheme to determine non-existing values at the start of the estimated time delay

The entire procedure may again be described in pseudocode as

$M \leftarrow$ number of iterations
$L \leftarrow$ number of samples
$N \leftarrow$ window length
$\hat{\theta}_1 \leftarrow \frac{1}{4}\left[\arg\{x(k+1)x^*(k-1)\} + \arg\{y(k+1)y^*(k-1)\}\right]$
for $n = 1$ to M **do**
  for $k = N/2$ to $L - N/2$ **do**
    $\hat{\beta} \leftarrow (\hat{\Theta}_n^T W \hat{\Theta}_n)^{-1} \hat{\Theta}_n^T W \Psi$
    $\hat{\tau}_n(k) \leftarrow \hat{\beta}_1$
  end for
  for $k = 1$ to $N/2$ **do**
    $\hat{\tau}(k) \leftarrow 2\hat{\tau}_n(N/2)k/N$
  end for
  for $k = L - N/2$ to L **do**
    $\hat{\tau}(k) \leftarrow \hat{\tau}_n(L - N/2)$
  end for
  $\hat{\theta}_{n+1} \leftarrow \frac{1}{2\hat{\tau}_n}\left[\arg\{x(k)x^*(k-\hat{\tau}_n)\} + \arg\{y(k+\hat{\tau}_n)y^*(k)\}\right]$
  if $\hat{\theta}_{n+1}(k)$ is non-existent **then**
    $\hat{\theta}_{n+1}(k) \leftarrow \hat{\theta}_n(k)$
  end if
end for

2.6 Analytical characterization of instantaneous frequency iteration algorithm

Now using the same signal as in Section 2.4, again we can plot the two derivates of the modulating phase. As seen from Figure 2.7, the effect of using the estimated delay values $\hat{\tau}$ to estimate an updated value for the instantaneous frequency as described by Eq. (2.82) becomes quite clear.

The two derivates follow each other much more closely as opposed to the situation seen in Figure 2.5 when the method described by Eq. (2.68) to estimate the instantaneous frequency is utilized.

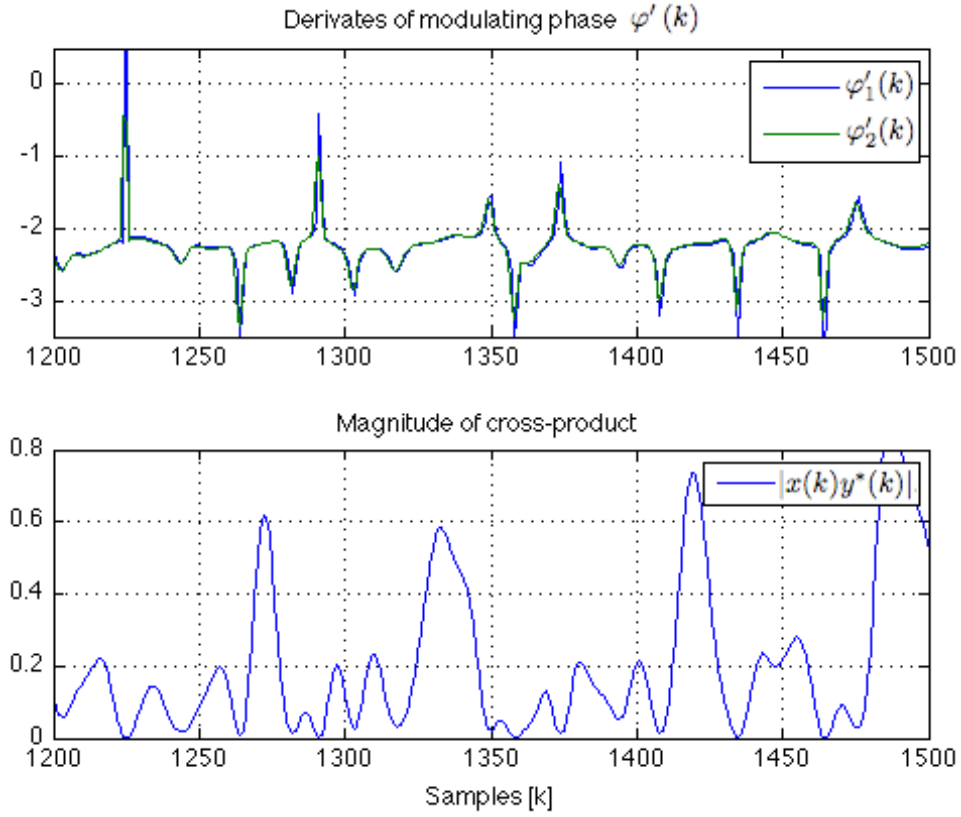

Figure 2.7: Difference of the derivate of the modulating phase $\varphi_1'(k)$ and $\varphi_2'(k)$ when estimating phase difference and the instantaneous frequency after one iteration of the minimum phase difference algorithm

As the time-delay estimator is a phase based estimator, this introduces some limitations on the maximum delay we are able to detect. As the phase by definition varies from minus π to π, i.e. $\angle = [-\pi, \pi]$, this means that the maximum phase difference between two signals equals π. This can again be related to the maximum time-delay we are able to detect as

$$\psi_{max} = \omega_c \tau_{max} = \pi \tag{2.83}$$

$$2\pi f_c \tau_{max} = \pi \tag{2.84}$$

$$\tau_{max} = \frac{1}{2f_c} \tag{2.85}$$

or in number of samples as

$$\tau_{max} = \frac{f_s}{2f_c} = \frac{1}{2f_c T_s} \tag{2.86}$$

where f_c equals the center frequency and T_s the sampling period. A larger center frequency will in turn lower the maximum detectable delay in seconds as seen in Figure 2.8.

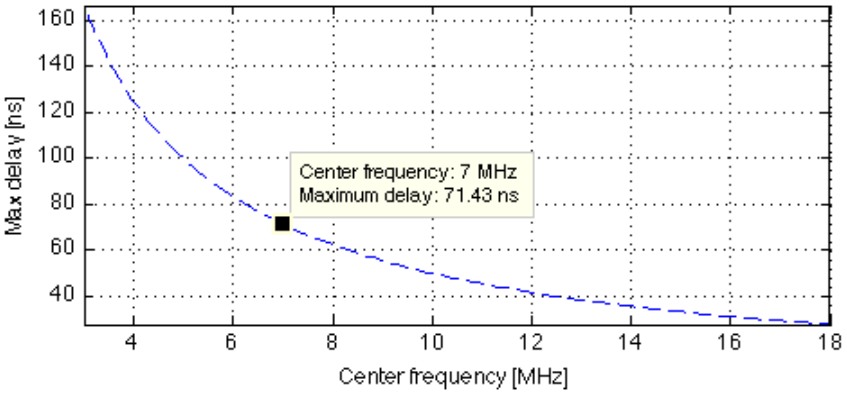

Figure 2.8: Maximum detectable delay in nanoseconds as a function of center frequency when estimating with the phase-based time-delay estimator

To characterize the impact of the instantaneous frequency iteration scheme we start by simulating a random signal $s(k)$ with center frequency $f_c = 7$ MHz, sampling frequency $f_s = 40$ MHz and a relative bandwidth of 50% of the center frequency, or a drop in intensity of 6 dB from its maximum value, i.e. $B_w = 3.5$ MHz. Now by defining two signals delayed in respect to $s(k)$ as $x(k)$ and $y(k)$, described in detail by Eq. (2.3) and Eq. (2.4), respectively, we get

$$x(k) = s(k + \frac{\tau(k)}{2}) \tag{2.87}$$

$$y(k) = s(k - \frac{\tau(k)}{2}) \tag{2.88}$$

The delay is assumed to be linear so it increases with depth up to a certain maximum value decided by Eq. (2.86), which for $f_c = 7$ MHz and $f_s = 40$ MHz equals 71 nanoseconds or 2.8 samples. The two delayed RF signals may for instance look something like displayed in Figure 2.9.

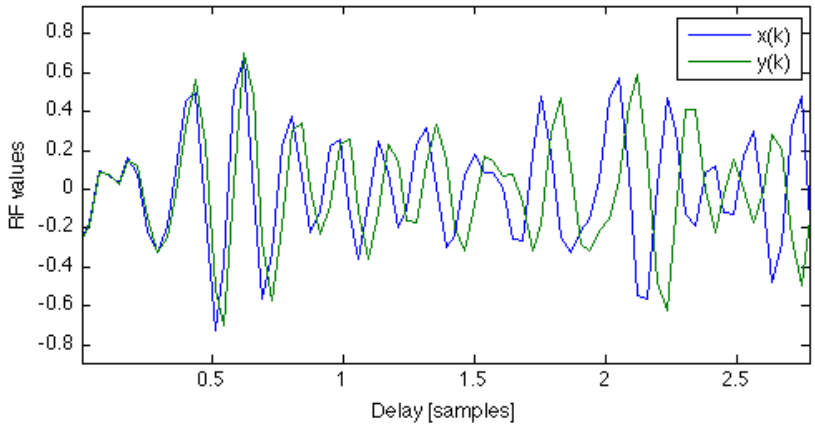

Figure 2.9: Two RF signals delayed in respect to each other with linearly increasing delay and center frequency $f_c = 7$ MHz, sampling frequency $f_s = 40$ MHz and 50% relative bandwidth

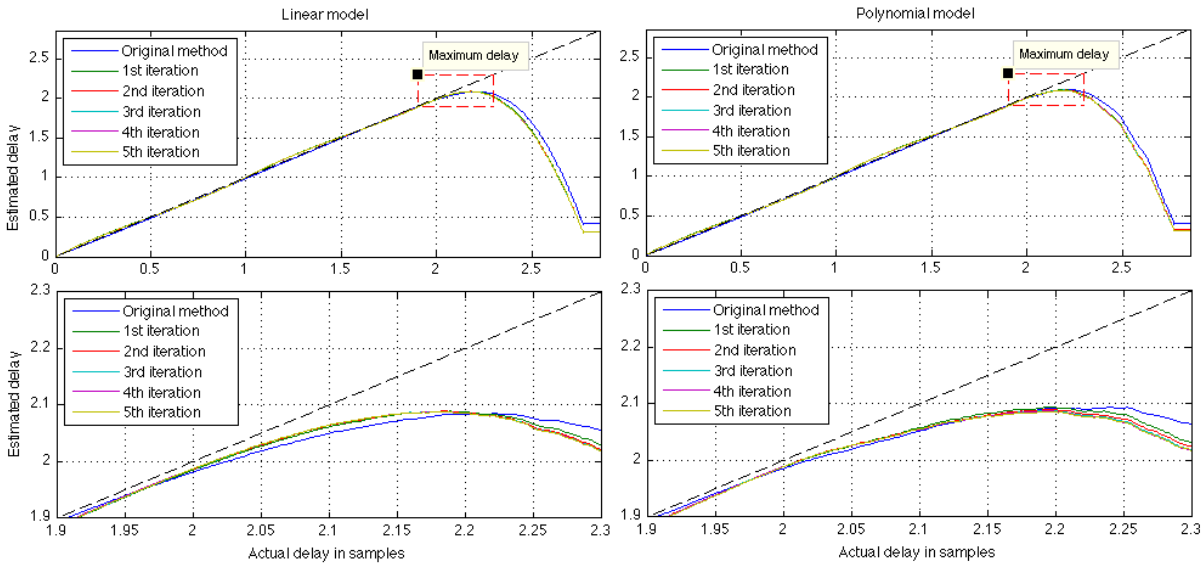

Figure 2.10: Maximum estimated delay by the phase-based time-delay estimator as a function of the actual delay for linear and polynomial model. Simulated with center frequency $f_c = 7$ MHz, sampling frequency $f_s = 40$ MHz, 50% relative bandwidth and $n = 1000$.

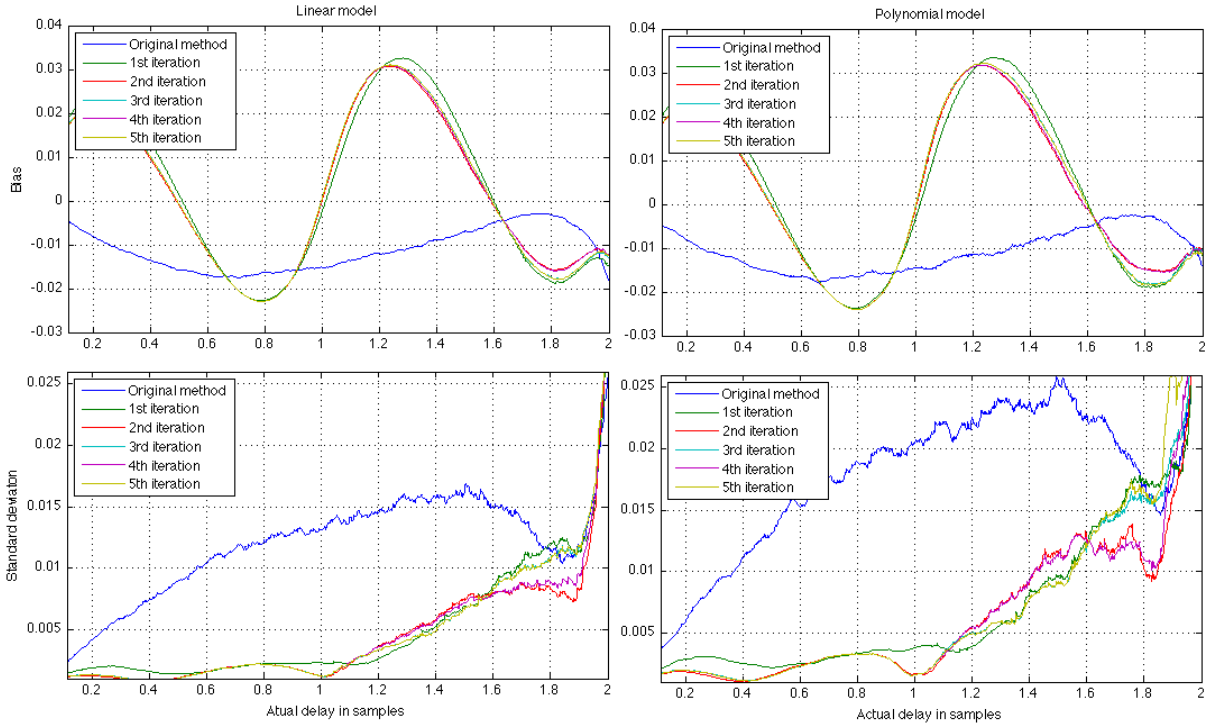

Figure 2.11: Bias and standard deviation for linear and polynomial model when estimated by the phase-based time-delay estimator as a function of the actual delay. Simulated with center frequency $f_c = 7$ MHz, sampling frequency $f_s = 40$ MHz, 50% relative bandwidth and $n = 1000$.

Seen in Figure 2.10 is the maximum delay which the phase-based algorithm is able to detect when simulating with a center frequency $f_c = 7$ MHz, sampling frequency $f_s = 40$ MHz, 50% relative bandwidth and number of simulations $n = 1000$. The actual delay between $x(k)$ and $y(k)$ is plotted in the dashed black line as seen on the top row of the figure, and is as already stated linearly increasing from zero to a maximum value as described by Eq. (2.86). The estimated values when using the linear model are plotted on the left hand side of the figure, while the estimated values when using the polynomial model of the second degree are plotted on the right hand side. Inspecting the estimated delay values as seen in Figure 2.10 it seems that both the linear and the polynomial model implemented using the iteration scheme described in Section 2.5 are able to detect a delay up until around two samples, or 50 nanoseconds using these parameters, before gradually deviating from the actual delay value. Although there exist slight differences between the estimated delay with and without the iteration scheme, using the parameters for f_s and f_c, they are almost negligible judging from the estimated delay alone.

To be able to see the impact the iteration scheme has on the estimated delay, the mean and standard deviation in number of samples are plotted for both models and all iterations as seen in Figure 2.11. The effect of using an iteration scheme for estimating the values of the instantaneous frequency is markedly clear. Although the iterations introduce a larger bias for the estimated delay values, it lowers the standard deviation significantly. As seen from the figure the iteration scheme works best for constant delays of around one sample, for which the bias is zero and the standard deviation is the lowest. Also interesting to notice is the increased magnitude of the standard deviation without iterations when comparing the linear and the polynomial model. This variation has all but been eliminated when using the iteration scheme as seen on the lower part of Figure 2.11.

For a sufficient sampling rate it seems that a single iteration of the instantaneous frequency iteration algorithm is adequate to lower the variance, but what is the impact if the sampling rate is lowered? The Nyquist rate is defined as the minimum sampling rate required to avoid aliasing, and for bandpass signals the Nyquist rate equals two times the highest frequency component of the signal, and an interesting observation occurs when sampling the signal below the Nyquist rate without filtering the signal with an anti-aliasing filter.

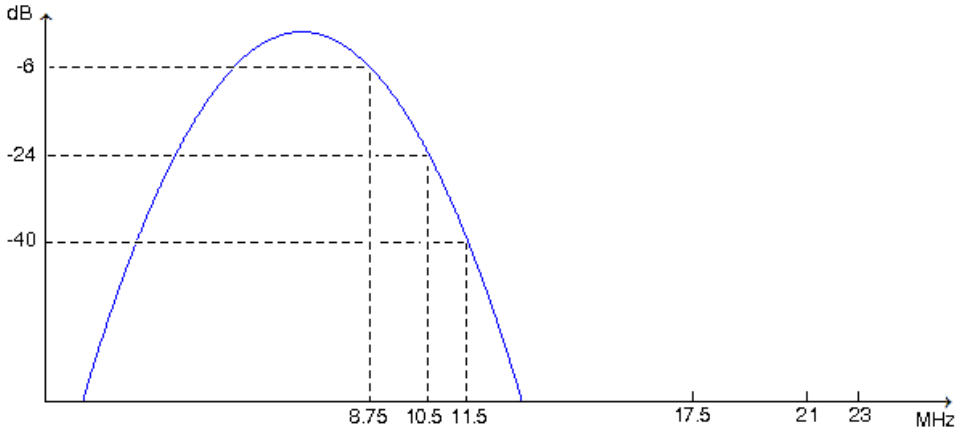

Figure 2.12: One sided normalized frequency spectrum of a band limited signal with Nyquist limits f_N and various minimum sampling frequencies $f_{s,min}$ for various bandwidths. Simulated with center frequency $f_c = 7$ MHz, sampling frequency $f_s = 40$ MHz, 50% relative bandwidth.

Seen in Figure 2.12 is the one sided frequency spectrum of the band limited signal having a

center frequency of 7 MHz. By sampling with a sampling frequency $f_s = 40$ MHz, we are clearly above this limit. Plotted in the figure are three different scenarios for Nyquist limit f_N and minimum sampling frequency $f_{s,min} = 2f_N$ which are described in detail in Table 2.1

Relative B_w	B_w	Drop in signal strength	f_N	$f_{s,min}$
50%	3.5 MHz	-6 dB	8.75 MHz	17.5 MHz
100%	7 MHz	-24 dB	10.5 MHz	21 MHz
130%	9 MHz	-40 dB	11.5 MHz	23 MHz

Table 2.1: Various bandwidth parameters when simulating with a center frequency $f_c = 7$ MHz

As given from the table, the bandwidth of the signal is related to the drop in signal strength of the one sided normalized frequency spectrum from its maximum value. A drop of 6 dB then corresponds to a relative bandwidth of 50%, or 3.5 MHz when simulating with a center frequency of 7 MHz. And a drop of of 24 dB and 40 dB corresponds to a relative bandwidth of 100% and 130%, or a bandwidth of 7 MHz and 9 MHz respectively. By sampling the signal with the lowest possible sampling frequencies $f_{s,min}$ as given in the fifth column of Table 2.1, we can plot the impact both the lowered sampling frequency and the iteration scheme has on the estimated delay values as plotted in Figure 2.13.

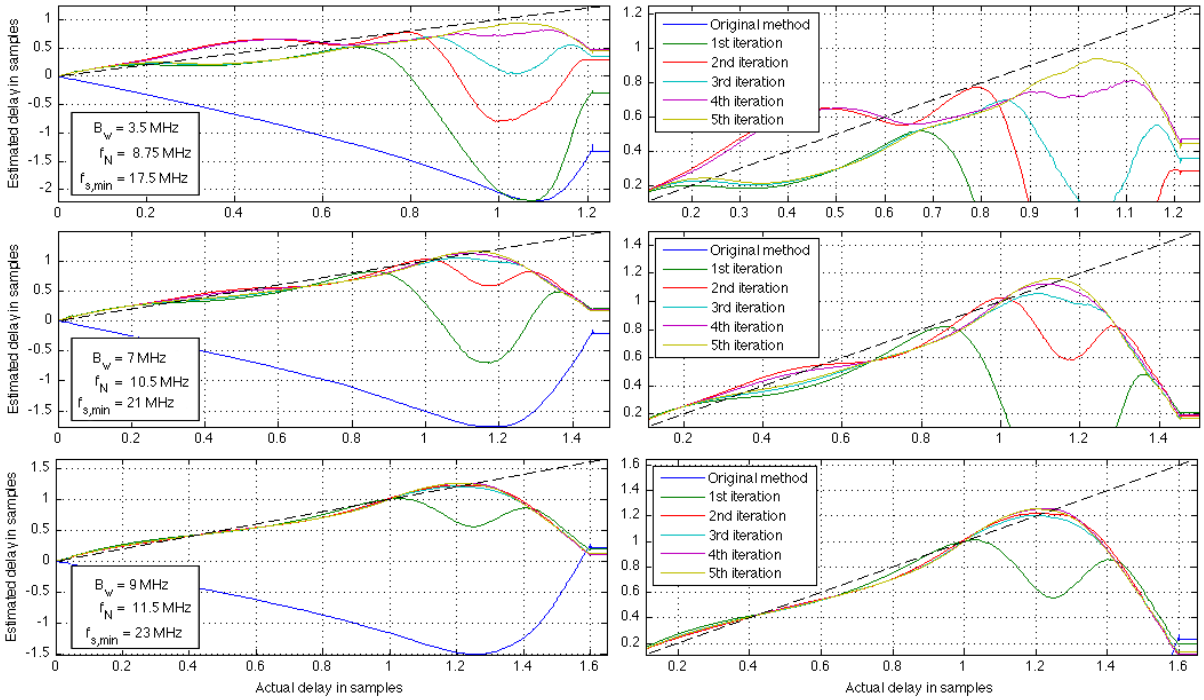

Figure 2.13: Maximum estimated delay by the phase-based time-delay estimator using a linear model as a function of the actual delay for different bandwidths and sampling frequencies. Simulated with center frequency $f_c = 7$ MHz and 50% relative bandwidth.

For the simulations a linear model was used as parametric model of the delay. The right hand side of the figure is a region of interest from the estimated delay values plotted on the left hand side. The first row displays the estimated values when using the parameters stated in the first row of Table 2.1, the second row displays the estimated values when using the parameters stated in the second row of Table 2.1, and the last row of the figure displays the estimated delay values

when using the parameters stated in the third row of Table 2.1.

As already stated the maximum delay possible to detect is a function of the sampling frequency as given by Eq. (2.86). This in turn means that the three different situations plotted on the three different rows of Figure 2.13 are scaled differently up to a maximum value. For the top row this corresponds to about 1.2 samples, for the second row 1.4 samples, and 1.6 samples for the third row. No anti-aliasing filter is used on the signal, and aliasing is bound to occur as the sampling rate is lowered. What is intuitively seen is that the estimated delay values when using the ordinary method for estimating the instantaneous frequency as stated in Eq. (2.68) and plotted in blue of Figure 2.13, completely fails to estimate the correct delay. This even goes for the highest sampling frequency as seen on the left hand side of the bottom row of the figure. Although the ordinary method is able to detect and estimate the correct delay when the sampling rate is sufficient as seen in Figure 2.10, it fails to do the corresponding correct delay estimation when sampling the signal at a much lower sampling rate. When using the iteration scheme on the other hand, the curve of estimated delay values follows the correct delay much more closely. When inspecting the top row of the figure it is clear that even at this low sampling rate the iteration algorithm manages to some degree to follow the correct delay curve, and as the iteration number increases, so increases the maximum detected delay. This might suggest the feasibility of the algorithm to iterate closer and closer to the correct value even when the sampling rate is low and beneath the Nyquist limit. To characterize the impact further, again it is possible to plot the bias and standard deviation given in samples for the three different situations as seen in Figure 2.14.

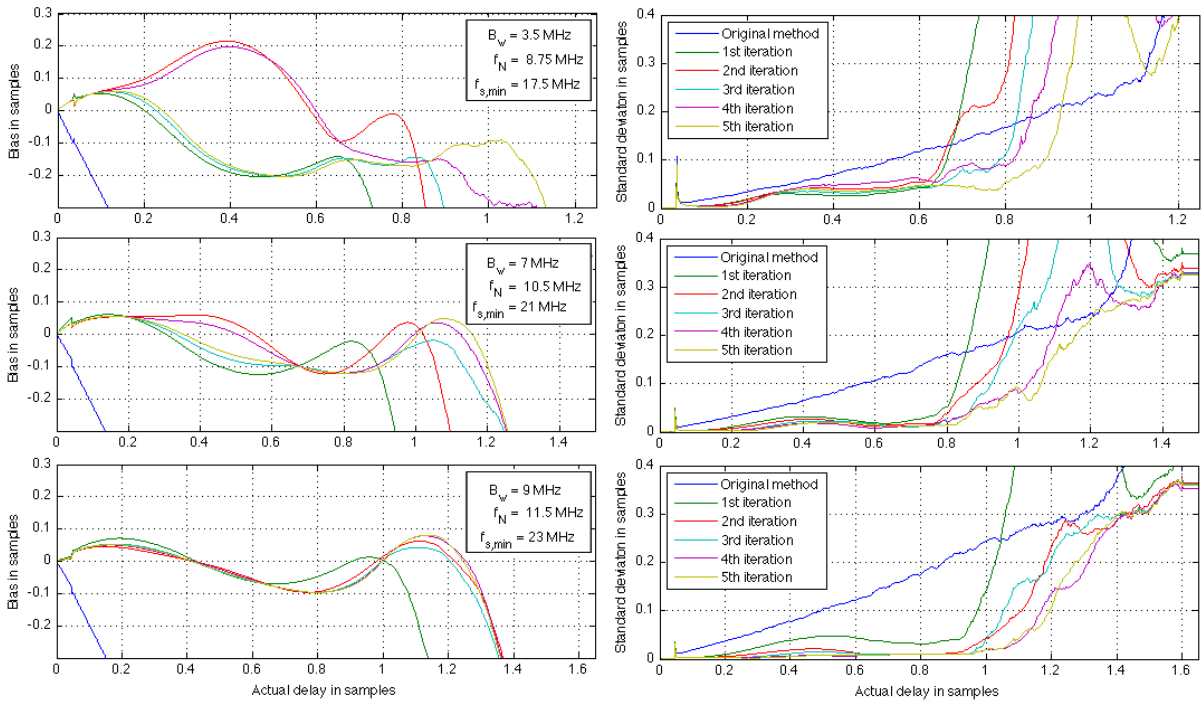

Figure 2.14: Bias and standard deviation in samples by the phase-based time-delay estimator using a linear model as a function of the actual delay for different bandwidths and sampling frequencies. Simulated with center frequency $f_c = 7$ MHz and 50% relative bandwidth.

Again the iteration scheme manages to lower the standard deviation, and an increased number of iterations will also lead to increased lowering of the standard deviation.

Chapter 3

Estimating tissue elasticity

Since the early beginnings of medical practice, the estimation of tissue hardness has been practiced through palpation, i.e. the act of feeling or pushing on various parts of a patient's body to determine medical conditions. Palpation has been an important tool to detect abnormalities in the body, mainly because the mechanical properties of diseased tissue are typically different than that of the healthy tissue surrounding it. A tumor or a suspicious cancerous growth is normally much stiffer than the background of normal soft tissue [12]. The basic relationship between tissue elasticity and hardness to palpability then follows the relationship that in order to be palpable, the object must be harder than the tissue surrounding it. However in many cases despite the differences in stiffness, the small size of a pathological lesion makes it harder to detect, and lesions located at deeper depths than the fingers are able to to sense preclude its detection and characterization. Palpation is then limited to the detection of abnormalities and tumors which are close to the skin. Ordinary ultrasound has the advantage of imaging deep inside the body, but is virtually unable to differ between tissue of various hardness and elasticity, and there has been a consistent interest in tissue hardness, motion and vibration over the years. Tissue elasticity is characterized by the amount of tissue displacement or distortion in response to the application of an external force. There are several ways of estimating tissue elasticity by ultrasound, but basically the various methods fall into three main categories.

3.1 Sonoelasticity imaging

Initial experiments in differentiating between normal soft tissues and hard lesions using ultrasound were conducted around 1986, but it was not until Lerner et. al. presented a method named "sonoelasticity imaging" in 1989 the concept had any practical implications [14, 15]. Sonoelasticity imaging, or sonoelastography, involves the application of a low-frequency vibrational energy to the tissue, and the simultaneous motion detection by Doppler technique to detect the ultrasonic waves that have been influenced by the vibrations. In sonoelasticity imaging the acoustic vibration is in the audible range (30-200Hz), and is transmitted in the tissue of interest. Color Doppler imaging is then used to detect the resulting tissue stiffness. Since the velocity of propagation is a function of the elastic properties of tissue, measurement of the velocity of a propagating mechanical vibration in tissue will yield the differences in elasticity. The concept is that stiff tissues will respond differently to an applied mechanical vibration than normal tissue. Areas, or tissue, of increased stiffness will experience less or decreased vibrations which can be seen as a "void" in the Doppler sonoelasticity image. The main advantage of this technique is

the ability to view the in-vivo results in real time, as the signal processing involved is basically equivalent to well established Doppler methods. [31, 32].

3.2 Transient elastography

A different approach called transient elastography was presented by Sandir et. al. in 1999 [20]. The method relies on the observation of the propagation of a pulsed shear wave, i.e. a wave where the oscillations occur perpendicular to the direction of energy transfer, to determine the elastic properties of tissue, also known as transient elastography. The shear wave propagating in the tissue has a very low-frequency ($\backsim$ 60 Hz), and the local velocity (typically from 1 to 10 m/s) of the wave is directly related to the Young's modulus, E. The Young's modulus is also known as the modulus of elasticity, and can be calculated by dividing the tensile stress by the tensile strain as given by Eq. (3.1)

$$E = \frac{\text{tensile stress}}{\text{tensile strain}} = \frac{\sigma}{\varepsilon} = \frac{F/A_0}{\Delta L/L_0} = \frac{FL_0}{A_0 \Delta L} \tag{3.1}$$

where E is the Young's modulus (modulus of elasticity), F is the force applied to the object, A_0 is the original cross-sectional area through which the force is applied, ΔL is the amount by which the length of the object changes, and L_0 is the original length of the object. A shear elasticity map of the medium may be computed using an inversion algorithm. Because the shear waves propagate through the medium in less than 0.1 s, the displacements induced by the shear wave are measured with an ultrasonic array connected to an ultrafast imaging system able to reach frame rates up to 6000 Hz. Transient elastography then has the advantages of being insensitive to patient motion and boundary condition artifacts because of its real-time capabilities with an acquisition time in less than 20 ms [21]. A different technique with close resemblance to transient elastography known as supersonic shear imaging (SSI) was presented by Bercoff et. al in 2004 [23]. In SSI the source radiates low-frequency shear waves inside the tissue, but makes the shear source move with supersonic speed to create quasiplane shear waves of stronger amplitude. Such a shear source which moves faster than the shear waves can be created by successively focusing the ultrasonic "pushing" beam at different depths. All resulting shear waves will interfere constructively along a Mach cone, creating two intense quasiplane shear waves propagating in opposite directions.

3.3 Elastography

The term "elastography" was coined by Ophir et. al. in 1991 as a quantitative method of imaging the elasticity of biological tissue by direct imaging of the strain and the Young's modulus of tissue [16]. Elastography involves quasi-static compression of tissue and the analysis of the echoes returned to the transducer before they are converted into B-mode images. The elastography method is based on external tissue compression, with subsequent computation of the strain profile along the transducer axis, and differs in other methods in several important aspects. The force applied to the tissue is not vibratory, but rather considered quasi-static, thus reducing the complexity of the generalized viscoelastic equation of forced motion to the much simpler Hook's equation. The average levels of strain evoked in the tissue are very small, and perhaps most importantly, elastography is capable of producing high resolution images [17]. In ultrasound

elastography two different sets of RF data from the same region of interest (ROI) are collected and stored. First a conventional scan is made, then the tissue is compressed slightly, and another set of RF signals is collected. Two frames of ultrasound data are then recorded, one before and one after a section of tissue is compressed by a small amount (e.g. with the ultrasound transducer) as shown in Figure 3.1. The strain is derived by analysis of pre-compression and post-compression profile of the axial displacement along the RF signal, and several techniques are available for estimating the displacement in tissues. The resulting tissue displacement between the two sets of RF data is usually tracked by speckle tracking techniques, e.g cross-correlation methods. Despite the fact that the original concept of elastography involves applying an external load to the tissue, the inherent motion of organs and deformation of tissue can be utilized, which in turn has lead to new inventions in the fields of intravascular and cardiac elastography [25].

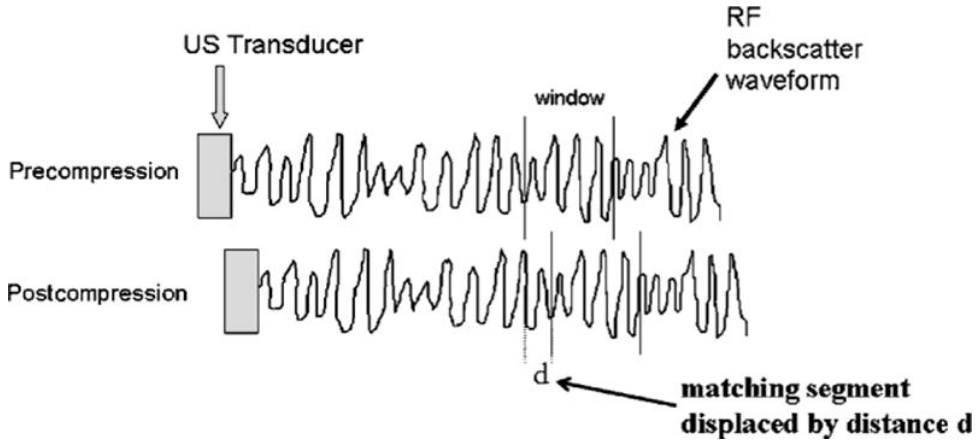

Figure 3.1: Basic principle behind elastography [1]

When a stress is applied to the tissue, it is being displaced and compressed. The local displacement of each particle along the direction of propagation of the ultrasonic beam, induces a shift in the time domain of the corresponding echo in the backscattered signal, due to changes in the time of flight. Assuming a constant speed of sound, the induced time shift is directly proportional to the local displacement. The relative displacement of tissue will be incremental and hence give rise to time shifts in the time delays of corresponding sections in the recorded ultrasound signals. Tracking and estimation of these time shifts will hence produce the corresponding displacement. The amount of shift in the signal equals the amount of tissue displacement at that point in the image frame, and this process is done for all points in the image. Ultrasound is an excellent imaging modality for elastography, whereas each image obtained from an ultrasound transducer has a unique speckle pattern. Speckle is an interference pattern visible in ultrasound images produced by the mutual interference of a set of wavefronts, and is dependent on the frequency of the transmitted pulse and its shape. Thanks to the distinct speckle pattern of the ultrasound images, time delay estimation can produce highly accurate estimates of the actual tissue motion [33]. When estimating the tissue displacement a window around the sample range is used to improve the estimate. The similarity within the sample window between a frame before and after pressure is applied, will tell us how much the signal, i.e. the tissue, has shifted for that range in the image. The most common way of finding this similarity is by using speckle tracking and cross-correlation techniques. The estimate of the actual time delay may then be found by estimating the shift of the peak of the cross-correlation function as displayed in Fig 3.2. Finding the maximum value of the cross-correlation function as l_{max}, and knowing the sampling period T_s, the corresponding time delay may be found as

$$l_{max} \cdot T_s = \hat{t} \tag{3.2}$$

However when the signal-to-noise ratio (SNR) is low, the probability of making errors in the estimation of the peak increases dramatically. Also another disadvantage using cross-correlation techniques include the sensitivity of cross-correlations to amplitude variations in the presence of small signal distortions. A different approach is to use the phase of the two signals to compute the delay. Wilson and Robinson described a method for phase tracking of wideband ultrasonic signals as early as 1982, and were able to measure displacement and deformation waveforms for displacements less than 0.1 cm [18]. At the start of 2008, Lindop et. al. presented a theoretical analysis and experimental results from an investigation of phase-based ultrasonic deformation estimators [19]. They were able to demonstrate their application to in vivo freehand strain imaging, and showed quantitatively that the approach offered a wider range of scanning conditions than adaptive methods based on correlation coefficients or sum of absolute differences.

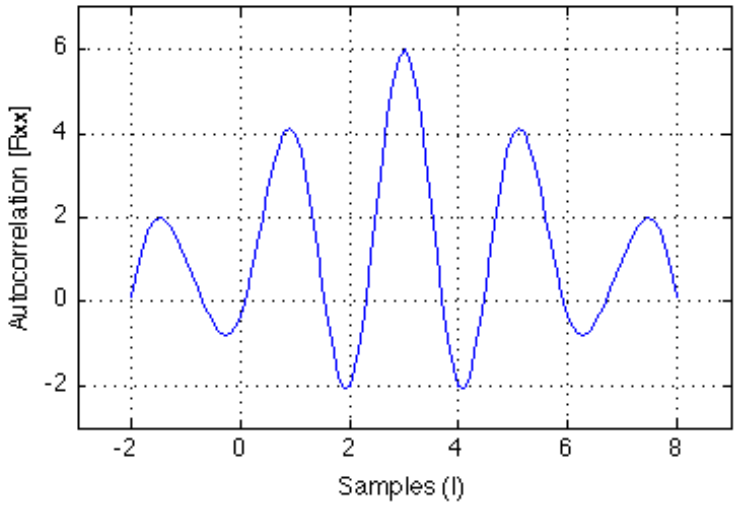

Figure 3.2: Cross-correlation within a sample window between two different frames . The peak of the function will yield the corresponding time delay

3.4 Relations of tissue displacement and tissue elasticity

The recorded displacement estimates are sometimes displayed directly as displacement images, but it is more common to take the spatial derivative of the displacement to produce the resulting strain between the acquired RF data before and after the applied compression. This resulting strain image is known as an elastogram, and the imaging technique is known as elastography. Each pixel in the elastogram, i.e. the elastography images, denotes the estimated amount of strain, ε, which the tissue experienced during the applied compression defined by

$$\hat{\varepsilon} = \frac{\hat{t}_1 - \hat{t}_2}{\Delta t} \tag{3.3}$$

where $\hat{t}_1$ and $\hat{t}_2$ denotes the estimates of the local tissue displacements spaced apart by the window shift Δt which is typically in the order of 0.1-0.2 mm [34]. The major disadvantage

of this method is the the noise induced by the gradient operation, and various methods have been proposed to decrease the noise using filtering. Also, using cross-correlation techniques for estimating time delays is based on the assumption of a constant displacement over the window range, while in fact the degree of local stretching and compression can be substantial and can degrade the estimates. The method presented in Section 2.1 is a phase based approach for subsample delay and displacement estimation, and makes no assumption on the local delay variation. Any parametric model can be used for the local delay variation, for instance a non-linear model as described by Eq. (2.60). The parameters of the model can be used to find the displacement a_k, and the gradient of the displacement b_k. The gradient of the displacement is connected to the mechanical properties of tissue, a small gradient is a sign of stiff tissue, and a large gradient is a sign of soft tissue. The tissue stiffness values are not quantitative but qualitative; only the relative tissue stiffness is visualized. As opposed to Eq. (3.3), the estimated strain, ε, by using the phase-based time-delay algorithm is given directly by the local rate of change of the model $\hat{\tau}(k)$, i.e.

$$\hat{\varepsilon} = \frac{\partial \hat{\tau}}{\partial k}(k) = b_k \tag{3.4}$$

As seen in Figure 3.3 the method is quite effective in displaying spheres that will appear isoechoic to the background using standard B-mode imaging. For this specific situation a non-linear model was chosen within a window length of 3.4 mm with a 10 MHz probe and a demodulation frequency of 6 MHz.

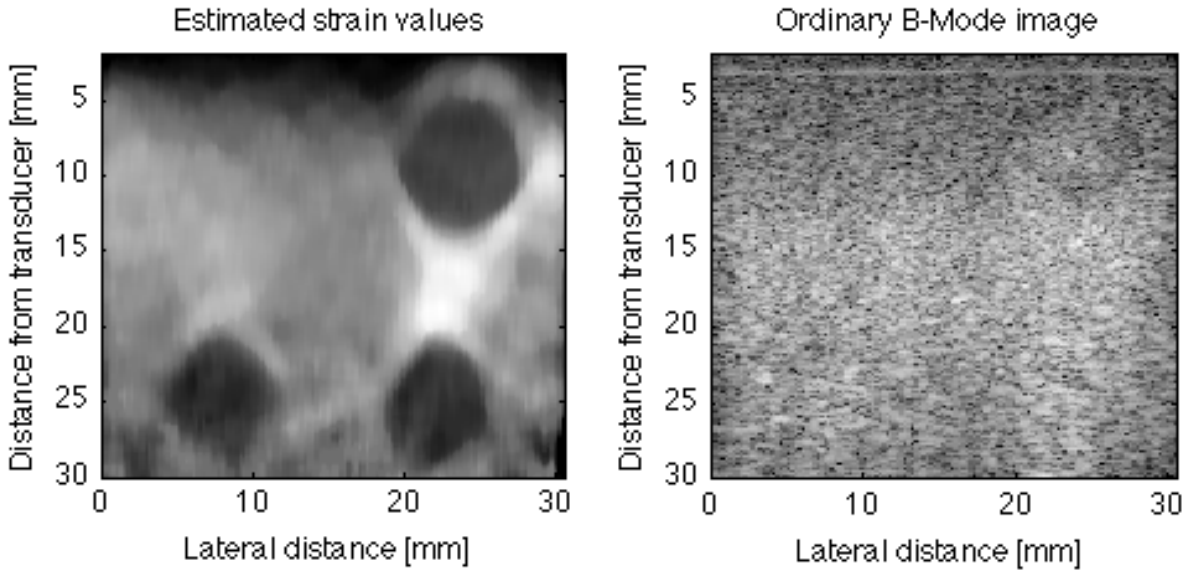

Figure 3.3: Elastogram made by using the phase-based time-delay algorithm with a non-linear model of $\hat{\tau}(k)$ as described by Eq. (2.60) within a window of size 3.4 mm. Recording made with a 10 MHz probe and a demodulation frequency of 6 MHz

Chapter 4

Impacts on elastogram quality for linear and nonlinear model of $\hat{\tau}$

For the results to be presented two different recorded data-sets are used. The first elastography recording is made by the Ultrasonix Medical Company, Vancouver, Canada, with a 10 MHz probe and a demodulation frequency of 6 MHz. The data-set consists of 30 frames, with each frame being made up of 192 scan lines and 1032 samples in the range direction. Each frame then has a total of 132 096 data points. The second recording is done at the Department of Circulation and Medical Imaging (ISB) with the Ultrasonix SonixRP system with a 10 MHz probe and a demodulation frequency of 4 MHz. The recordings were performed on a basic elasticity phantom as seen in Fig. 4.1 [2]. The model contains two sizes of spheres positioned at two different depths, and the spheres in the phantom will appear isoechoic to the background using conventional B-mode imaging. The recorded data-set consists of 50 frames, with each frame being made of 256 scan lines and 902 samples in the range direction, giving each frame a total of 231 424 data points. The elastography images are made by using the real-time delay-tracking algorithm developed for estimating spatially varying delays in RF signals, as described in Eq. (2.19), to track and estimate the local tissue compression based on the time shifts raised in the signal.

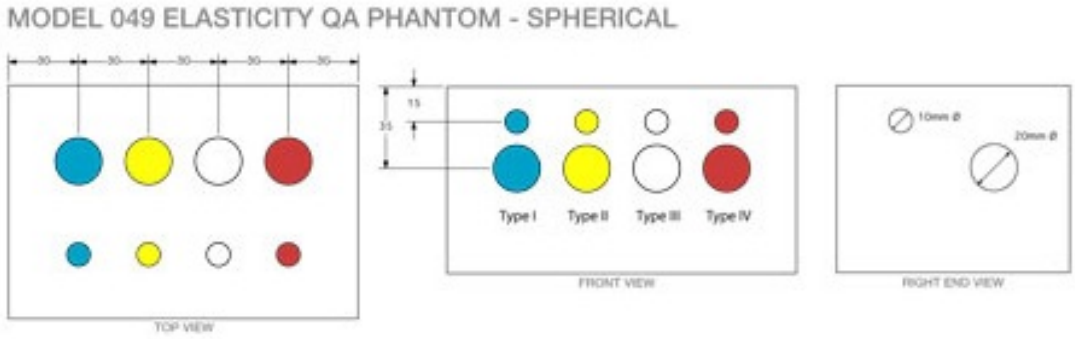

Figure 4.1: CIRS Model 049 ultrasound phantom used for elasticity imaging [2]. The phantom contains several spheres of different sizes and elasticity. The spheres will appear isoechoic to the background using conventional B-mode imaging

For post-processing adjustments of the strain values to be displayed, there are several possibilities. In order to avoid that very large negative or positive values from the estimated strain values

impair the dynamic of the final image, thresholding of the data is used. Also smoothing in the time and spatial domain is implemented to increase the smoothness of the sequence of frames to be displayed in the final movie, and to suppress noise. These results are already presented and discussed in [35], and will not be explored further. The two parameters to be tuned for the phase-based time-delay estimation algorithm, before any post-processing is performed, is the length of the sample window and the choice of model of the delay $\hat{\tau}(k)$.

All simulations, calculations and images were created using Matlab version R2008a by the Mathworks company [36], unless otherwise stated.

4.1 Choice of window length for phase based estimator

The window length is the number of samples N of the sample window for which the minimum values of the model $\hat{\tau}(k)$ is to be found. A too long sample volume could lead to too much smoothing of the final image, whereas a too short sample volume could lead to too close tracking of the noise in the image. There is hence a tradeoff between contrast and resolution. With fixed values for time and spatial domain smoothing the effects of the choice of window length for the elastography recording made by the Ultrasonix Medical Company can be seen in Figure 4.2, with window lengths ranging from 2.2 mm to 4.4 mm, which is the sample range in which the parameters $\hat{\beta}$ of the model $\hat{\tau}(k)$ is estimated. The strain values are in this case estimated by a linear model of $\hat{\tau}(k)$.

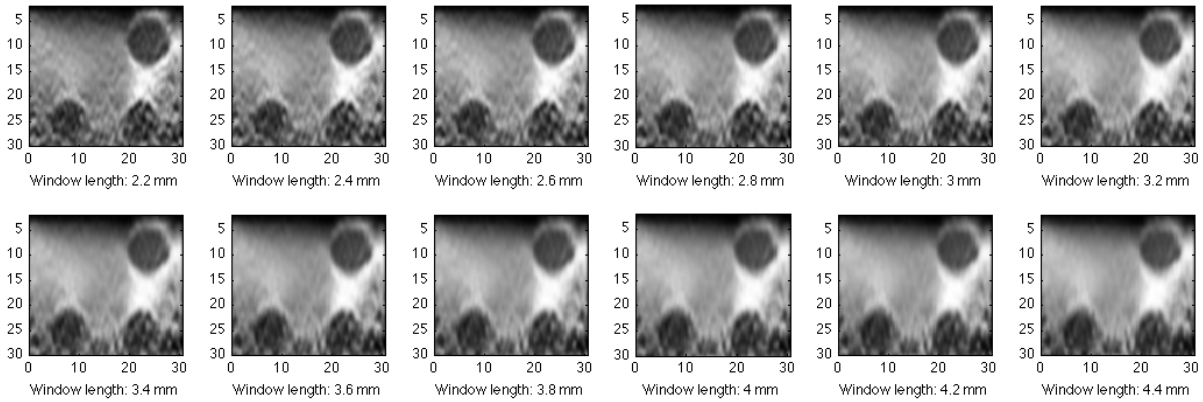

Figure 4.2: Elastogram made with different window lengths ranging from 2.2 mm to 4.4 mm. Recorded with a 10 MHz probe and a demodulation frequency of $f_d = 6$ MHz. Strain values estimated with a linear model for $\hat{\tau}(k)$

From Figure 4.2 it seems that a window length of 2.2 mm closely tracks the inclusions, but the final image will also contain a larger degree of noise as perceived by the observer. In contrast, a window size of 4.4 mm and above would seem to smear the resolution of the image too much. A compromise must then be established, and the best perceived image is found to be with a window length of 3.4 mm for this specific recording having a demodulation frequency of 6 MHz.

Focusing on the recording done at ISB, it is again possible to view the differences in choice of window length. The images displayed in Figure 4.3 have window lengths ranging from 3.8 mm to 6.0 mm, which is the sample range in which the parameters $\hat{\beta}$ of the linear model $\hat{\tau}(k)$ is estimated. Again a compromise between contrast and resolution has to be made, and

the optimal value for window length is found perceptibly at 5.0 mm for this specific recording having a demodulation frequency of 4 MHz.

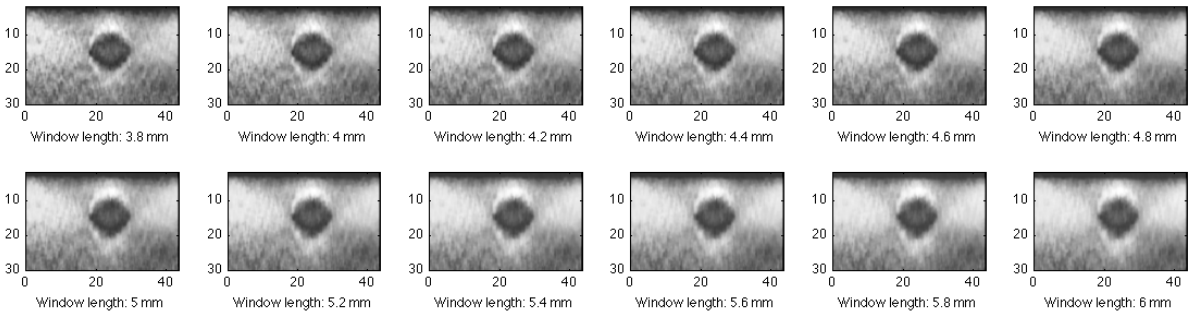

Figure 4.3: Elastogram made with window lengths ranging from 3.8 mm to 6.0 mm. Recorded with a 10 MHz probe and a demodulation frequency of $f_d = 4$ MHz. Strain values estimated with a linear model for $\hat{\tau}(k)$

It is clear that the two recordings have different optimal values for window length, and the challenge will be in finding a fixed, globally valid parameter to be used as window length. Instinctively, what seems to vary between the two recordings are the demodulation frequencies f_d. Now noting that the wavelength λ is related to the center frequency f_c, or in the case where the signal is demodulated the demodulation frequency f_d, as

$$\lambda = \frac{c}{f_d} \tag{4.1}$$

where c represents the propagation speed, which for soft tissue is approximately 1540 m/s. Seen on the left hand side of Figure 4.4 is a plot of the sample window in number of wavelengths as a function of window length in millimeter. Two lines are plotted representing two fixed frequencies of 6 MHz and 4 MHz respectively, with a fixed speed of sound of 1540 m/s. The 6 MHz line being the top blue line, and the 4 MHz line being the bottom blue.

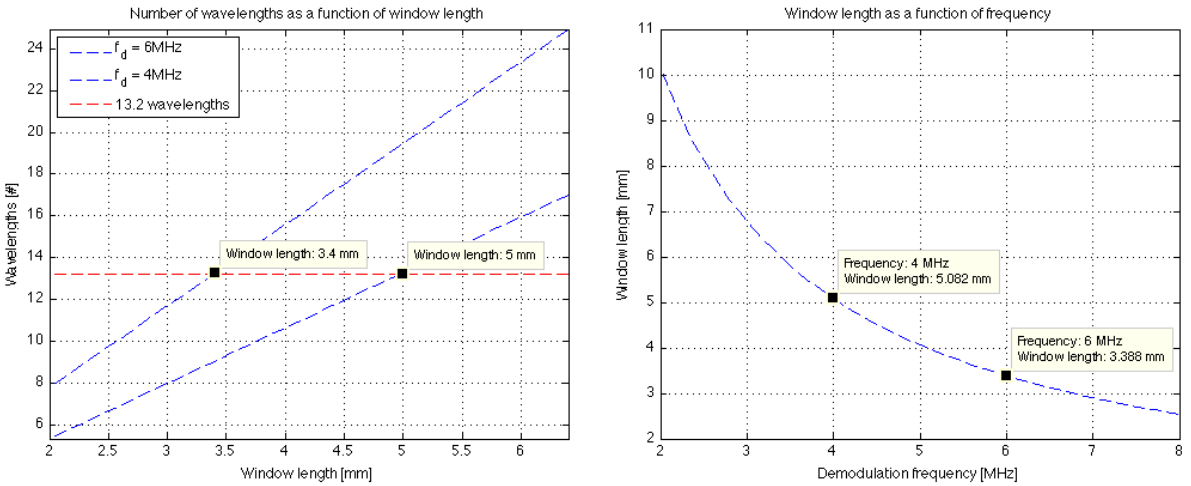

Figure 4.4: Number of wavelengths as a function of window length in millimeter for fixed frequency of 6 MHz and 4 MHz, and window length in millimeter as a function of demodulation frequency, both with fixed speed of sound as 1540 m/s

The best perceived image quality is obtained for a window length of 3.4 millimeter with a demodulation frequency of 6 MHz, and 5.0 millimeter for a demodulation frequency of 4 MHz. Converting these two window lengths into number of wavelengths, we get approximately 13 for both recordings, as represented by the horizontal red line in the plot on the left hand side of Figure 4.4. By setting the sample range, i.e. the size of the sample window, for a fixed number of wavelengths of approximately 13, we can plot the various window lengths as a function of demodulation frequency as seen on the right hand side of Figure 4.4. The results are intuitively seen, a lower demodulation frequency will give a larger window length in millimeter, whereas a higher demodulation frequency will give a smaller sample window in millimeter when operating with a fixed value for number of wavelengths.

This will have some implications on the computational time for the finished processed elastography images as a larger window length will lead to increased computational time. Displayed in Figure 4.5 is the computational time for the two different data-sets as a function of window length in millimeter. As the two data-sets vary both in frames, and number of data points in each frame, the computational time will also differ. The general trend is that an increase in window length gives an increased computational time, which is displayed by the two monotonically increasing graphs of Figure 4.5.

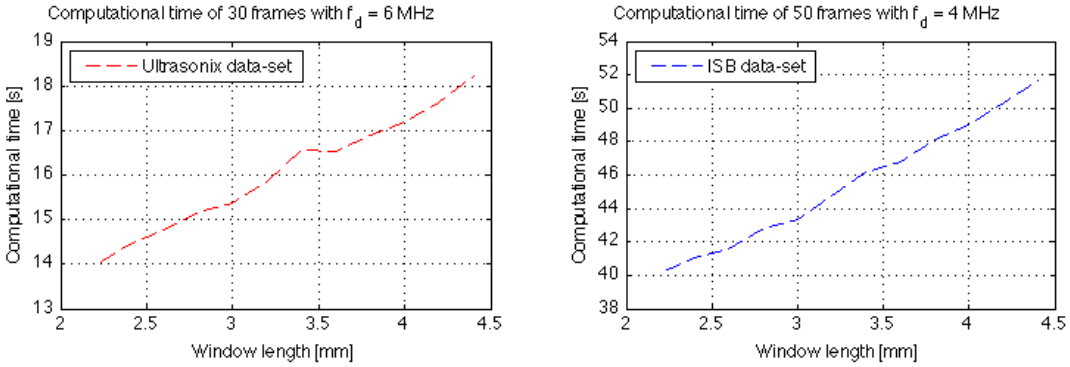

Figure 4.5: Computational time as a function of window length for the phase-based time-delay algorithm with a linear model. The first data-set consists of 30 frames with a demodulation frequency $f_d = 6$ MHz, whereas the second data-set consists of 50 frames with a demodulation frequency $f_d = 4$ MHz

4.2 Comparison of linear and non-linear model of $\hat{\tau}$ used on elastography data

Two models, one linear and one polynomial of the second degree, have been tested for the phase-based time-delay estimation algorithm as model of $\tau(k)$ described as

$$\hat{\tau}_{k,n} = a_k + b_k(n-k) \tag{4.2}$$

$$\hat{\tau}_{k,n} = a_k + b_k(n-k) + c_k(n-k)^2 \tag{4.3}$$

Both models can be stated in a minimum least squares sense, where the sum of squares is expressed as

$$Q = \sum_{n=k-\frac{N}{2}}^{k+\frac{N}{2}} w_n(\psi_n - \theta_n \hat{\tau}_{k,n})^2 \tag{4.4}$$

which has its solution matrix, i.e. the parameters, computed through Eq. (2.52) as

$$\hat{\beta} = \begin{bmatrix} a_k \\ b_k \end{bmatrix} \tag{4.5}$$

where a_k equals the smoothed estimate $\hat{\tau}(k)$, and b_k the local rate of change of the model, which can be seen on as the strain value ε. It is hence b_k, or the strain values, which are displayed in the final elastogram.

Displayed in Figure 4.6 is a series of frames from an elastography sequence computed from the data-set provided by Ultrasonix. The top row displays the sequence when estimated by a locally linear model of $\hat{\tau}(k)$ as stated in Eq. (4.2), while the bottom row displays the same sequence of frames computed from a locally polynomial model of the first degree as stated in Eq. (4.3). Both sequences are computed with the same window length, and the same parameters for thresholding and spatial and time domain smoothing.

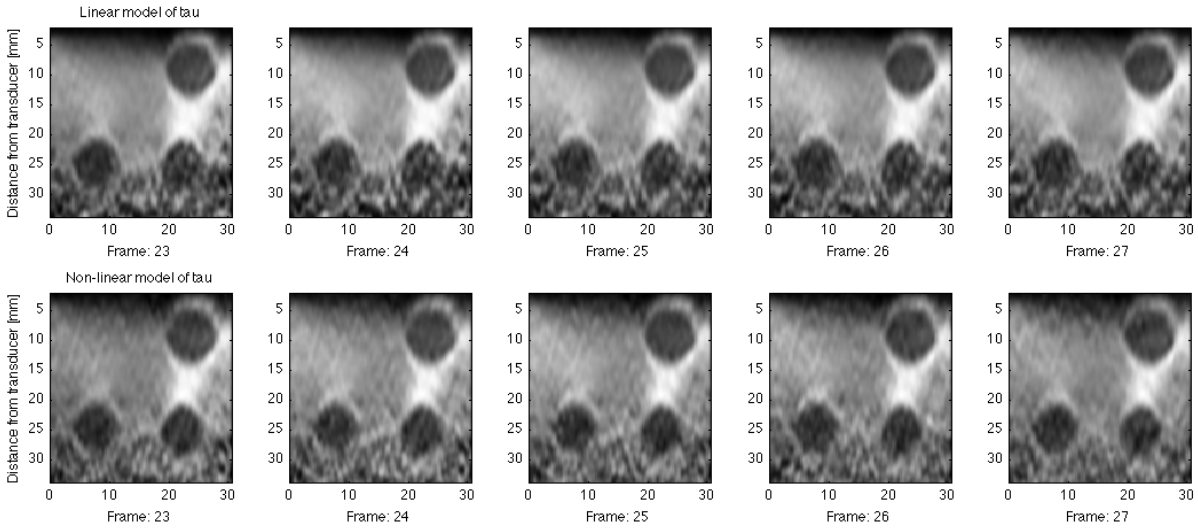

Figure 4.6: Sequence of frames from estimated elastogram with a linear model of $\hat{\tau}(k)$ (top row), and a polynomial model of $\hat{\tau}(k)$ (bottom row)

Initially the two sequences look virtually the same, especially when focusing on the areas close to the transducer surface. But what seems to be the main difference is observable at the bottom of the frames. It may seem that the frames computed from the linear model have a larger degree of noise present in this area than what is observable for the sequence at the bottom row computed by the non-linear model. As pressure applied on the phantom by the transducer is highest closest to the transducer surface, it will lose some of its impact as it propagates further down the tissue, as elastic tissue not only experiences compression in the range direction, but in all directions simultaneously. As elastograms are computed by the difference in strain from frame to frame, the estimations will be degraded if there is little or no strain present. This is observable at the very bottom of the top sequence of frames in Figure 4.6, where edge detection of the inclusions become increasingly difficult.

Focusing closer on various region of interests (ROI) of one frame computed by the linear and the non-linear model of $\hat{\tau}(k)$, it is possible to see the differences even clearer. Displayed in Figure 4.7 are three different ROIs of the elastogram, with the elastogram computed by a linear model at the top, and the elastogram computed by a polynomial model at the bottom. The frame at the left hand side of the figure displays the estimated elastography image, which is the same as the second image from the left in Figure 4.6, i.e. frame 24. The second frame of Figure 4.7 displays an ROI of the model's adaption to noise in the elastogram where there are no inclusions present. The last two frames display ROIs of the model's ability to detect edges in the image, i.e. detect the size and shape of the inclusions present.

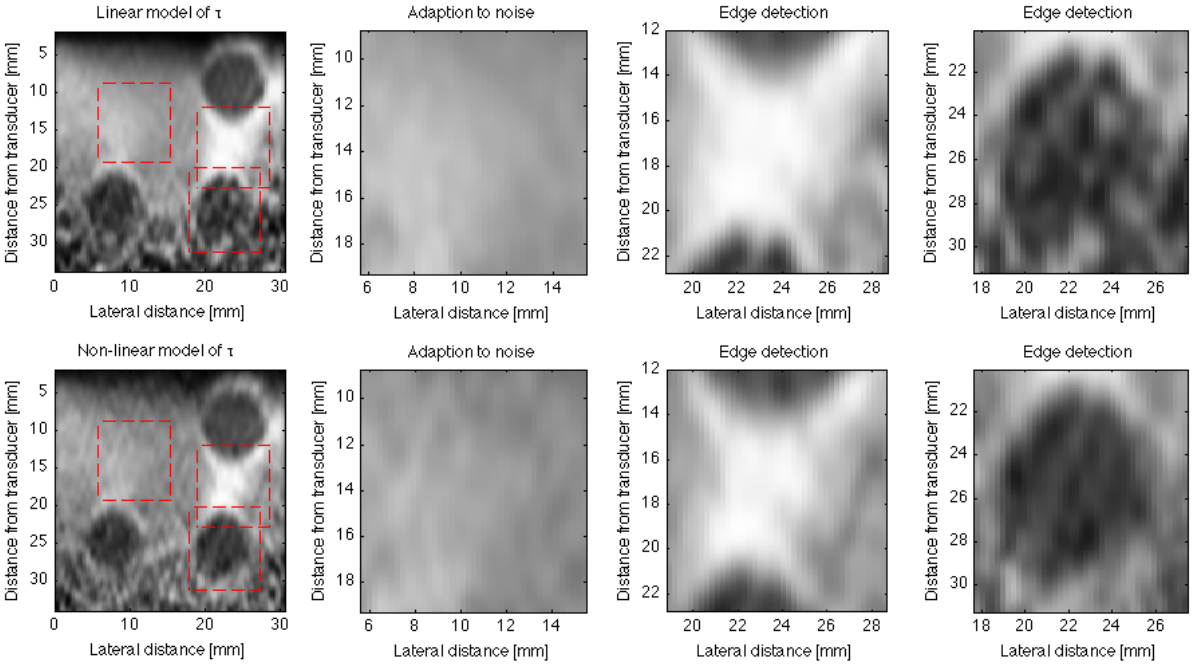

Figure 4.7: Various region of interests for elastogram estimated by a linear model (top row), and a polynomial model (bottom row). The first ROI displays how the two different models adapt to noise, whereas the last two ROIs displays edge detection for the two models

As seen from the second frame from the left for the top and bottom row, the polynomial model to a greater extent adapts to the noise in the image. This is the case where there are no differences in strain present, as the tissue hardness for this ROI is pretty uniformly distributed. As the polynomial model has a higher complexity than the linear, it is expected that it also will track small differences more closely. The unfortunate effect is that it also experiences a greater adaption to noise.

Turning attention to the the last two frames on the right hand side of Figure 4.7, the ability to detect edges is displayed more clearly. As seen in the third frame from the left, i.e. the second ROI, the bright area between the top and bottom inclusion of the elastogram is slimmer for the polynomial model than what is the case for the linear. This result can also be seen clearly in the sequence displayed in Figure 4.6. It may also seem that the polynomial model is better in detecting a clear difference between an inclusion and the surrounding tissue. This result is especially visible in the third ROI displayed on the right hand side of the figure, being the inclusion at the bottom right of the elastogram. For the linear model there is a lot of noise present, both inside the area of the inclusion, and in the surrounding tissue. This makes it more difficult to clearly distinguish the size and edges. Estimating the elastogram by a polynomial

model on the other hand is better in detecting these edges located at a depth where the strain is lower than closer to the transducer surface. Comparing the inclusion estimated by the two models one can clearly see an improvement by updating to a polynomial model. This result is also visible by again turning attention to the sequence of frames displayed in Figure 4.6 and focusing on the lower part of each frame.

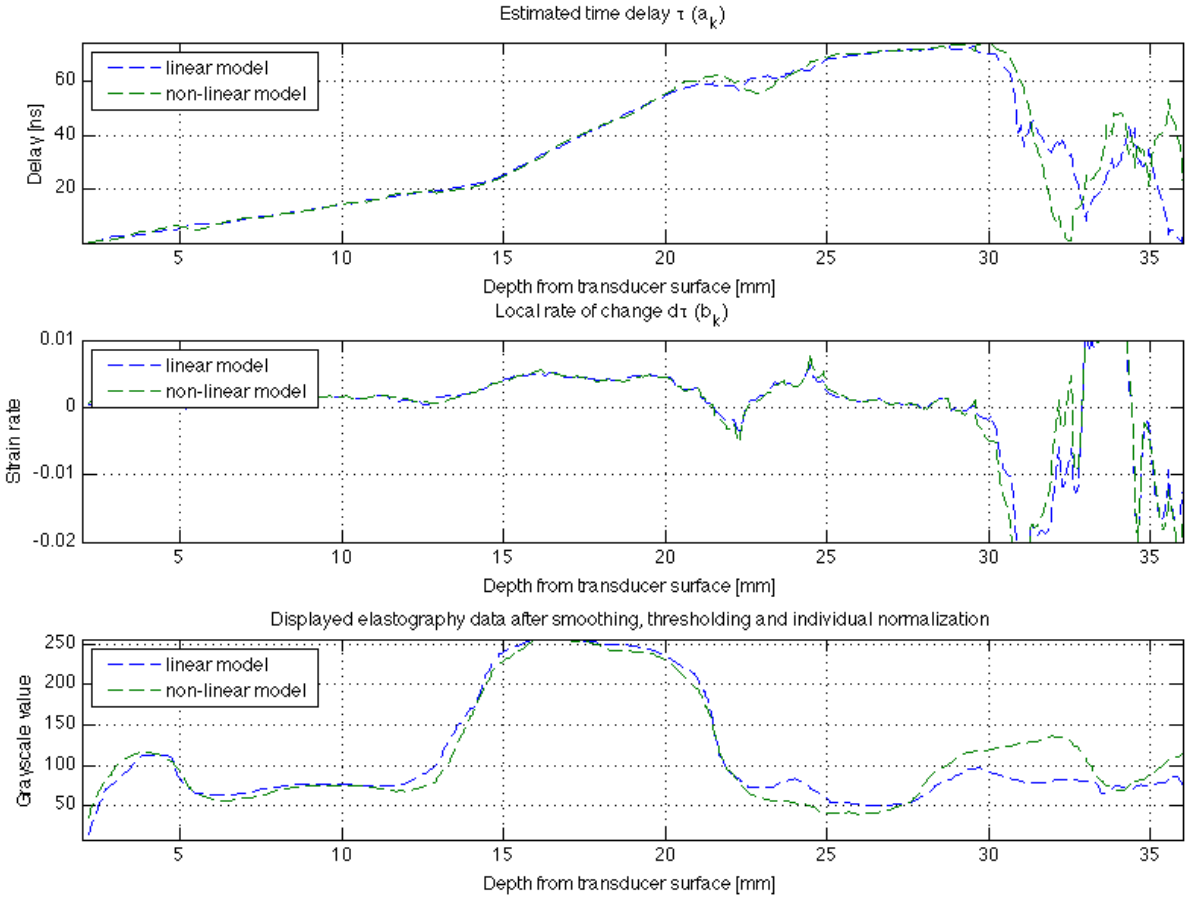

Figure 4.8: Estimated time delay $\tau(k)$, local rate of change ε, and final elastogram values for a single line through the image from top to bottom for the two different models of $\hat{\tau}(k)$

Seen in Figure 4.8 is a plot of single line going from top to bottom of the elastogram for the two various models. The estimated values from the linear model are plotted in blue, and the values from the polynomial model are plotted in green. The top row displays the estimated time difference $\tau(k)$, or the value of a_k from the model being used. The center row displays the local rate of change, i.e. the strain or the value of b_k of the model, and the bottom row displays the values after time and spatial domain smoothing, in addition to thresholding of data and individual normalization, has been performed. The final plot is hence the grayscale values that are displayed in the final elastogram. The line goes straight through the two inclusions on the right hand side of the image displayed in the left frame in Figure 4.7. This can also be seen from the bottom row of Figure 4.8, as a small gradient is a sign of stiff tissue, and a large gradient a sign of soft tissue. It is clear that the regions between 5-13 mm and 22-28 mm have small gradients, which is a sign of stiff tissue, which in turn is a sign of an object that is harder than the tissue surrounding it. As can be seen from the the plots of a_k and b_k on the top and middle row of the figure, the differences between the two various models of $\hat{\tau}(k)$ are especially distinguishable at a depth of around 30 mm and beyond.

The most interesting observation is even clearer when focusing on an ROI further down in the tissue as displayed on the bottom row of Figure 4.9, where the two delay models are clearly different. For this specific frame, and this specific line in the image, the largest difference occurs at a depth of around 3.2 cm, where the maximum difference is around 2.3 dB. Also the dynamic area, i.e. the difference between the maximum and minimum value of the signal, is different for the two models. The polynomial model has in this example a dynamic area of about 5.3 dB, and the linear model a dynamic area of 2.8 dB. This in turn yields that the polynomial model has a dynamic area being 2.4 dB higher than the linear model. This might suggest that the contrast of the displayed values is further improved by the use of a polynomial model. Although the corresponding dB values are for a single line within a specific frame, the main results are generally valid.

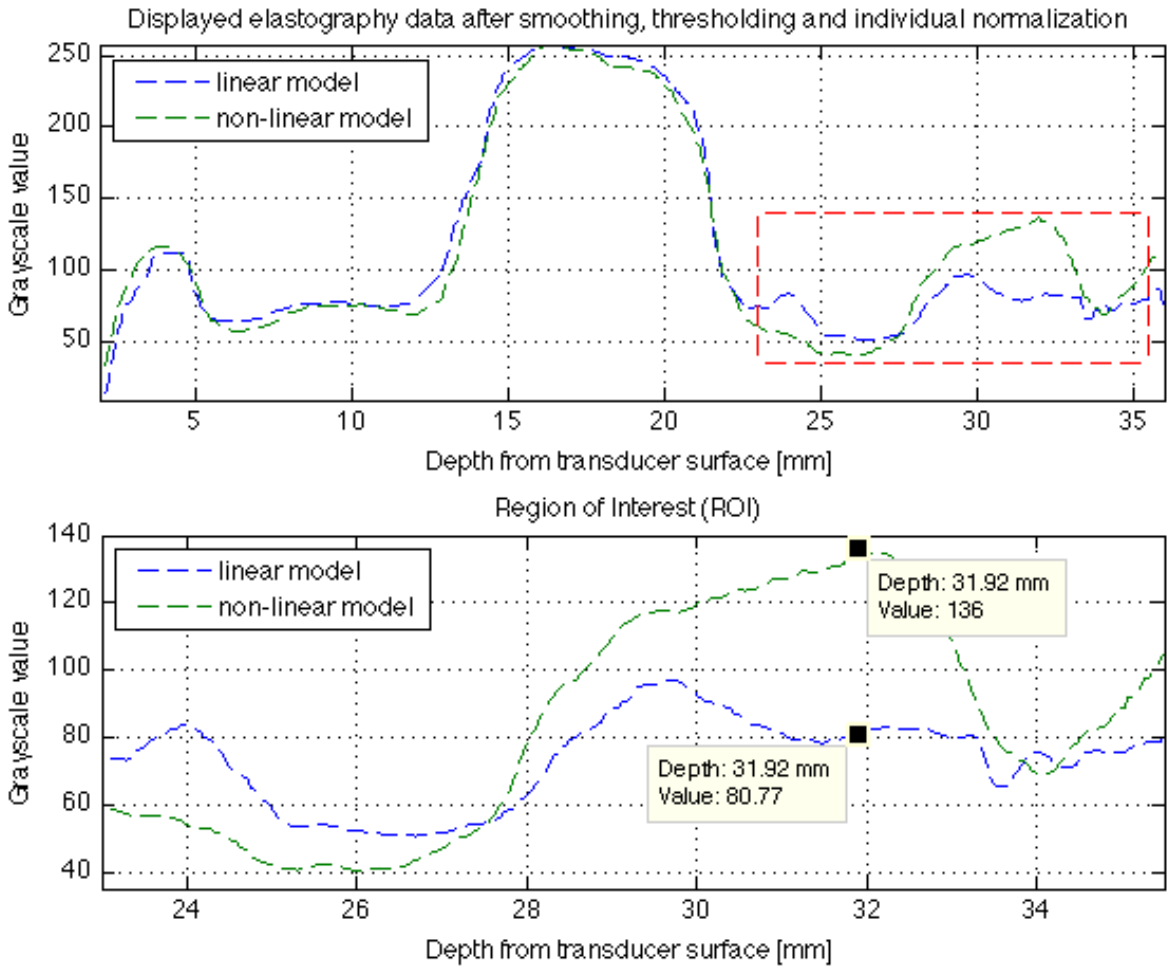

Figure 4.9: Final elastogram values for a single line through the image from top to bottom for the two different models of $\hat{\tau}(k)$

4.3 Improved noise suppression and edge detection by use of median filter for spatial filtering

As already discussed the quality of the elastogram is dependent on the presence of strain, and it seems the polynomial model is better in estimating small differences more closely compared to the linear model. As already seen, this also has the unfortunate effect of simultaneously adapting to the noise in the image. One way to overcome this problem, and simultaneously keep hold of the desired effect of improved edge detection when the pressure is low, i.e., when there is little strain present in the tissue, is by implementing a different approach when filtering in the spatial domain. The images displayed so far have been made using a gaussian weight matrix for the spatial averaging function. To observe the differences even clearer between the linear and non-linear model of $\hat{\tau}(k)$, the same series of frames as in Figure 4.6 are computed, but this time using a median filter for spatial filtering, which is a filter that calculates the median of neighboring pixels' values. The algorithm works by first storing the neighboring pixels in and array. The neighboring pixels are chosen to be within a window function of a certain size and shape, also known as a kernel. The next step is sorting the pixel values numerical, and the final step is picking the median from the sorted list as the pixel value. This process is done for all points in the image. Although the median filter has an algorithmic complexity of $O(r)$ in the kernel radius, it can be shown that a simple yet much faster algorithm exhibiting $O(1)$ runtime complexity can be achieved [37]. Seen in Figure 4.10 are the same frames as displayed in Figure 4.6, but this time median filtering is implemented. The main impact this has on the frames is that it increases the noise reduction by filtering out the so called salt and pepper noise. Salt and pepper noise is a form of noise typically seen in images appearing as randomly occurring white and black pixels.

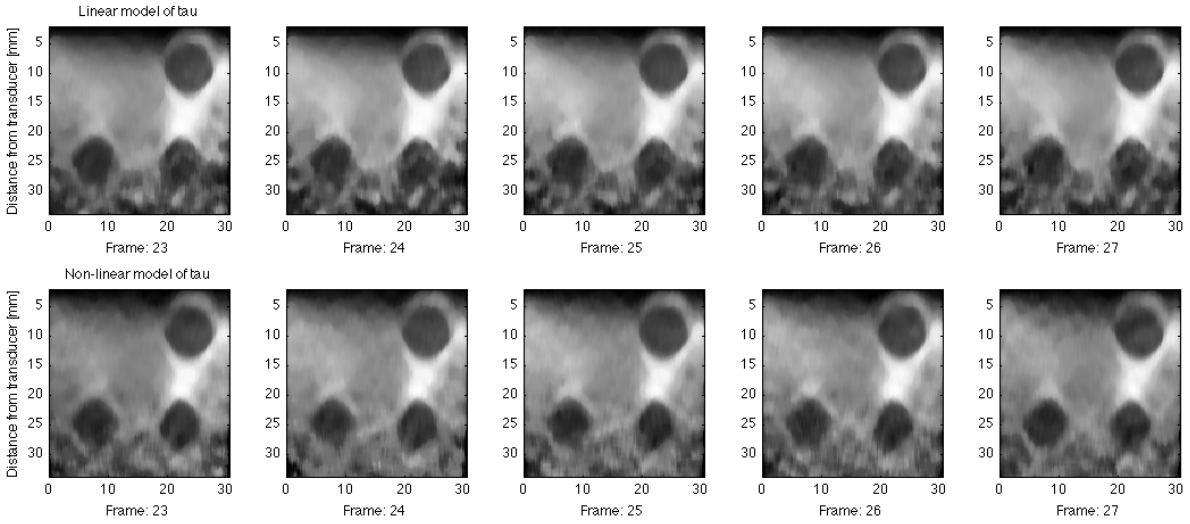

Figure 4.10: Sequence of frames from estimated elastogram with a linear model of $\hat{\tau}(k)$ (top row), and a polynomial model of $\hat{\tau}(k)$ (bottom row) and both sequences filtered by a median filter

Going into detail of the elastogram using the same ROIs as in Figure 4.7, it is easier to observe the differences between the two estimation models as displayed in Figure 4.11. The median filter has all but removed the problem with noise adaption for the polynomial model as seen in the first ROI of the figure. Once again the edge detection by using a polynomial model for $\hat{\tau}(k)$ is better than what is the case for the linear model. This can especially be observed by focusing on

the two inclusions on the bottom of each frame of Figure 4.10. The main difference however is the edge detection and contrast resolution of the inclusion displayed in the lower right corner of the elastogram. As already mentioned this area of the image experiences less strain than closer to the transducer surface. This means that time delay estimation from frame to frame, which also gives us the strain estimation, is increasingly difficult. This is especially clear for the linear model where both the edges and the contrast of the inclusion is corrupted by noise as seen from the frame on the right hand side on the top row of Figure 4.11. However the inclusion estimated by the non-linear model and displayed in the frame on the right hand side on the bottom row of the figure, is quite clear in both resolution and contrast. It would then seem that when there is little strain present, the polynomial model is much better in estimating differences in tissue stiffness than what is the case for a linear model.

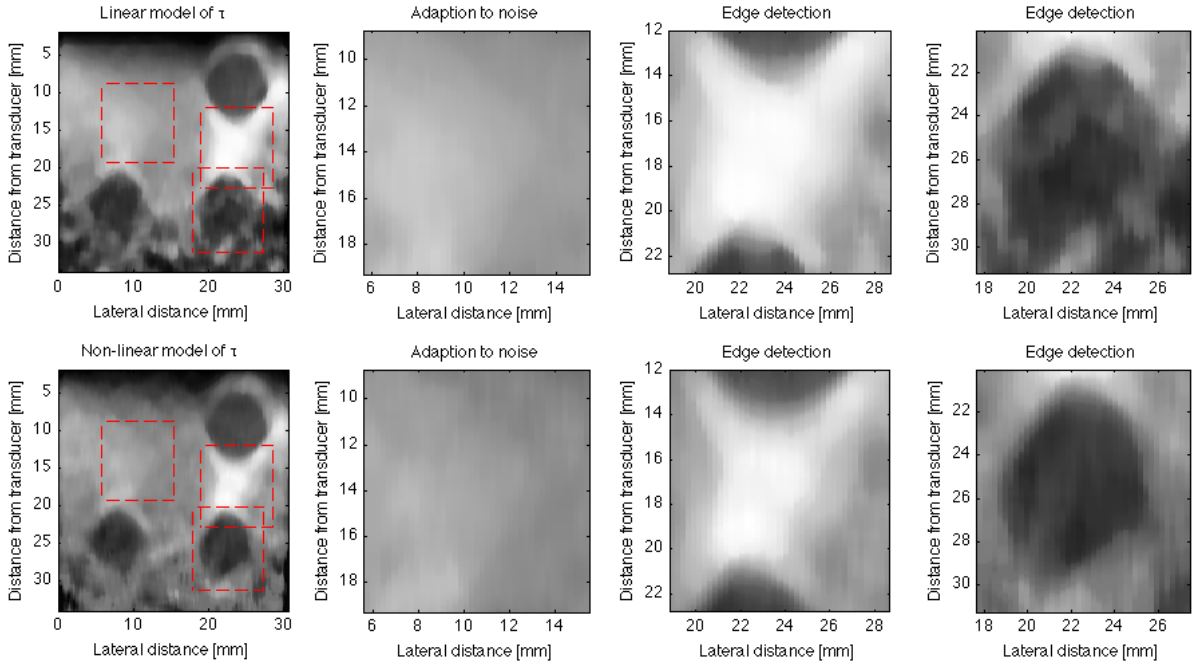

Figure 4.11: Various region of interests for median filtered elastogram estimated by a linear model (top row), and a polynomial model (bottom row). The first ROI displays how the two different models adapt to noise, whereas the last two ROIs displays edge detection for the two models

By selecting a single frame and focusing on the inclusions alone, as seen in Figure 4.12, the feasibility of the phase-based elastography estimator is quite evident. Although the recordings are done in vitro, thus making it an ideal imaging situation, an ultrasound imaging phantom usually has an attenuation coefficient of around 0.5 dB/MHz/cm which will have an impact on the signal strength. For a center frequency of 6 MHz, and a depth of 3 cm this corresponds to a drop in signal strength of around 10 dB. Nevertheless the two inclusions on the bottom left and bottom right of the first frame of Figure 4.12 are clearly distinguishable from the surrounding tissue.

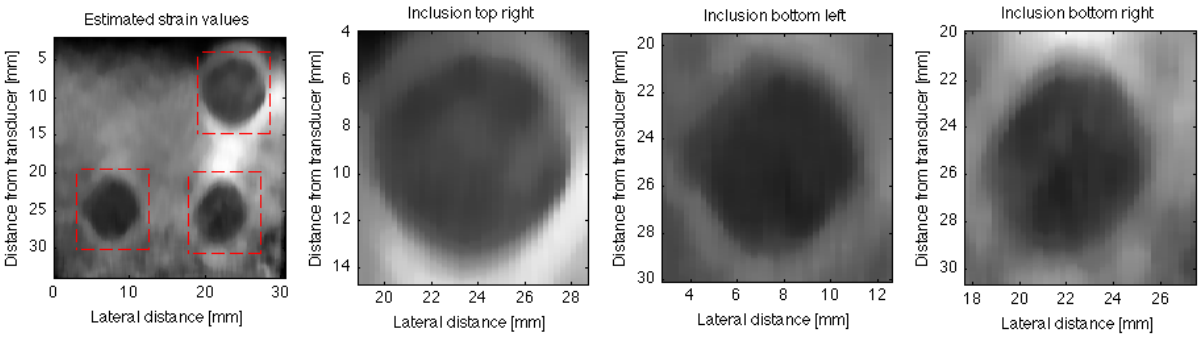

Figure 4.12: Various regions of interest for median filtered elastogram estimated by a polynomial model. The first ROI displays the inclusion on the top right, the second ROI displays the inclusion on the bottom left, and the third ROI displays the inclusion on the bottom right

Although updating the model of $\hat{\tau}(k)$ from a linear to a polynomial has great implications on the final quality of the elastogram, it also increases the computational time. Seen in Figure 4.13 is a plot of the computational time for a single frame as a function of window length for the two different models. As discussed in Section 4.1 a wider window length will also lead to an increased computational time. But also interesting is that updating to a non-linear model increases the computational time by a factor of 1.5, regardless of the window size. This means that the computational time by using a polynomial model of the first degree takes on average 50% times longer than what is the case when using a linear model as displayed in Figure 4.13.

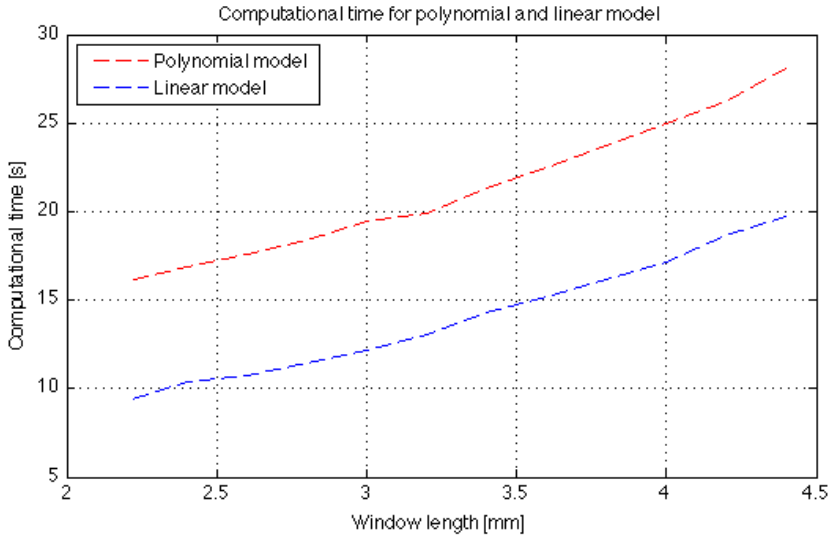

Figure 4.13: Computational time as a function of window length for the same data-set and for two models of $\hat{\tau}(k)$. The computational time for a polynomial model of the first degree is displayed in red, and the computational time for the linear model is displayed in blue

Chapter 5

SURF imaging

5.1 Principles of SURF imaging

The Second-order UltRasound Field imaging (SURF) technique is based on transmission of dual-frequency band pulses from the same acoustic source, and each SURF-pulse complex is composed of a high-frequency (HF) imaging and a low-frequency (LF) manipulation pulse. The pulses typically have a frequency separation greater than 1:7 in order to ensure approximately constant manipulation pressure over the imaging pulse length. The purpose of the LF pulse is to manipulate the scattering and propagation of the HF imaging pulse, and the HF pulse is then used to image tissue or nonlinear scatterers under the influence of the manipulation pulse. The LF content is removed by filtering, and the LF pulse is thus only transmitted and not received. The name SURF also indicates that the propagating pulse complex can be seen as a HF wave surfing on top of a LF wave [4, 38].

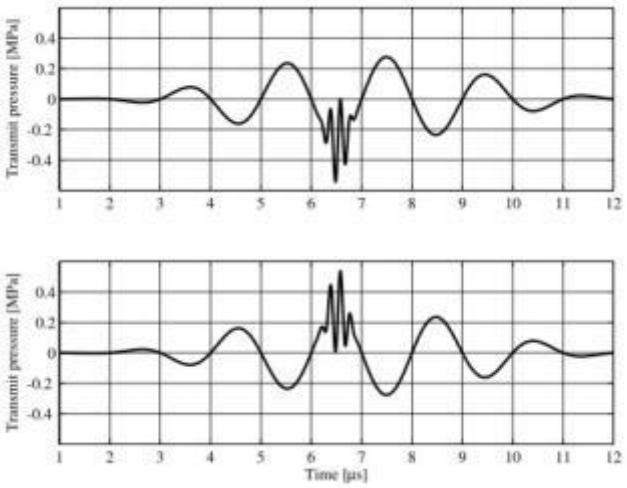

Figure 5.1: Illustration of two different SURF-pulse complexes with the high-frequency imaging pulse first placed in a compression phase of the low-frequency manipulation pulse, and then in a rarefaction phase

The most basic pulsing scheme is a two-pulse setting where the imaging pulse is first placed in a compression phase of the manipulation pulse, and then in a rarefaction phase as illustrated

in Figure 5.1. By combining the received signals and using adapted signal processing, such a pulsing scheme may be used as an ultrasound contrast detection method. Another approach is to compose a synthetic SURF transmit beam generated from the difference between two propagated pulse complexes fired in the same direction on different manipulation pressures and filtered around the imaging HF frequency. This method may be used for reverberation suppression.

5.2 Homogeneous linear wave equation

Wave propagation is derived from the cyclic exchange between dynamic (kinetic) energy given as the acoustic vibration velocity, and potential energy given as elastic energy stored when the material is compressed. The acoustic vibration velocity, i.e. the dynamic energy, may be written from the Newton acceleration law as

$$-\nabla p(r,t) = \rho \frac{\partial u(r,t)}{\partial t} \tag{5.1}$$

where u equals the particle velocity, p the pressure and ρ the mass density of the unstrained material. The potential energy is given as

$$-\nabla u(r,t) = \kappa \frac{\partial p(r,t)}{\partial t} \tag{5.2}$$

where κ equals the bulk compressibility which is the local compression of the fluid. Dropping the dependence on space r and time t for notational convenience, together these two equations give us the linear homogenous wave equation for the evolution of acoustic pressure p as

$$-\nabla p = \rho \frac{\partial u}{\partial t} \tag{5.3}$$

$$\nabla(-\nabla p) = \nabla(\rho \frac{\partial u}{\partial t}) \tag{5.4}$$

$$\nabla^2 p = -\rho \frac{\partial}{\partial t} \nabla u \tag{5.5}$$

$$\nabla^2 p = -\rho \frac{\partial}{\partial t}(-\kappa \frac{\partial p}{\partial t}) \tag{5.6}$$

$$\nabla^2 p = \rho\kappa \frac{\partial^2}{\partial t^2} p \tag{5.7}$$

$$\nabla^2 p - \rho\kappa \frac{\partial^2}{\partial t^2} p = 0 \tag{5.8}$$

$$\nabla^2 p - \frac{1}{c^2} \frac{\partial^2 p}{\partial t^2} = 0 \tag{5.9}$$

where the speed of sound is given as $c = 1/\sqrt{\kappa\rho}$, and the expression for the particle velocity, u, may be derived in the same manner.

5.3 Nonlinear wave propagation

The propagation of ultrasound waves is nonlinear, and different phenomenon that arise when diagnostic ultrasound waves propagate can not be explained on the basis of linear assumptions alone. These effects include a gradually progressive distortion of the acoustic waveform, the associated generation of components at harmonic frequencies of the fundamental, attenuation and acoustic shock formation. The local nonlinearity is small, but is accumulated during forward propagation due to variations in propagation speed over the waveform, causing distortion to develop with distance as seen in Figure 5.2. The effects appear most strongly in fluids with low acoustic attenuation, such as water, amniotic fluid or urine. Similar effects also appear in soft tissue, but are limited by absorption and scattering [39].

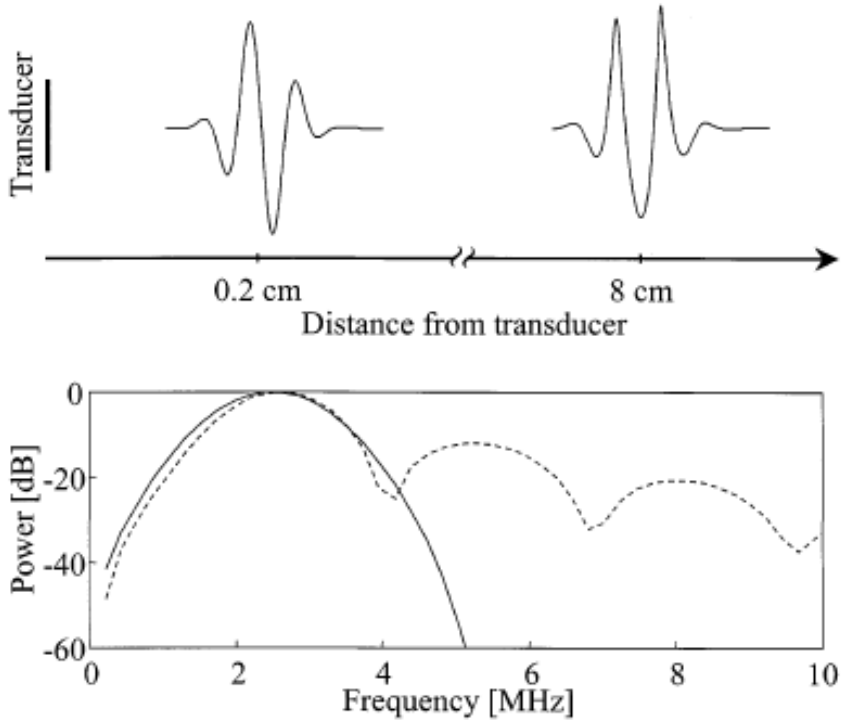

Figure 5.2: Effects of nonlinear propagation; distortion of the acoustic waveform, and the generation of components at harmonic frequencies of the fundamental [3]

In the literature, isentropic nonlinear elasticity is usually described by a Taylor-series expansion of the acoustic pressure p as a function of the mass density ρ. The entropy s is assumed constant, so that there exist no extrinsic or intrinsic heat conduction or viscous friction. The Taylor-development expresses the variations in pressure as a function of mass density in a medium, and represents the fact that mass density does not change linearly as the applied pressure is altered. In the physical world the nonlinear terms of elasticity have the implication that the medium gets stiffer, i.e. less compressible, as compression is applied. A second order expansion of the Taylor-development give us an expression for the isentropic nonlinear elasticity as

$$p = \left[\frac{\partial p}{\partial \rho}\right]_{0,s} (\rho - \rho_0) + \frac{1}{2}\left[\frac{\partial^2 p}{\partial \rho^2}\right]_{0,s} (\rho - \rho_0)^2 \tag{5.10}$$

where ρ_0 is the mass density of the unstrained material. By introducing the variable change

$\rho_1 = \rho - \rho_0$, the pressure, p, may be written as

$$p = \rho_1 \left[\frac{\partial p}{\partial \rho}\right]_{0,s} + \frac{\rho_1^2}{2}\left[\frac{\partial^2 p}{\partial \rho^2}\right]_{0,s} \tag{5.11}$$

$$= \rho_0 \frac{\rho_1}{\rho_0}\left[\frac{\partial p}{\partial \rho}\right]_{0,s} + \frac{\rho_0^2}{2}\left(\frac{\rho_1}{\rho_0}\right)^2\left[\frac{\partial^2 p}{\partial \rho^2}\right]_{0,s} \tag{5.12}$$

$$= A\frac{\rho_1}{\rho_0} + \frac{B}{2}\left(\frac{\rho_1}{\rho_0}\right)^2 \tag{5.13}$$

where the A and B parameters are defined as

$$A = \rho_0 \left[\frac{\partial p}{\partial \rho}\right]_{0,s} \tag{5.14}$$

$$B = \rho_0^2 \left[\frac{\partial^2 p}{\partial \rho^2}\right]_{0,s} \tag{5.15}$$

and the derivations are performed in unstrained material and with constant entropy. The continuity equation for mass in the Lagrange regime may be stated as

$$\rho \approx \frac{\rho_0}{1+\nabla\psi} \Rightarrow \frac{\rho}{\rho_0} = \frac{1}{1+\nabla\psi} \tag{5.16}$$

where ψ is the particle displacement vector, i.e., displacement of a particle from its equilibrium position. The relationship ρ_1/ρ_0 may then be written as

$$\frac{\rho_1}{\rho_0} = \frac{\rho-\rho_0}{\rho_0} = \frac{\rho}{\rho_0} - 1 = \frac{1}{1+\nabla\psi} - 1 = \frac{1-1+\nabla\psi}{1+\nabla\psi} = \frac{\nabla\psi}{1+\nabla\psi} \approx -\nabla\psi(1-\nabla\psi) \tag{5.17}$$

where the last approximation is valid for $\nabla\psi \ll 1$. Combining this last result with Eq. (5.13) we get

$$p = -A\nabla\psi(1-\nabla\psi) + \frac{B}{2}\left(-\nabla\psi(1-\nabla\psi)\right)^2 \tag{5.18}$$

$$= -A\nabla\psi + A(\nabla\psi)^2 + \frac{B}{2}(\nabla\psi)^2(1-\nabla\psi)^2 \tag{5.19}$$

$$= -A\nabla\psi + (A+\frac{B}{2})(\nabla\psi)^2(1-\nabla\psi)^2 \tag{5.20}$$

$$\approx -A\nabla\psi + A(1+\frac{B}{2A})(\nabla\psi)^2 \tag{5.21}$$

$$= -A\nabla\psi + A\beta_n(\nabla\psi)^2 \tag{5.22}$$

$$= -\frac{1}{\kappa}\nabla\psi + \frac{1}{\kappa}\beta_n(\nabla\psi)^2 \tag{5.23}$$

where the approximation in Eq. (5.21) is valid when neglecting terms with a higher order than two. By solving Eq. (5.23) with regards to $\nabla\psi$, we get the material equation for nonlinear tissue elasticity as

$$-\nabla\psi = \kappa p - \beta_n(\kappa p)^2 \tag{5.24}$$

The compressibility κ is defined as the inverse of A, and the parameter β_n decides the size of the nonlinear effect. β_n can be found experimentally for various materials [40], and is defined as

$$\beta_n = 1 + \frac{B}{2A} \tag{5.25}$$

Typical values of β_n and other acoustic parameters for typical soft tissue are given in Table 5.1 [6].

Material	β_n	$\kappa\,[10^{-12}Pa^{-1}]$	$\rho\,[kg/m^3]$	$c\,[m/s]$	Temp $[^\circ C]$
Blood	4	396	1025	1570	26
Fat	5.8-6.2	508	950	1440	37
Liver	4.34	385	1060	1560	37
Muscle	4.7	380	1070	1560	30
Spleen	4.9	385	1060	1560	30

Table 5.1: Nonlinearity parameter β_n and other acoustic parameters for typical soft tissues [6]

5.4 Homogeneous nonlinear wave equation

Now expanding the wave equation to the nonlinear case, the relation between the relative volume compression and the applied acoustic pressure p is given by the material or constitutive equation for nonlinear tissue elasticity as

$$\frac{\delta V}{\Delta V} = -\nabla\psi = \kappa p - \beta_n(\kappa p)^2 \tag{5.26}$$

where ψ is the displacement of a particle from its equilibrium position, V represents the volume, and $\beta_n = 1 + \frac{B}{2A}$ is the tissue nonlinearity parameter given as the first and second coefficient of the Taylor development of the non-linear wave equation. Hence the relative change in volume equals the derivative in multi-dimensional space of a particle from its equilibrium position, i.e. the particle velocity u equals $\nabla\psi$

Defining the momentum potential ϕ as

$$\rho u = -\nabla\phi \tag{5.27}$$

will in turn give from Eq. (5.1) that the pressure may be related to the momentum potential as

$$p = \frac{\partial \phi}{\partial t} \tag{5.28}$$

Now, starting with the material equation for nonlinear tissue elasticity Eq. (5.26), and using the definition of the momentum potential Eq. (5.27) and the relation between pressure and momentum potential Eq. (5.28) and noting that $u = \Delta\psi$ we get

$$-\nabla\psi = \kappa p - \beta_n(\kappa p)^2 \tag{5.29}$$

$$-\nabla u = \kappa \frac{\partial p}{\partial t} - \beta_n \kappa^2 \frac{\partial p^2}{\partial t} \tag{5.30}$$

$$-\nabla\left(-\frac{1}{\rho}\nabla\phi\right) = \kappa \frac{\partial}{\partial t}\left(\frac{\partial \phi}{\partial t}\right) - \beta_n \kappa^2 \frac{\partial}{\partial t}\left(\frac{\partial \phi}{\partial t}\right)^2 \tag{5.31}$$

Comparing equations Eq. (5.2) and Eq. (5.30), we see that Eq. (5.30) is the nonlinear equivalent of Eq. (5.2). The last term on the right hand side of Eq. (5.31) is the nonlinear term of the homogeneous nonlinear wave equation, which we can derive as

$$\frac{\partial}{\partial t}\left(\frac{\partial \phi}{\partial t}\right)^2 = 2\frac{\partial \phi}{\partial t}\frac{\partial^2 \phi}{\partial t^2} \tag{5.32}$$

Substituting this result in Eq. (5.31), and rearranging, we get

$$\nabla\left(\frac{1}{\rho}\nabla\phi\right) - \kappa\frac{\partial^2 \phi}{\partial t^2} + 2\beta_n\kappa^2\frac{\partial \phi}{\partial t}\frac{\partial^2 \phi}{\partial t^2} = 0 \tag{5.33}$$

$$\nabla\left(\frac{1}{\rho}\nabla\phi\right) - \kappa\left(1 - 2\beta_n\kappa\frac{\partial \phi}{\partial t}\right)\frac{\partial^2 \phi}{\partial t^2} = 0 \tag{5.34}$$

$$\nabla\left(\frac{1}{\rho}\nabla\phi\right) - \kappa\left(1 - 2\beta_n\kappa p\right)\frac{\partial^2 \phi}{\partial t^2} = 0 \tag{5.35}$$

Usually the mass density ρ varies with distance as $\rho(z)$ due to spatial variances of tissue. Imagining a situation without absorption, the mass density is uniform over the sample length, and the nonlinear wave equation may be expressed as

$$\nabla^2\phi - \kappa\rho\left(1 - 2\kappa\beta_n p\right)\frac{\partial^2 \phi}{\partial t^2} = 0 \tag{5.36}$$

The speed of sound may then be expressed as a function of pressure as

$$c(p) = \frac{1}{\sqrt{\kappa\rho(1 - 2\kappa\beta_n p)}} \tag{5.37}$$

which gives us the momentum potential for nonlinear propagation as

$$\Delta^2\phi - \frac{1}{c(p)^2}\frac{\partial^2 \phi}{\partial t^2} = 0 \tag{5.38}$$

where p is the total acoustic pressure.

5.5 Sound propagation and time delays as a function of acoustic pressure

Due to the nonlinear relationship between relative volume compression and applied acoustic pressure for tissue, the speed of sound for tissue is pressure dependent. For SURF imaging this means that if the imaging pulse travels close to a peak (or a through) on the manipulation pulse it experiences a nearly constant positive (or negative) manipulation pressure over its duration, resulting in an increased (or decreased) sound velocity. The LF manipulation pulse therefore generates a local change in the speed of sound experienced by the HF imaging pulse [41]. The propagation velocity as a function of pressure may be expressed as

$$c(p) = \frac{1}{\sqrt{\kappa\rho(1 - 2\beta_n\kappa p)}} = \frac{c_0}{\sqrt{1 - 2\beta_n\kappa p}} \approx c_0(1 + \beta_n\kappa p) \tag{5.39}$$

where κ is the bulk compressibility, ρ is the mass density, $\beta_n = 1 + \frac{B}{2A}$ is the tissue nonlinearity parameter given as the first and second coefficient of the Taylor development of the non-linear wave equation, and $c_0 = 1/\sqrt{\kappa\rho}$. The last approximation is valid when $\kappa\rho \ll 1$, which is the case for diagnostic ultrasound imaging [38].

For SURF imaging it is convenient to analyze the propagation velocity $c(p)$ by separating the total acoustic pressure p into two components

$$p = p_m + p_i \tag{5.40}$$

where p_m represents the LF manipulation pulse pressure, and p_i the HF imaging pulse pressure. Using the approximation in Eq. (5.39) and inserting the pressures gives

$$c(p) = c_0(1 + \beta_n\kappa p) = c_0(1 + \beta_n\kappa p_m + \beta_n\kappa p_i) \tag{5.41}$$

If the the frequency separation between the HF imaging pulse and the LF imaging pulse is large enough, i.e. the ratio f_i/f_m is high, the manipulation pressure experienced by the imaging pulse is approximately constant. The imaging pulse will then experience a speed of sound proportional to the manipulation pressure

$$c_i(p_m) \approx c_0(1 + \beta_n\kappa p_m) \tag{5.42}$$

An imaging pulse traveling in a compression phase of the manipulation pulse will thus propagate faster than if it was traveling in a rarefaction phase. This generates a time delay in the received HF signals from the two transmitted pulse complexes. The two signals transmitted under different manipulation pressures will thus be delayed with respect to each other, and the delay will be varying with depth. This relative time shift between them will be small at shallow depths, but is accumulated during forward propagation. Figure 5.3 displays the estimated delay from the transmission of two pulses with the HF pulse located on either a high or low pressure of the LF pulse. As seen from the figure these delays are small close to the transducer surface, and accumulate during forward propagation.

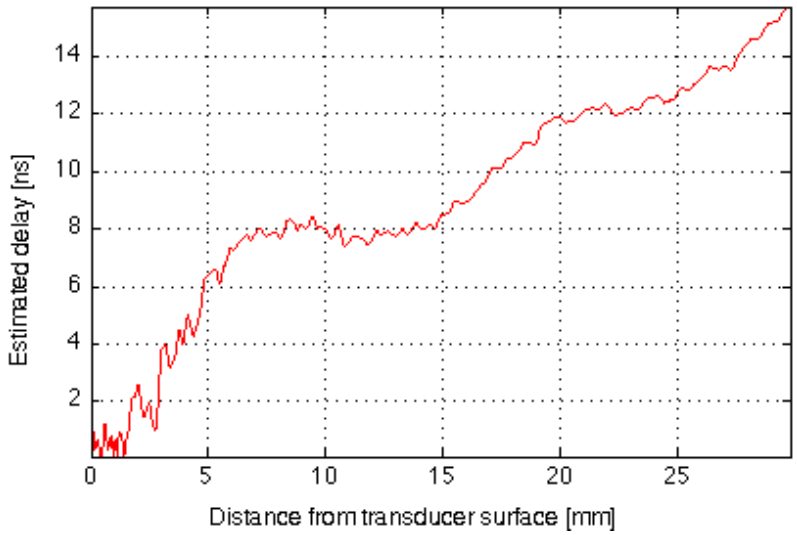

Figure 5.3: Estimated time-delay by the phase-based time-delay estimation algorithm from the most basic SURF pulsing scheme; a two-pulse setting with the imaging pulse first placed in a compression phase of the manipulation pulse, and then in a rarefaction phase

Now trying to develop an expression for the variable delays between the two pulses, we first begin by expressing the relationship between distance z, speed of sound c, and time t, and using the fact that the speed of sound varies with pressure and distance as in Eq. (5.39), we get

$$z = ct = c(z_0, p)t = \int_0^t c(z_o, p)\,\mathrm{d}t_0 \tag{5.43}$$

$$= \int_0^t c_0[1 + \beta_n \kappa p(z_0)]\,\mathrm{d}t_0 \tag{5.44}$$

$$= c_0 \int_0^t \mathrm{d}t_0 + c_0 \int_0^t \beta_n \kappa p(z_0)]\,\mathrm{d}t_0 \tag{5.45}$$

$$= z_0 + \Delta z \tag{5.46}$$

Δz is then a change of perceived depth from where the echoes are originated as result of the imaging pulse being placed on a manipulation pulse with a different manipulation pressure. By performing the following variable change $\mathrm{d}t_0 = \mathrm{d}z_0/c_0$ we can rewrite Eq. (5.45) as

$$z = z_0 + \int_0^z \beta_n \kappa p(z_0)\,\mathrm{d}z_0 \tag{5.47}$$

$$= z_0 + \Delta z \tag{5.48}$$

This result states that if an imaging pulse experiences a manipulation pressure switched from $p(z)$ to $-p(z)$ between the two shots needed to form the SURF beam, the propagation difference will be an added factor which is dependent on the manipulation pressure, the local compression of the medium and the tissue nonlinearity parameter. Due to amplitude reduction of the reflected or scattered LF pulse, the imaging HF pulse experiences negligible sound speed manipulation after scattering. We can therefore derive an expression for the time-delay between the two pulses

considering how the delays only occur at half the total length of the pulse-echo propagation distance

$$\tau(z) = \frac{2\Delta z}{c_0} = \frac{2}{c_0}\int_0^z \beta_n \kappa p(z_0)\,\mathrm{d}z_0 \tag{5.49}$$

A different approach is to compute the time-delay between the two pulses propagating with different sound velocity directly. This is done by finding the difference in pulse travel-time, where t_- and t_+ denotes the time of flight for a traveling pulse with negative and positive manipulation pressure respectively. The time difference as a function of distance and pressure may then be established

$$\tau(z) = t_- - t_+ = \frac{z}{c_-} - \frac{z}{c_+} = \int_0^z \frac{1}{c_-(z_0)} - \frac{1}{c_+(z_0)}\,\mathrm{d}z_0 \tag{5.50}$$

where c_- and c_+ denotes the speed of sound for a low and high manipulation pressure respectively. Again using the relation of speed of sound and pressure as given in Eq. (5.39) the above expression may be written as

$$\begin{aligned}
\tau(z) &= \int_0^z \frac{1}{c_0[1-\beta_n\kappa p(z_0)]} - \frac{1}{c_0[1+\beta_n\kappa p(z_0)]}\,\mathrm{d}z_0 && (5.51)\\
&= \int_0^z \frac{c_0[1+\beta_n\kappa p(z_0)] - c_0[1-\beta_n\kappa p(z_0)]}{c_0^2[1-\beta_n\kappa p(z_0)][1+\beta_n\kappa p(z_0)]}\,\mathrm{d}z_0 && (5.52)\\
&= \frac{1}{c_0}\int_0^z \frac{1+\beta_n\kappa p(z_0) - 1 + \beta_n\kappa p(z_0)}{1+\beta_n\kappa p(z_0) - \beta_n\kappa p(z_0) - [\beta_n\kappa p(z_0)]^2}\,\mathrm{d}z_0 && (5.53)\\
&\approx \frac{2}{c_0}\int_0^z \beta_n\kappa p(z_0)\,\mathrm{d}z_0 && (5.54)
\end{aligned}$$

where the last approximation is valid for small $\beta_n\kappa p$. Typical values of the tissue nonlinearity parameter, β_n, in human tissue are 6 for fat and 4.7 for skeletal muscle, while the bulk compressibility, κ, typically is $508\cdot10^{-12}$ and $380\cdot10^{-12}$ Pa^{-1} respectively. Thus $\beta_n\kappa$ in fat and skeletal muscle is around $3\cdot10^{-9}$ and $1.8\cdot10^{-9}$ Pa^{-1} [6]. Assuming $\beta_n \backsim 5$, $\kappa \backsim 450\cdot10^{-12}$ Pa^{-1} and a constant sound velocity of $c = 1540$ m/s, we get the typical delays for various manipulation pressures given as

P [MPa]	0.1	0.5	1	1.5	2
$\frac{\Delta\tau}{z}$ $[\frac{ns}{cm}]$	2.9	14.6	29.2	43.8	58.4

Table 5.2: Theoretical values of time delays in nanoseconds per centimeter as a function of manipulation pressure assuming $\beta_n \backsim 5$, $\kappa \backsim 450\cdot10^{-12}$ Pa^{-1} and a constant sound velocity of $c = 1540$ m/s

where the delays are given in nanoseconds per centimeter, and the manipulation pressure is in MPa. Typically for a constant epxerienced pressure $p = 1$ MPa the sound speed change is $\Delta c \approx 0.2$ to 0.3 % of c_0. If $c_0 = 1540$ m/s the delay between two pulses after 2 cm of propagation is $\backsim 50$ to 60 ns.

The time delays are crucial for several aspects of SURF imaging. For SURF contrast imaging this delay has to be estimated and corrected for, which also improves the tissue suppression of

the SURF imaging method. Also if the delay $\tau(z)$ can be estimated, the signal can be corrected and used to extract the nonlinear signal. Estimates of new imaging parameters like $\beta_n\kappa$, which is a measure of the compressibility and stiffness of the medium, may then be established. Quantification of tissue is then possible by assuming a relation between delay and tissue parameters as $\Delta\tau = f(p, \beta_n\kappa)$. Since the time delays are accumulative as a function of depth, this allows for the generation of a synthetic transmit beam by subtraction of the delayed pulses without doing any time-delay corrections. This beam has the same type of characteristics as a harmonic beam and may be used for suppression of nearfield reflectors and sidelobe reduction. In addition the estimation of nonlinear scattering, temperature change, aberration and density (e.g. in oil or gas) is possible.

Chapter 6

Reverberations

6.1 Theory of multiple scattering

Ultrasound assumes that an echo returns to the transducer after a single reflection, and that the depth of an object is related to the time it takes the traveling pulse to hit the reflective surface of the object and return to the transducer surface. However, due to the inherent nature of wave propagation, ultrasound imaging may present some features, i.e. artifacts, that may lead to misinterpretation of the collected data. For instance, heterogeneities in the tissue produce multiple scattering of the propagating pulse as part of the wave is reflected back and forth several times between tissue layers before returning to the transducer. This is due to differences in acoustical impedances of the different tissue layers, and the detected echo does not run the shortest sound path because it bounces back and forth between the object and the transducer. The sequential echoes will take longer to return to the transducer, and the ultrasound processor will erroneously place the delayed echoes at an increased distance from the surface of the skin. These echoes infer with the main received signal which is scattered only once, and may greatly impair the contrast resolution of the final image, as they appear as additive noise at deeper depths than their true originals are located. A variety of artifacts can occur due to reverberations, where the most common is a severe loss of image contrast.

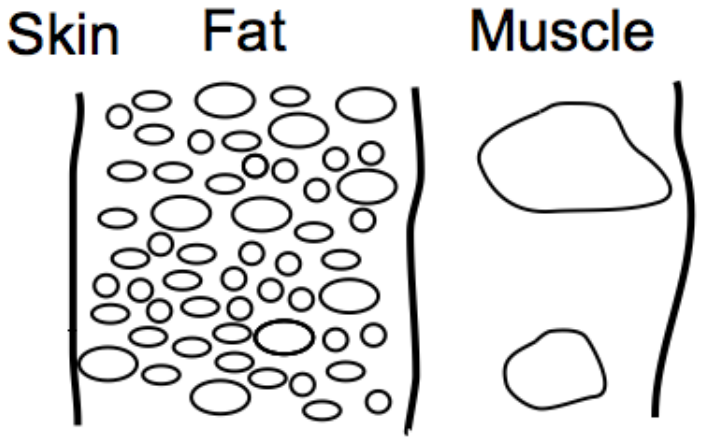

Figure 6.1: Physical structure of the body wall consisting of layered tissue close to the skin, and irregular mixtures of muscles, fat and connective tissue.

Multiple scattering is also known as reverberations, and are especially visible in the near field and imaging through the body wall due to the layered structure of the tissue close to the skin, and the irregular mixtures of muscles, fat and connective tissue of the body wall as displayed in Figure 6.1. Reverberations may then be viewed as acoustic noise or distortion introduced in the image by the inherent inhomogeneous structure of soft tissue. Due to its appearance, the artifact is also referred to as ring-down artifact and comet tail artifact. The presence of these reverberations is a source of artifacts that can hinder the correct analysis of ultrasound signals and images. Besides adding additive noise to the final image, they can also introduce errors in the quantitative parameter estimation in fields such as biological tissue characterization [27, 42].

6.2 Reverberation classes

As already stated, most reverberations are especially visible in the near field near the body wall, but reflections, or multiple scattering, may also occur when the first reflection takes place within the imaging region. To categorize the various reverberation types, the reverberation propagating paths can roughly be divided into three different classes depending on where the first scattering or reflection takes place, and related to how the components are suppressed in 2nd harmonic imaging. The amplitude of the 2nd harmonic components increase with depth, and is very low close to the transducer. Hence if the first scatterer is so close to the transducer that the 2nd harmonic component of the transmitted pulse is still low, harmonic imaging will suppress multiple scattering of this type. The propagation path examples are given in Fig. 6.2, and all paths have a total length of $2z_i$, so the corresponding image artifacts will appear at the imaging depth z_i.

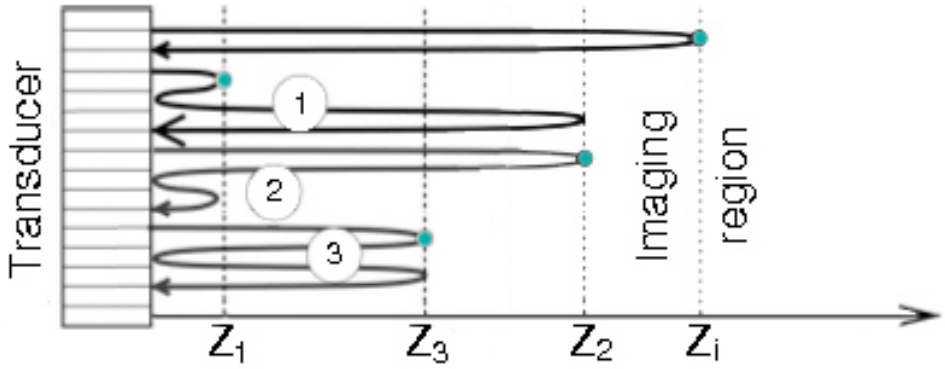

Figure 6.2: Direct wave propagation (upmost path) and reverberations of class 1, 2, and 3 (2nd to 4th path). Figure adapted from [4]

As seen from the figure the upmost path is based on the assumption that the propagating pulse returns to the transducer after a single reflection within the imaging region. This is the ideal imaging situation without any multiple scattering artifacts appearing in the final ultrasound image.

The first class of reverberations, as seen from the second path on the figure, experiences a reflection close to surface of the skin in the near field, causing it to be reflected back to the transducer surface. The propagating pulse is then reflected from the transducer surface down to the imaging region, before it returns to the transducer. The object within the imaging region

could for example be the carotid artery, and Class 1 reverberations are often found as noise inside the artery.

The second class of reverberation is seen from the third path on the figure. Here the pulse is first reflected from a structure in front of the object, like the body wall. But in addition the propagation is followed by a second reflection from a structure close to the transducer, often caused by the transducer array itself, followed by at least a third reflection from a second layer within the near field. With carotid imaging, Class 2 reverberations can be found as noise inside the artery, similar to Class 1 reverberations.

The final class describes a pulse that never propagates down to the imaging region, but rather is reflected back and forth between a strong reflective layer situated at half the distance to the imaging region z_i. The class includes a first scattering from a structure in front of the object (like in the body wall), followed by a reflection of this back scattered signal from a strong near field structure (for example the transducer array), followed by at least a third scattering from a second structure in the region on front of the object. The basis for this class of reverberations are that both the first and the third scatterers are so close to the transducer that limited 2nd harmonic component of the transmitted field is developed. Class 3 reverberations are for example the noise found in the apical region in cardiac imaging.

The different reverberation classes are described in detail in Table 6.1

Propagation path	First scattering	Second scattering
Direct wave	z_i	-
Class 1 reverberation	z_1	$z_2 = z_i - 3z_3/2$
Class 2 reverberation	z_2	z_1
Class 3 reverberation	$z_3 = z_i/2$	z_3

Table 6.1: Reverberation classes with total path length $2z_i$ in all cases. Adapted from [4]

6.3 Mimicking multiple reflections

6.3.1 Bacon as reverberation model

An attempt of mimicking a situation in which multiple reflections occur can been done by adding a tissue mimicking layered structure between the transducer and an ultrasound phantom before recording. As seen in figure 6.3 this structure consists of tissue from a pig, commonly known as bacon.

Figure 6.3: Tissue from a pig as reverberation model

By cutting the piece of bacon in appropriate sizes, it is possible to use one of those slices as a

form of reverberation model as seen in figure 6.4. The transmitted ultrasound signal will hence have to travel through this initial layered tissue of muscle and fat, before it enters the phantom. This again will produce reverberations which are visible in the final ultrasound image.

Figure 6.4: Imaging on phantom with bacon as reverberation model

6.3.2 Water and silicon plate as reverberation model

A downside when using biological tissue, or in this case pig bacon, as reverberation model, is the presence of fat in the tissue. Fat attenuates the signal to a large extent, and may introduce problems with keeping the signal-to-noise ratio high enough in order to collect valuable results. An attempt to circumvent this unwanted effect, is to use a silicon plate as reverberation model as seen in Figure 6.5. The silicon plate lies in water on top of the phantom to create the reverberations. A downside is the fact that we are less likely to encounter the three different types of reverberations as described in Section 6.2.

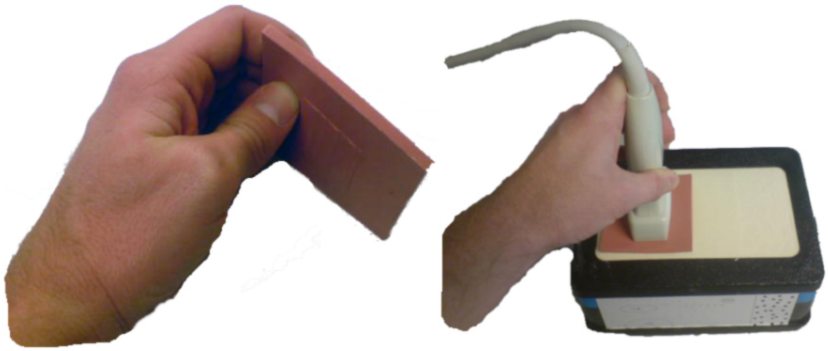

Figure 6.5: Silicon plate as reverberation model

6.3.3 Computer simulations of reverberations

A third option is to simulate the reverberations after the recorded RF signal has been obtained as seen in Figure 6.6. The reverberations are simulated as a replica of the signal over a certain depth as seen on the right hand side of the figure. The advantage of simulating the reverberations on the computer is that we are ensured not to loose signal power, as opposed to when the ultrasound wave has to pass through an initial reverberation layer. In addition the reverberations can easily be tailored to match perfectly on top, and not above, the region of interest.

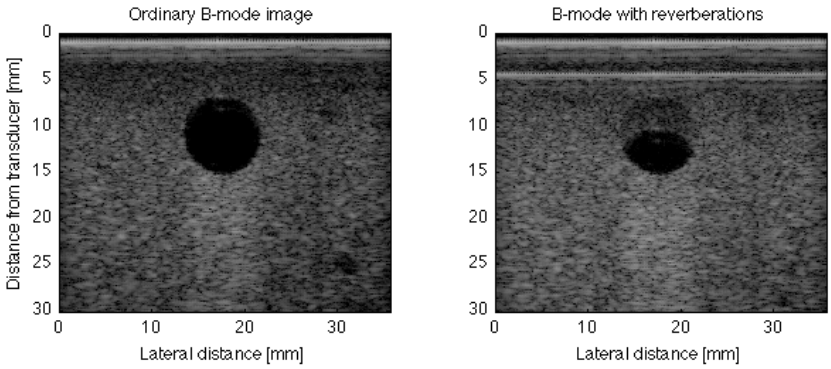

Figure 6.6: Simulating reverberations in Matlab

6.4 Effects of reverberations on recorded B-mode images

B-mode images from the CIRS model 050 nearfield phantom [5] with and without a reverberation model between the transducer and the phantom are recorded. Especially the effect the reverberations have on a 10 mm cyst-like volume situated with its center at a depth of approximately 10 mm from the phantom surface is studied. Seen in figure 6.7 are the two different imaging situations. On the left hand side is a B-mode image where the reverberation model is not applied. For this situation one can clearly see the contrast between the cyst-like volume and its surroundings. On the right hand side the layered tissue structure between the transducer and the phantom is applied. For this situation, where the reverberation model is used, one can clearly se how a ghost image of the layered structure on the surface is appearing at deeper depths, and for this situation, ruining the resolution of the 10 mm volume in the middle of the phantom.

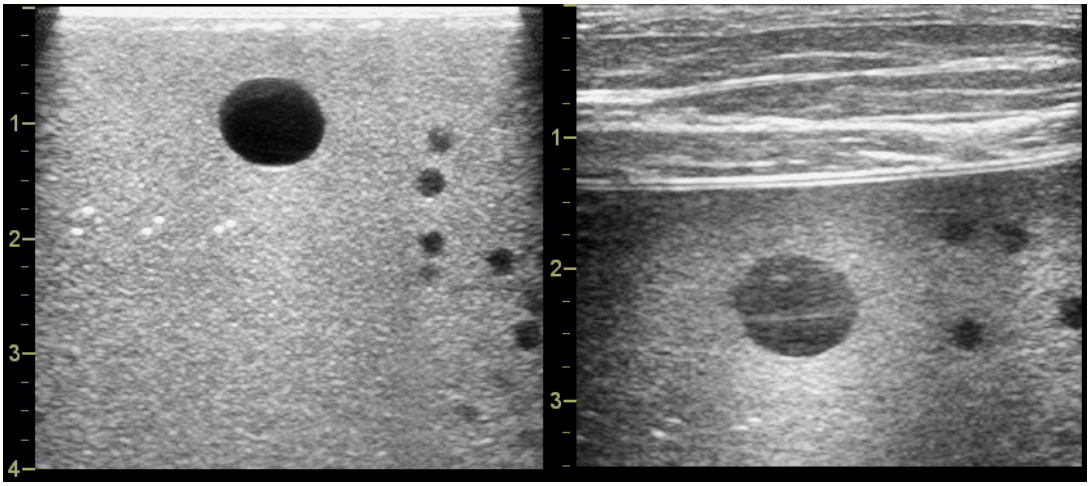

Figure 6.7: B-mode image of phantom with and without reverberation model

6.5 Effects of reverberations on estimated elastography images

By applying the reverberation model on top of the CIRS elastography phantom, it is possible to witness the effect reverberations have for impairing time delay estimates and then also the

final elastogram. All recordings are done with the Ultrasonix SonixRP system with a 10 MHz transducer. Seen in figure 6.8 is a recording with the Ultrasonix elastography mode turned on on the scanner.

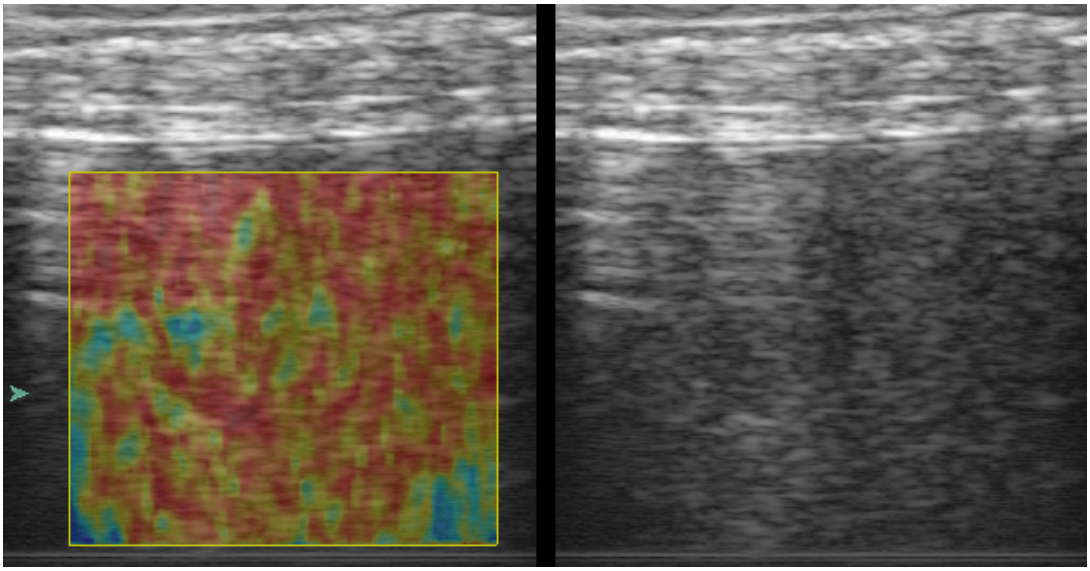

Figure 6.8: Elastography recordings with Ultrasonix method with reverberations

As seen on the right hand side of the figure one can catch a slight glimpse of the inclusion being a tad darker than the surrounding tissue in the middle of the figure. Also the reverberation model can be easily spotted on top of the figure. The elastography image, seen on the left hand side of the figure, on the other hand does not show this inclusion at all. Clearly the reverberations greatly impair the contrast resolution of the final image, and ghost echoes appearing at deeper depths, as seen in figure 6.7, ensure that the estimated time delays are false and the inclusion in the phantom is indistinguishable from the surrounding tissue.

Chapter 7

Reverberation suppression capabilities of SURF

7.1 Signal model without reverberation suppression

When scatterers in the tissue being analyzed by an ultrasound pulse are moving, we get a Doppler delay between pulses in slow time with constant beam direction as

$$\tau_d = \frac{2v_r T_s}{c} \tag{7.1}$$

where T_s is the pulse repetition frequency (PRF) period, and v_r is the radial velocity component of the scatterers. This delay may also be viewed on in an elastography sense as the delay originating due to applied pressure to the skin, and the elasticity of tissue. The signal with reverberations may then be expressed as

$$y(t) = x_l(t - \tau_d(z_i)) + r_1(t - \tau_d(z_1)) + r_2(t - \tau_d(z_2)) + r_3(t - \tau_d(z_3)) + n(t) \tag{7.2}$$

where x_l represents linear 1st order scattering, r_1, r_2 , and r_3 are the reverberations of Class 1-3 of the linear scattering, and $n(t)$ represents noise that is uncorrelated in the slow time. As described by the equation the Doppler delay is a function of distance from the transducer surface, where the distances z_i, z_1, z_2, z_3 are the same as seen in Figure 6.2 and described in Table 6.1. This also means that the delay due to elasticity is different for various regions of the tissue. We assume that the elasticity delay is low close to the transducer surface, which leads to the delay at this depth, $\tau_d(z_3)$, being zero. Also the Doppler delays may be stated as a function of time rather than distance, and Eq. (7.2) may be stated as

$$y(t) = x_l(t - \tau_d(t_i)) + r_1(t - \tau_d(t_1)) + r_2(t - \tau_d(t_2)) + r_3(t) + n(t) \tag{7.3}$$

7.2 Reverberation suppression method of SURF imaging

The SURF pulse complexes, composed of a HF imaging and a LF manipulation pulse, are utilized for reverberation suppression by taking advantage of a sound speed change introduced by the

LF pulse. As stated in section 5.5 and equation (5.49), two HF pulses which are transmitted on respectively the compression and rarefaction phase of the LF pulse will be delayed in respect to each other, and this delay will be varying with depth. This relative time shift between them will be small at shallow depths, but is accumulated during forward propagation.

The two received band-limited pulses with different time delays may then be described in the 1D case without loss of generality as

$$x(t) = s\left(t + \frac{\tau}{2}\right) \tag{7.4}$$

$$y(t) = s\left(t - \frac{\tau}{2}\right) \tag{7.5}$$

where $s(t)$ is the original non shifted signal. Taking the fourier transform of the two signals they can be stated in the frequency domain as

$$X(\omega) = S(\omega)e^{i\omega\frac{\tau}{2}} \tag{7.6}$$

$$Y(\omega) = S(\omega)e^{-i\omega\frac{\tau}{2}} \tag{7.7}$$

where ω is the center angular frequency. For SURF imaging with reverberation suppression, the synthetic SURF pulse is composed of the difference between two pulses sent on different manipulation pressures, thus producing different time delays. The synthetic SURF pulse may then be stated in the frequency domain as

$$S_d(\omega) = X(\omega) - Y(\omega) \tag{7.8}$$

$$= S(\omega)\left[e^{i\omega\frac{\tau}{2}} - e^{i\omega\frac{\tau}{2}}\right] \tag{7.9}$$

$$= S(\omega)i2sin\left(\omega\frac{\tau}{2}\right) \tag{7.10}$$

where the relation $e^x - e^{-x} = 2isin(x)$ comes from Eulers formula. Taking this result back in the time domain, the final SURF signal with reverberation suppression can be stated as

$$s_d(\omega, t, \tau) = \underbrace{2sin\left(\omega\frac{\tau}{2}\right)}_{G(\omega,\tau)} \mathfrak{Im}\left\{x(t)e^{i\omega t}\right\} \tag{7.11}$$

That is we have an additional gain factor $G(\omega, \tau)$ regulating the amplitude of $s_d(\omega, t, \tau)$ relative to the original non-shifted signal $s(t)$. The maximum and minimum absolute values of this gain factor are 2 for $\omega\tau = \pi$ and 0 for $\omega\tau = 0$.

For an imaging situation the LF manipulation experienced by the HF pulse depends on both the spatial coordinate $\vec{r}$ and the time t. The propagation time difference $\tau(\vec{r})$ accumulated between the two HF pulses is thus a space-dependent field. To generate a difference HF field $s_d(\vec{r}, t)$ being suppressed at shallow depths and amplified within the imaging region, the LF pulse transmission should be tailored to make $\tau(\vec{r})$ small at shallow depths, and $\sim \frac{\pi}{\omega}$ within the imaging region [4]. A simulation of the pressure from the SURF pulse alongside the pressure from an ordinary

ultrasound wave being focused at 10 mm is displayed in fig 7.1. It is clearly shown how the pressure close to the transducer, and the region in which reverberations are likely to occur, is suppressed by as much as up to 40 dB for the synthetic SURF transmit beam in comparison to an ordinary ultrasound pulse.

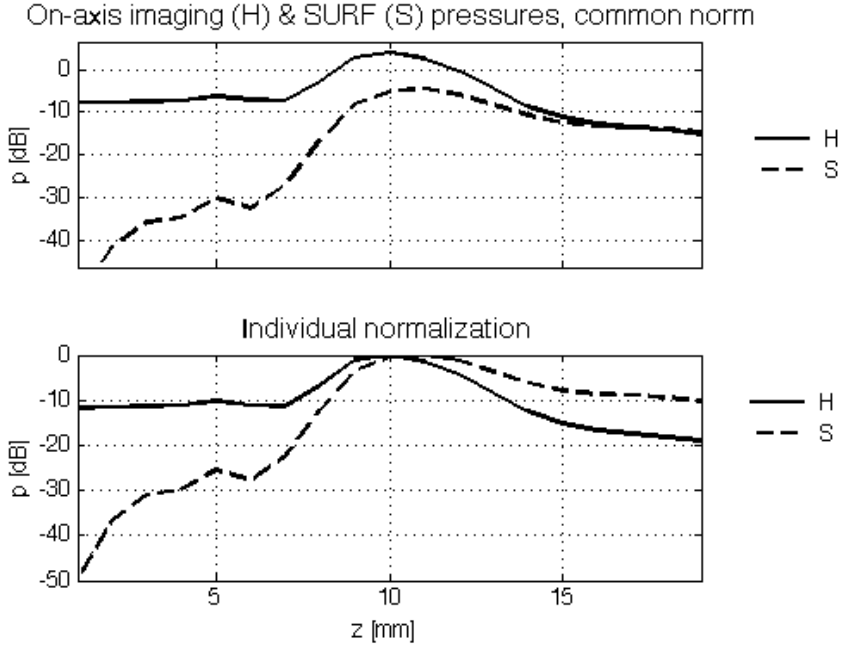

Figure 7.1: On axis pressure field from SURF and ordinary ultrasound pulse

7.3 Signal model with reverberation suppression

We assume a LF manipulation pressure of the form $a_k p_0(r)$, where a_k is an amplitude parameter that varies between pulses (k is the slow time pulse number coordinate) and r is the range coordinate. The pulse number then varies as

$$a_k = (-1)^{k+1} \tag{7.12}$$

which again gives a nonlinear propagation delay as $a_k \tau_n$, where the delay due to the synthetic SURF beam may be expressed as

$$\tau_n(t) = \frac{1}{c_0} \int_0^{\frac{c_0 t}{2}} \beta_n(s) \kappa_a(s) p_0(s) \, \mathrm{d}s \tag{7.13}$$

The complete SURF signal model including reverberations with stationary reverberation scatterers and moving object scatterers is then

$$\begin{aligned} y_k(t) = {} & x_l(t - a_k \tau_n(t_i) - k\tau_d(t_i)) + a_k x_n(t - a_k \tau_n(t_i) - k\tau_d(t_i)) \\ & + r_2(t - a_k \tau_n(t_2) - k\tau_d(t_2)) + r_1(t - k\tau_d(t_1)) + r_3(t) + n_k(t) \end{aligned} \tag{7.14}$$

where x_l represents linear 1st order scattering, $a_k x_n$ represents 1st order nonlinear scattering, r_1, r_2 , and r_3 are the reverberations of Class 1-3 of the linear scattering, and n_k represents noise that is uncorrelated in the slow time, for example through exchange of scatterers within the beam. We note that r_2 has the same variation with the nonlinear and Doppler delays as the 1st order linear scattering, and can hence not in general be descriminated from the 1st order scattering with the SURF method. However, one can obtain $r_1(t) = r_2(t)$ by selecting the same receive and transmit beams.

Today, reverberation suppression is achieved by second harmonic imaging. But this has the disadvantage of low penetration, and little or no signal in the near field. SURF pulses on the other hand images in the fundamental frequency, but has also the added effect of low signal level in the near field. This is due to the increasing nature of the nonlinear delay $\tau(\vec{r})$.

Chapter 8

Effects of reverberations and reverberation suppression in elastography images

All results presented in this chapter are made as a result of recordings made with a Sonix RP ultrasound device [43] by the Ultrasonix company (Ultrasonix Medical Corporation, Vancouver, Canada). The Sonix RP is an ultrasound research interface used in over 100 universities and institutions world-wide, and offers a wide variety of imaging possibilities and is a flexible research tool that can be used to capture raw data and generate new technologies. The elastography recordings were performed on a basic CIRS Model 049 elasticity phantom [2] as seen in Figure 4.1. The phantom model has an attenuation factor of 0.5 dB/MHz/cm and contains two sizes of spheres positioned at two different depths, The spheres in the phantom will appear isoechoic to the background using conventional B-mode imaging. All recordings were done on one of the smallest spheres located at a depth of around 15 mm from the phantom surface, and has an elasticity being harder than the tissue surrounding it. The recordings done on the SonixRP system are recorded without any form of filtering and are stored as RF values. Any filtering, demodulation and time-delay estimation is hence performed on the raw recorded RF data.

All simulations, calculations and images were created using Matlab version R2008a by the Mathworks company [36], unless otherwise stated.

8.1 Elastography recordings made with a 7.5 MHz Ultrasonix transducer

A data set recorded with the 7.5 MHz Ultrasonix probe was performed to demonstrate the feasibility of the phase-based time-delay estimation algorithm. Seen in Figure 8.1 is the frequency spectrum of the recorded RF data in blue, the filter used to filter the data in the dashed red line, and the filtered RF data in green. The filter used to filter the data is a bandpass Finite Impulse Response (FIR) filter with cut-off frequencies of 2.5 and 9 MHz.

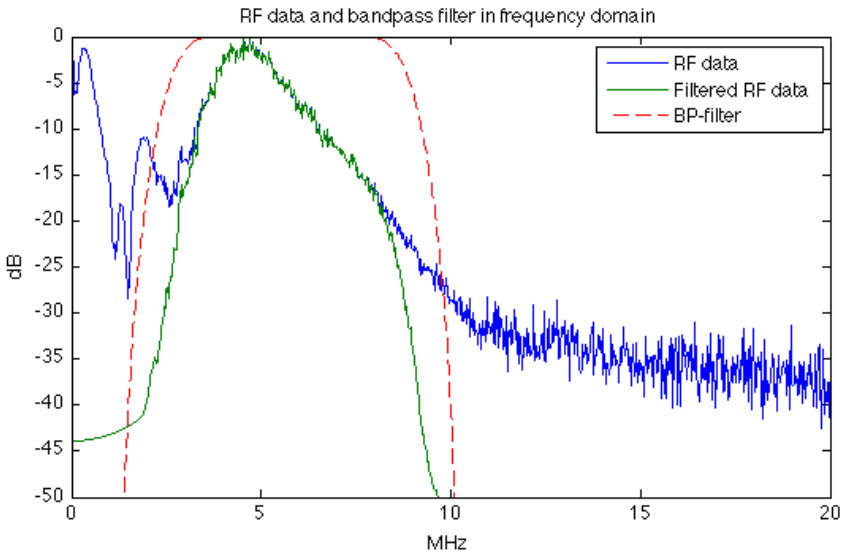

Figure 8.1: Frequency spectrum of RF data recorded with a 10 MHz Ultrasonix probe and a sampling frequency $f_s = 40$ MHz. FIR bandpass filter with cut-off frequencies of 2.5 and 9 MHz is plotted in red, and the filtered spectrum of the RF signal is plotted in green

Seen in the first frame of Figure 8.2 is the ordinary B-mode image as displayed on the scanner after filtering with a bandpass filter has been performed. Frames two and three display time delay and strain values as estimated by the phase-based time-delay estimation algorithm as described in Chapter 2. As seen the strain rate values will give the differences in elasticity, although the frame to a great extent is corrupted by noise. Finally, the last frame displays the final elastogram after thresholding and time and spatial domain smoothing has been performed as described in [35]. Comparing with the unprocessed strain values in the third frame, smoothing and thresholding of frames have a massive impact. As seen from the B-mode image in the first frame of the figure, one can catch a glimpse of the overall structure of the sphere, although it is quite hard to differ from the surroundings, and knowledge of the exact location of the sphere is prerequisite in order to be able to detect it.

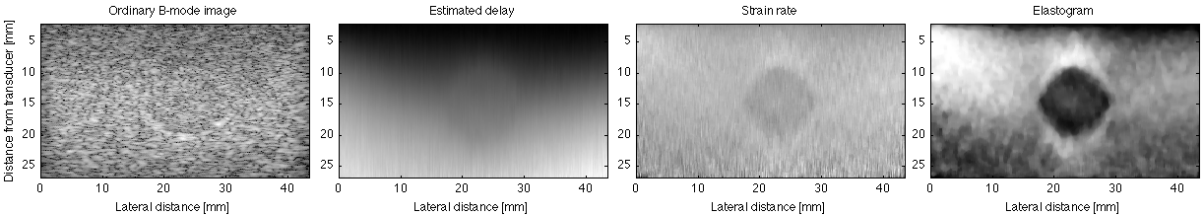

Figure 8.2: Ordinary B-mode image, estimated time delay values, strain rate values, and elastogram made with a 7.5 MHz Ultrasonix probe, a frame rate of 27 Hz and a demodulation frequency $f_d = 5$ MHz. Time delay values were estimated by a linear model of $\hat{\tau}$ within a window size of 4.1 mm

Seen in Figure 8.3 is an image of a single line running from the top to the bottom of a single frame. The top row is a line taken from the second frame of Figure 8.2, the second row is the same line taken from the third frame of Figure 8.2, and the bottom row is the same line taken from the elastogram displayed in the fourth frame of Figure 8.2. By comparing the unprocessed strain data on the second row with that of the final grayscale values which are displayed on the bottom row, the impact the time and spatial domain smoothing has on the final elastogram is

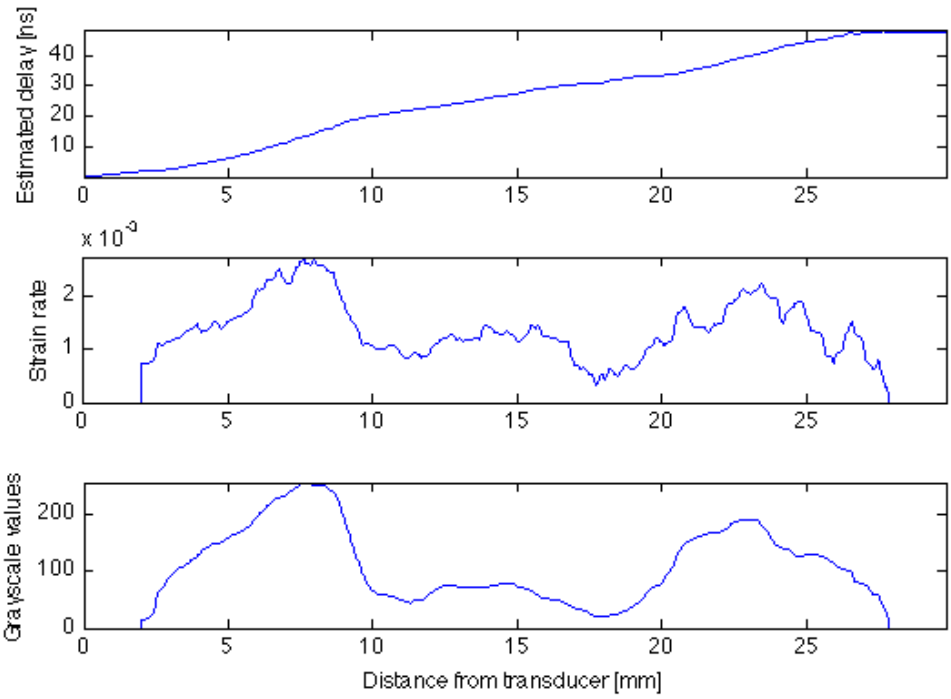

Figure 8.3: Estimated time delay values in nanoseconds, local rate of change, i.e. strain rate values, and final elastogram values for a single line running from top to bottom of a single frame as seen in the second, third an fourth frame of Figure 8.2

quite evident. Also interesting to notice is the value of both the strain data and elastogram values from a depth of around 10 mm to 20 mm. As a small gradient is a sign of stiff tissue, and a large gradient is sign of soft tissue, it is clear that the line goes straight through the inclusion seen clearly in the fourth frame of Figure 8.2. Also interesting to notice is the fact that the values at the start and end of the frame displaying the strain rate values, and the frame displaying the elastogram values, are equal to zero. This is due to the fact that a window of N number of samples is used to improve the estimate, and the delay is calculated over this window, which in turn gives that the estimated delay values will be set to zero over a range of $N/2$, or half the window length, at the start and end of the estimated delay. For this demodulation frequency the window size is 4.1 mm, and as seen from Figure 8.3, the start and end values for the middle and bottom row are equal to zero at half this sample size.

8.2 Elastography recordings made with 6.5 MHz SURF transducer "Viglen"

Now, turning attention to the SURF probe and imaging in ordinary B-mode, again it is possible to display the frequency content of the RF spectrum in blue, the frequency spectrum of the FIR bandpass filter in the dashed red line, and the frequency content of the filtered RF data in green as seen in Figure 8.4. Comparing with Figure 8.2 the cut-off frequencies of the FIR bandpass filter are the same. The frequency content of the RF values however are different, as the ultrasound probe used to record the data is different.

Seen in the first frame of Figure 8.2 is the ordinary B-mode image as displayed on the scanner

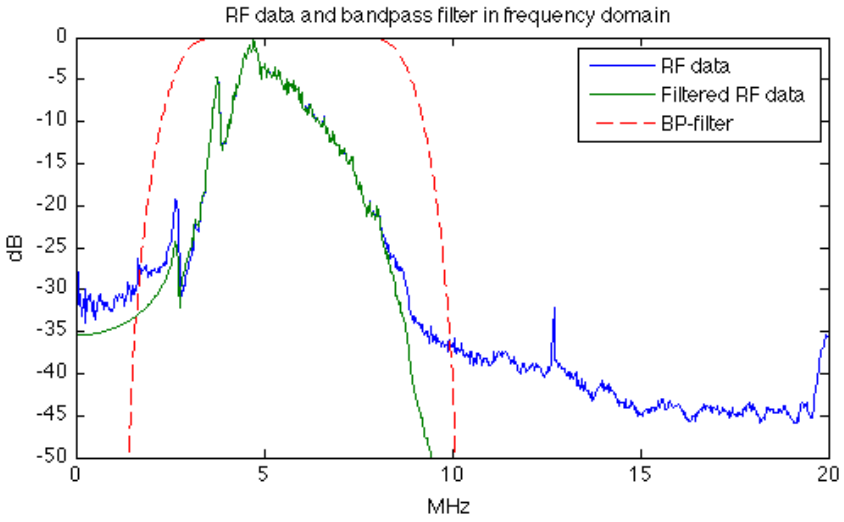

Figure 8.4: Frequency spectrum of RF data recorded with a 6.5 MHz SURF probe "Viglen" and a sampling frequency $f_s = 40$ MHz. FIR bandpass filter with cut-off frequencies of 3 and 9 MHz is plotted in red, and the filtered spectrum of the RF signal is plotted in green

after filtering with a bandpass filter has been performed. Frames two and three display time delay and strain values respectively, whereas frame four display the final elastogram. As this recording was demodulated with a demodulation frequency of 6 MHz, the window size for which the delay is calculated over is smaller than the case for the recording done with the Ultrasonix probe, and is equal to 3.4 mm. Comparing Figure 8.5 with Figure 8.2 there is clearly a difference. It seems that the recording done with the SURF probe is much more corrupted by noise, although all parameters involved in making the elastogram are equal as before, besides the window size which is smaller due to a change in demodulation frequency.

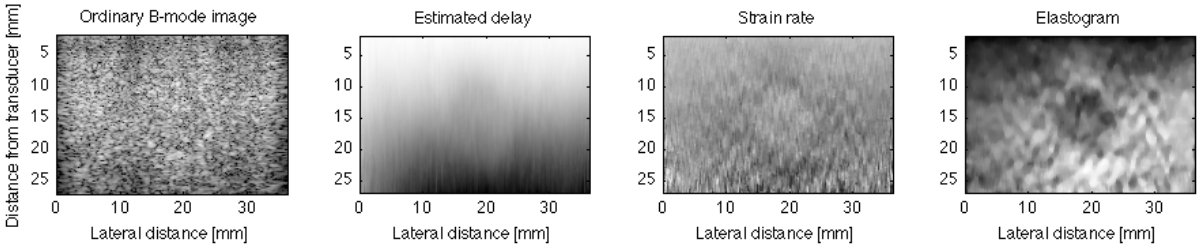

Figure 8.5: Ordinary B-mode image, estimated time delay values, strain rate values, and elastogram made with a 6,5 MHz SURF probe "Viglen", a frame rate of 26 Hz and a demodulation frequency $f_d = 6$ MHz. Time delay values were estimated by a linear model of $\hat{\tau}$ within a window size of 3.4 mm

Seen in Figure 8.6 is an image of a single line running from the top to the bottom of a single frame. The top row is a line taken from the estimated delay values seen in the second frame of Figure 8.5, the second row is the same line taken from the strain data seen in the third frame of Figure 8.5, and the bottom row is the same line taken from the elastogram displayed in the fourth frame of Figure 8.5. Comparing the figure with Figure 8.3 it is clear that the signal displayed in Figure 8.6 is more influenced by noise as opposed to the case displayed in Figure 8.3. Especially the estimates of the strain before any form of smoothing or thresholding is performed as seen in the center row of Figure 8.6 are to an extent more noisy than what is the case for the values

seen in the middle row of Figure 8.3. This may again indicate that the feasibility of obtaining high quality RF data, which in turn is processed by the phase-based time-delay estimator, may be somewhat diminished when using the SURF probe.

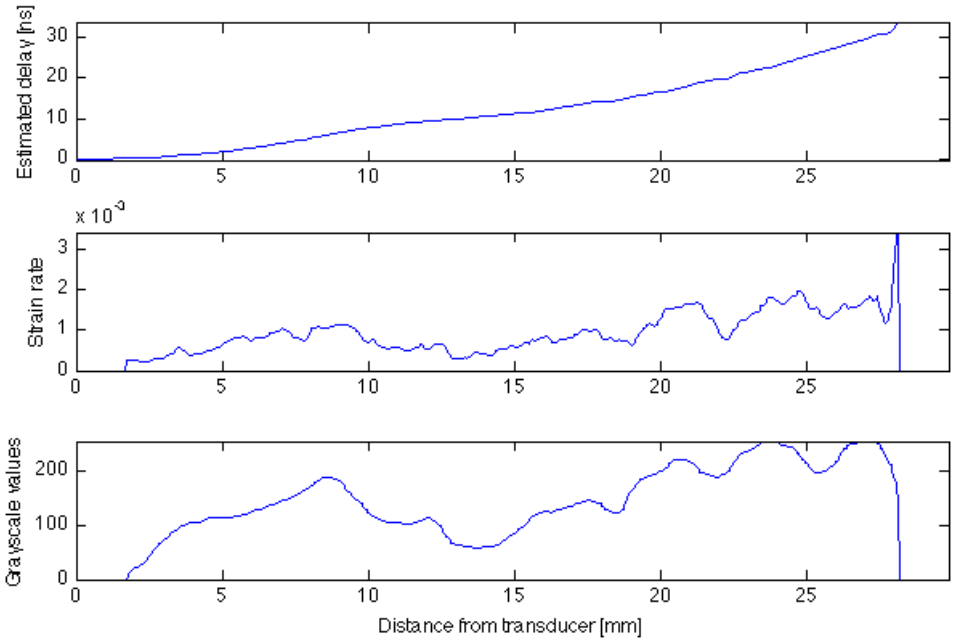

Figure 8.6: Estimated time delay values in nanoseconds, local rate of change, i.e. strain rate values, and final elastogram values for a single line running from top to bottom of a single frame as seen in the second, third an fourth frame of Figure 8.5

8.3 Elastography recordings made with 6.5 MHz SURF transducer "Viglen" with reverberation suppression

As discussed in Chapter 5 a SURF pulse complex is composed of both a LF manipulation pulse, and a HF imaging pulse. The purpose of the LF pulse is to manipulate the scattering and propagation of the HF imaging pulse, and the HF pulse is then used to image tissue or nonlinear scatterers under the influence of the manipulations pulse. As seen from the frequency content of the unfiltered RF data plotted in blue in Figure 8.7, there exist a large LF peak around 1.9 MHz. This LF content is removed by filtering, and the LF pulse is then only transmitted and not received. Comparing with the frequency spectrum when imaging without a dual pulse SURF setting as seen in Figure 8.4 the difference is quite clear. Not only is there an introduction of the LF content, but the HF spectrum is altered as well.

Seen in the first frame of Figure 8.8 is the ordinary B-mode image as displayed on the scanner after filtering with a bandpass filter with cut-off frequencies of 3 MHz and 9 MHz has been performed. Frames two and three display estimated time delay and strain values as estimated by the phase-based time-delay estimation algorithm, whereas frame four display the final elastogram after thresholding and smoothing to suppress noise. As this recording was demodulated with a demodulation frequency of 6 MHz, the window size for which the delay is calculated over is set to 3.4 mm. Comparing Figure 8.5 with Figure 8.8 there is not much difference, although the quality of the final elastogram is clearly diminished as opposed to the recording done with the

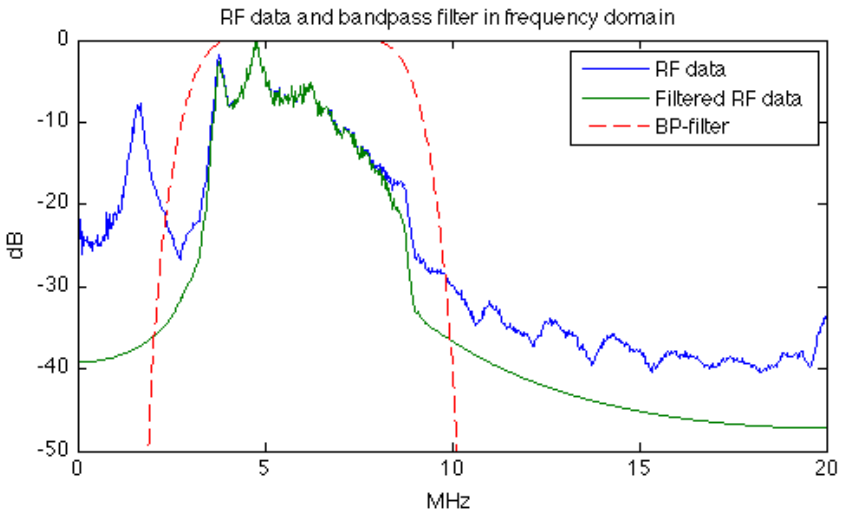

Figure 8.7: Frequency spectrum of RF data recorded with a 6.5 MHz SURF probe "Viglen" and a sampling frequency $f_s = 40$ MHz. FIR bandpass filter with cut-off frequencies of 3 and 9 MHz is plotted in red, and the filtered spectrum of the RF signal is plotted in green

Ultrasonix probe seen in the fourth frame of Figure 8.2. Nevertheless, this results proves that it is possible to combine the phase-based time-delay estimation algorithm, and the SURF imaging reverberation suppression technique, to produce elastography images.

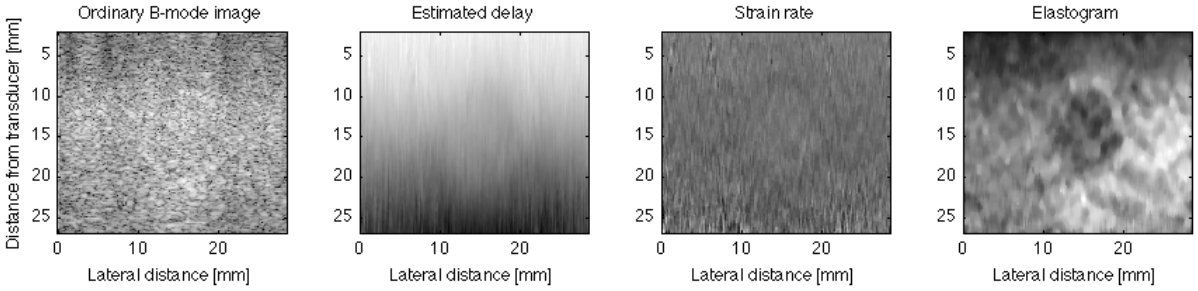

Figure 8.8: Ordinary B-mode image, estimated time delay values, strain rate values, and elastogram made with a 6.5 MHz SURF probe "Viglen", a frame rate of 26 Hz and a demodulation frequency $f_d = 6$ MHz. Time delay values were estimated by a linear model of $\hat{\tau}$ within a window size of 3.4 mm

8.4 Introducing reverberations in the signal, and the effect of reverberation suppression for B-mode and elastography images

To validate the correctness of the reverberations when applying a reverberation model, and ensuring the reverberations lie on top of, and not above or beneath the inclusion, a recording made with the 6.5 MHz SURF probe "Viglen" was made on the CIRS model 050 near field phantom. The reverberation model to be applied on top of the phantom is an approximately 1 cm thick soft silicon plate, and the reverberations will occur at twice this thickness, i.e. approximately 2 cm from the transducer surface. Figure 8.9 displays two screenshots taken from the Ultrasonix scanner. Seen on the left hand side of figure is the ordinary B-mode imaging situation, and on the right hand side is the same situation when SURF reverberation suppression is utilized.

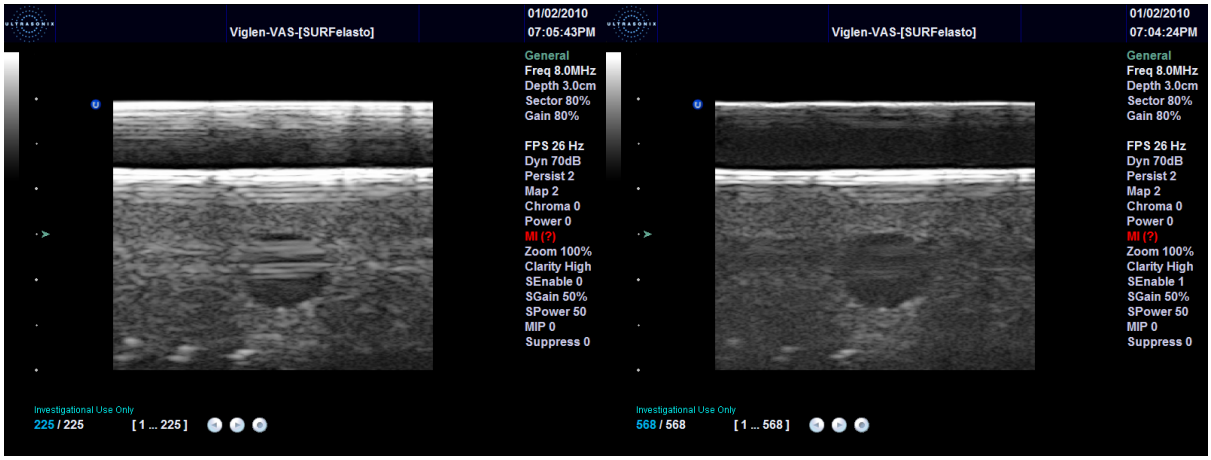

Figure 8.9: B-mode image of CIRS model 050 near field phantom [5] with reverberation model applied. Ordinary B-mode image on the left hand side, and reverberation suppression processed image on the right hand side

As seen from the figure the CIRS model 050 near field phantom gives an instant and quantifiable assessment on the impact of both the introduction of reverberations, and the effectiveness of the SURF reverberations suppression technique. As the sphere in the middle of both frames is a cyst with approximately a 10 dB difference in backscattering properties in respect to the surrounding tissue, it is quite easy to spot both its location and the impact of reverberations. This is opposed to the CIRS model 049 elasticity phantom where the sphere is virtually indistinguishable from the surrounding tissue, as the difference lies in the elasticity and not the backscattering properties. As seen from the frame on the right hand side of Figure 8.9, the reverberation suppression technique is able to reduce the reverberations to such an extent that they have almost disappeared. The unfortunate effect is that much of the signal power is suppressed as well, and there is less penetration at the depths where the sphere is located. This loss of signal power will then have an impact on the resulting SNR of the signal in that area, and lead to a decreased quality of the recording, and hence the obtained RF values. As discussed in Section 7.2 the reverberation suppression technique of SURF imaging should be tailored in order to make the gain factor as high as possible within the imaging area, and the maximum and minimum absolute values of this gain factor are 2 for $\omega\tau = \pi$ and 0 for $\omega\tau = 0$. As this expression depends on the achieved delay between the two shots fired to compose the synthetic SURF pulse, it is

likely that for this situation this delay is not high enough in order to maximize the gain factor, which in turn results in a decrease in signal strength.

Now, turning attention back to the CIRS model 049 elasticity phantom, and applying the reverberation model, it is possible to examine the frequency spectrum of both the obtained RF values, the filtered data, and the FIR bandpass filter plotted in blue, green and red respectively as seen in Figure 8.10. Once again it is clear how the LF pulse is filtered out by the FIR bandpass filter, and is then only transmitted and not received.

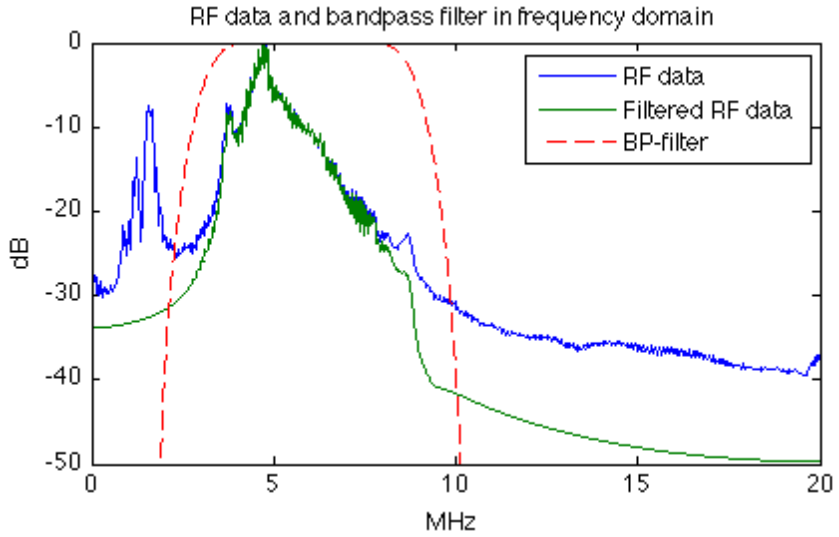

Figure 8.10: Frequency spectrum of RF data recorded with a 6.5 MHz SURF probe "Viglen" and a sampling frequency $f_s = 40$ MHz. FIR bandpass filter with cut-off frequencies of 3 and 9 MHz is plotted in red, and the filtered spectrum of the RF signal is plotted in green. Recording made with reverberation model applied to the phantom

Converting the filtered and demodulated RF-data into estimated time-delay values by the phase-based time-delay estimation algorithm, it is possible to examine the result as seen in Figure 8.11. The recording was done with a frame rate of 26 Hz, and the time-delays were estimated by a linear model within a window length of 3.4 mm.

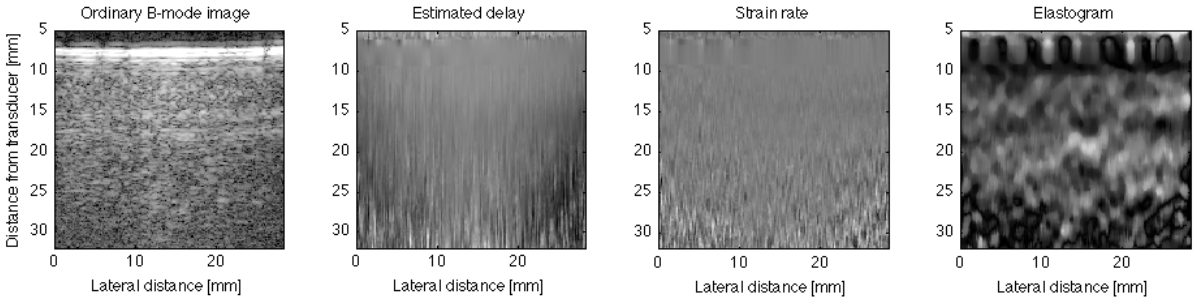

Figure 8.11: Ordinary B-mode image, estimated time delay values, strain rate values, and elastogram made with a 6.5 MHz SURF probe "Viglen", a frame rate of 26 Hz and a demodulation frequency $f_d = 6$ MHz. Time delay values were estimated by a linear model of $\hat{\tau}$ within a window size of 3.4 mm. Recording done with both reverberation model and reverberation suppression

Judging from Figure 8.11 alone, it is difficult to make any general remarks. The inclusion present in the phantom is not visible neither in the B-mode image, or from the estimated time-delay,

strain values, and final elastogram. As seen in Section 8.2 and Section 8.3, the feasibility of the SURF probe "Viglen" to obtain high quality RF data is diminished compared to the Ultrasonix probe. This may suggest that an added reverberation layer will further decrease the quality of the RF signals obtained, as the SNR is further lowered. In addition as seen from Figure 8.9 an additional loss of signal power occurs when the time delay between two SURF pulse complexes is not high enough to be able to generate a maximum value of the gain factor. This again will have an impact on the RF data. Finally, and most importantly, the reverberation model which is used is not optimal. As the main goal of adding a reverberation model to the phantom is to mimic real life situations, and specifically the three different types of reverberations as discussed in Section 6.2, the need for a correct and improved model is apparent. It is likely that all these three factors concerning the SURF probe, loss of signal power when using reverberation suppression, and the reverberation model that is used combined have a negative impact on the quality of the obtained RF data, and hence the correctness of the estimated time delays and the final elastogram.

In order to ensure that the reverberations added to the signal are on top of the inclusion, and that the reverberation model does not ensure a severe loss of signal power of the propagating ultrasound wave, a different approach is to use a SURF recording as that in Section 8.3, and add the reverberations to the signal directly in Matlab after the recording has been done. Seen in Figure 8.12 is a recording done on the CIRS model 050 near field phantom with reverberations applied after the recording has been obtained, in order to easily quantify and adjust the position of the reverberations. The recording was done with the SURF probe "Viglen" with reverberation suppression, such that the frame on the right hand side of the figure represents the situation with reverberations and reverberation suppression.

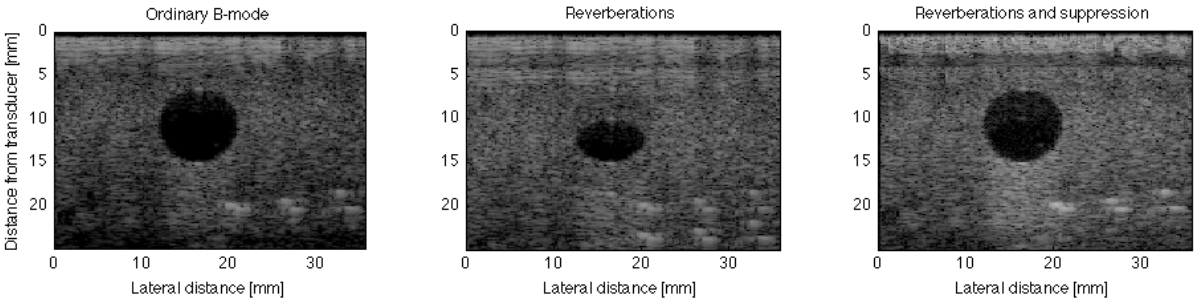

Figure 8.12: Ordinary B-mode image, image with simulated reverberations, image with simulated reverberations and reverberation suppression.

As seen from the second frame of the figure, the reverberations are simulated as replicas of the signal over a certain depth, and the simulated reverberations occur at twice this depth. Comparing the third frame of Figure 8.12 with the second frame of Figure 8.9, it is clear that reverberation suppression is achieved in this situation as well, but without the heavy loss of signal power lost by imaging through an initial reverberation model layer.

Now turning attention to the same recording as described in Section 8.3, we are able to add reverberations to the signal without the undesired effect of loosing signal power further down the propagating path. As the recording is performed on the CIRS 040 elastography phantom, it is also possible to convert the recordings into estimated time delays, and hence also into elastography images. Seen in Figure 8.13 is the same recording as described in Section 8.3, i.e. a SURF recording with reverberation suppression, only in this case reverberations are added in Matlab before any time delays are estimated. The top row of the figure displays the B-mode

images as seen on the ultrasound scanner, whereas the bottom row displays the corresponding elastogram as estimated by the phase-based time-delay estimation algorithm. Most interesting is the second and third frame of the figure, i.e. the frame where reverberations are added, and the frame where the recording with added reverberations are processed with SURF reverberation suppression. Inspecting the second elastogram with added reverberations, it is clear how the phase-based algorithm completely fails to estimate any differences in strain, as the inclusion is corrupted by noise. The frame processed with SURF reverberation suppression however is able to remove the reverberations appearing on top of the inclusion, and the difference in strain is once again detectable. Although the images displayed are taken from one frame only, the conclusions are generally valid.

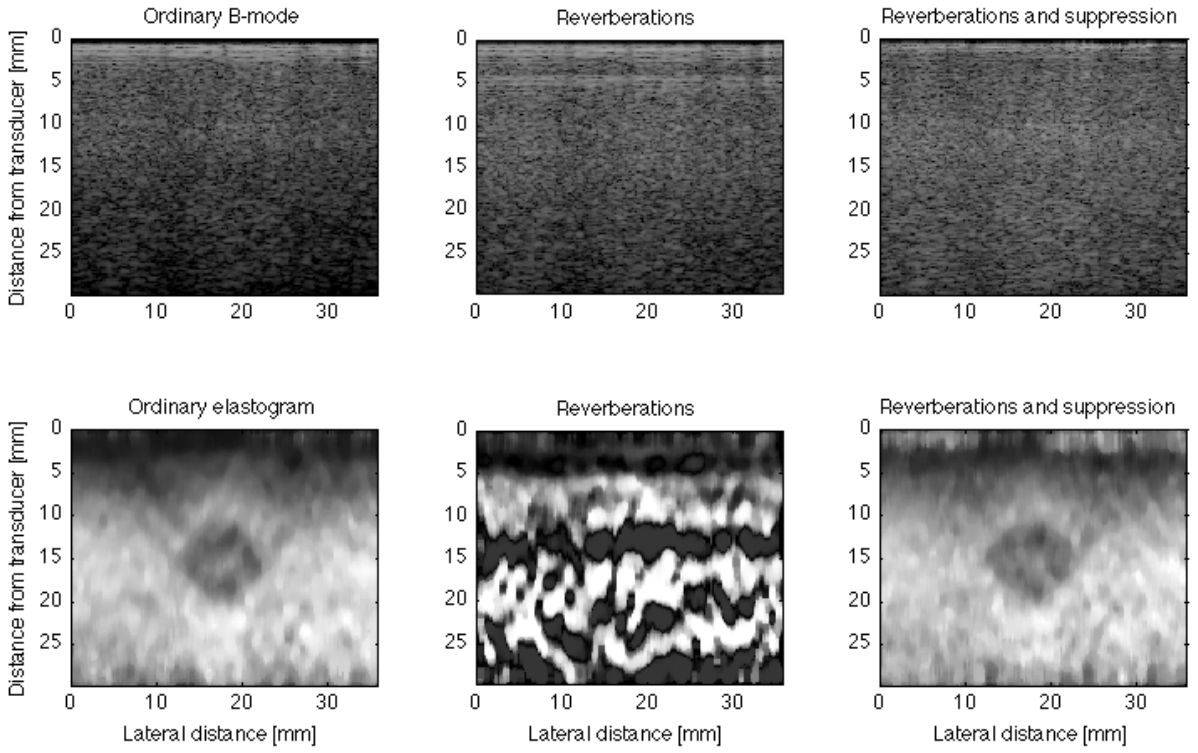

Figure 8.13: Ordinary B-mode image and corresponding elastogram, same frame with simulated reverberations and elastogram with reverberations, and same frame with simulated reverberations and reverberation suppression and corresponding elastogram. Recorded with a 6.5 MHz SURF probe "Viglen". FIR bandpass filtered with cut-off frequencies of 3 and 9 MHz. Frame rate 26 Hz, and demodulation frequency $f_d = 6$ MHz. Time delay values were estimated by a linear model of $\hat{\tau}$ within a window size of 3.4 mm

8.5 Elastography images computed from in vivo recordings of the lower arm

A recording has been done transversally on the lower arm to prove the feasibility of the phase-based time-delay estimation algorithm for in vivo situations. The recording was done with the 6.5 MHz Ultrasonix transducer as described in Section 8.1, and filtered with a FIR bandpass filter with cut off frequencies of 3 MHz and 9 MHz. The data set was demodulated with a demodulation frequency $f_d = 6$ MHz, which in turn gives a window size of 3.4 mm for which the delay values are calculated over with a linear model of $\hat{\tau}$. As seen from the left frame of Figure 8.14, the estimated strain values are overlaid the ordinary B-mode image with an opacity of 25%, which enables us to see both the structure and the elasticity of the tissue of interest. Comparing the left and right frame of the figure, it is clear how elasticity can not be judged based on the ordinary B-mode image alone. The structure going from the top right corner of the left frame of the figure and across the center of the frame is for instance not visible at all on the B-mode image. It is likely that this is a muscle fiber of some sort, having elastic properties being harder than the connective tissue surrounding it.

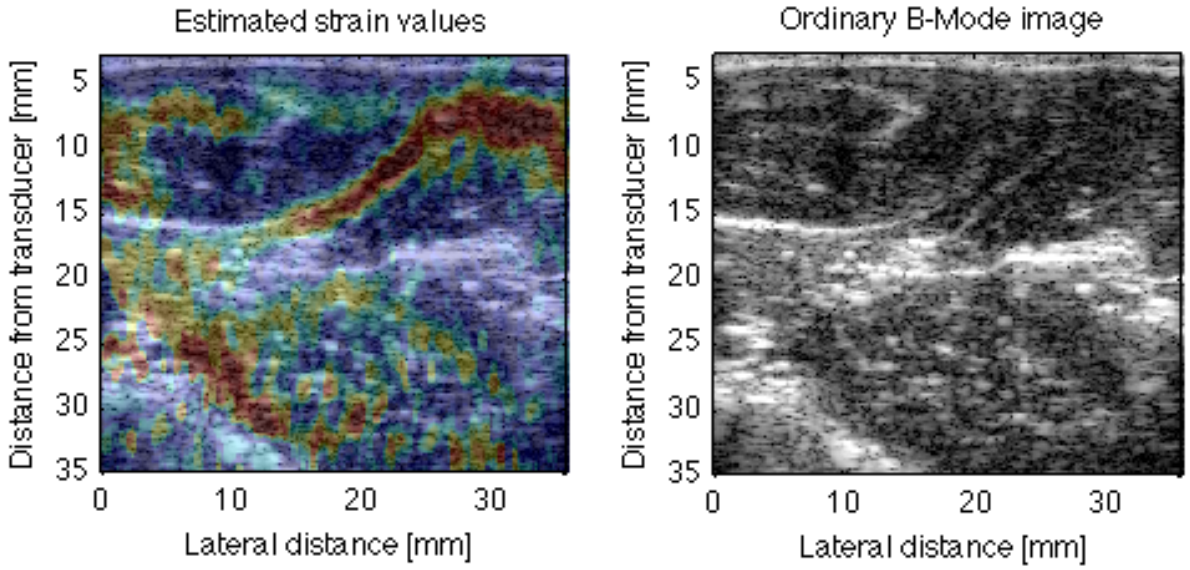

Figure 8.14: Transversal recording on the lower arm with estimated strain values on the left hand side, and the ordinary B-mode image on the right hand side. Recording made with a 7.5 MHz Ultrasonix transducer, and filtered by a FIR bandpass filter with cut off frequencies of 3 MHz and 9 MHz. Data demodulated with a demodulation frequency $f_d = 6$ MHz. Time delay values were estimated by a linear model of $\hat{\tau}$ within a window size of 3.4 mm

Chapter 9

Discussion

An iterative scheme to update the values of the instantaneous frequency estimates, and the estimated time-delay values has been implemented for the phase-based time-delay estimation algorithm. Although conclusions regarding the statistical properties of such a scheme has been made, only general observations have been made when lowering the sampling frequency. The observations suggest how an iterative scheme may be an important tool for lowering the standard deviation when the sampling frequency is low, but no general conclusion relating the three parameters bandwidth, sampling frequency and number of iterations have been made.

When estimating time delays the delay is calculated over a window of N number of samples to improve the estimate, and the length of this window will have an impact on the final elastogram. A too short sample volume will lead to too close tracking of the noise in the image, whereas a too long sample volume will lead to too much smoothing of the final image. The optimal value is found to be with a window length of approximately 13 wavelengths. The question remains however if this is a valid assumption. As the value is found experimentally, the hypothesis should be tested on several different data-sets as well. Also trying to relate this window size with one or more quantifiable factors regarding the quality of the final elastogram could even further lead to a globally valid value..

Two models, one linear and one polynomial, have been tested for the phase-based time-delay estimation algorithm as parametric models of the local delay variation. However, it is not a given fact that either of these are the best fit to real life situations, and other parametric models should be tested out as well. The main drawback of using a more complex model however, is the increased computational time. The observations and conclusions drawn from the experiments regarding the two parametric models have mainly been conducted on one specific data-set. It would also be interesting to see if the observations and conclusions given in this paper are universally valid when testing the different models on several other data-sets as well.

Performing in vitro recordings with a reverberation model proved difficult. The 6.5 MHz SURF transducer "Viglen" is not yet optimal compared to an ordinary transducer, and the recorded RF-data is also diminished, which in turn suggests a lowered SNR. Also the reverberation suppression technique implemented as to date not only suppresses reverberations, but also results in a decreased SNR. The reverberation suppression technique of SURF imaging should be tailored in order to make the gain factor as high as possible within the imaging area, and the maximum and minimum absolute values of this gain factor are 2 for $\omega\tau = \pi$ and 0 for $\omega\tau = 0$. As this expression depends on the achieved delay between the two shots fired to compose the synthetic SURF pulse, it is likely that for the reverberation situation in this thesis this delay was not high enough in

order to maximize the gain factor, which in turn resulted in a decrease in signal strength. Also, for the SURF mode with reverberation suppression the most basic setting was used, i.e. the synthetic SURF beam with reverberation suppression consists of the difference between a HF pulse transmitted in a compression phase of the LF pulse, and a HF pulse transmitted in a rarefaction phase of the LF pulse. Although this approach works, different settings may be tried as well, and may prove to further increase the reverberation suppression capabilities and the final quality of the obtained ultrasound image.

More importantly, the reverberation model that was used was not optimal, and was not able to reproduce reverberations adequately. Much of the signal strength was lost when having to pass through this initial layer of reverberation model, and a great challenge is in keeping the SNR high while at the same time producing reverberations. Also the reverberation model should be able to mimic a real life situation as close as possible, in addition to achieve the three different kinds of reverberations which are present.

Chapter 10

Conclusion

The phase-based time-delay estimation algorithm works very well for estimating delays. As the algorithm uses approximations to the phase difference and the instantaneous frequency to calculate the delay, these approximations will also have an impact on the correctness of the delay estimates. The assumption that the modulating phase is equal for both the approximations is somewhat inaccurate, as there indeed does exist differences of the modulating phase when comparing the instantaneous frequency and the phase difference. However, this difference can be minimized by using the estimated delay to obtain updated values for the instantaneous frequency. These updated values may again be used to find new improved values for the delay estimate in an iterative fashion. By implementing an iterative scheme it is possible to lower the standard deviation significantly, although on the cost of an increased bias. An interesting feature is the situation when the sampling frequency is low, or even beneath the Nyquist rate. In such a situation an iterative scheme may help to calculate delays up to a larger delay value than what is the case for the ordinary method. This may indicate that the iterative scheme may be an important tool when the acquired signal is corrupted by noise.

As the estimation of tissue stiffness is basically a time-delay estimation problem when it comes to elastography, the phase-based time-delay estimation algorithm may also be used for elastography purposes which is proved both in vitro and in vivo. As the delay is calculated over a window of N number of samples to improve the estimate, the length of this window will have an impact on the final elastogram. A too short sample volume will lead to too close tracking of the noise in the image, whereas a too long sample volume will lead to too much smoothing of the final image. There is hence a tradeoff between contrast and resolution, and the optimal situation is found to be with a window length of approximately 13 wavelengths.

The phase-based time-delay estimation algorithm makes no assumption on the local delay variation, and any parametric model can be used for the local delay variation within the sample volume of size N. By comparing a linear and a polynomial model as parametric models, and improvement in the image quality of the elastography images is observed when using a polynomial model of the second degree. As a polynomial model has a higher complexity than a linear, it is better in detecting edges and differences located at a depth where the strain is lower than closer to the transducer surface, which in turn improves the resolution of the elastogram. In addition, an improvement of the dynamic area of the image when using a polynomial model is observed, implying and improvement also in contrast. These differences may be further emphasized when performing spatial filtering with a median filter. Although a polynomial model is superior to a linear as parametric model of the local delay variations, it comes at a cost of

increased computational time which is on average 50% longer.

RF-data recorded with the 6.5 MHz prototype SURF probe "Viglen", which in turn are converted to elastography images, indicate that the probe is not yet optimal as opposed to an ordinary 7.5 MHz Ultrasonix probe. Especially the estimated strain data before any thresholding or smoothing has been performed are to an extent much more corrupted by noise than what is the case for strain values estimated from RF-data recorded with the Ultrasonix probe. This may indicate that the feasibility of obtaining high quality RF data is somewhat diminished when imaging with the SURF probe "Viglen".

Reverberations impair the contrast resolution of ultrasound images, and greatly reduces the validity of the estimated time delays. When these reverberations appear on top of an inclusion, the estimated elastography images are unable to distinguish differences in elasticity, and no inclusion is visible in the final elastogram. The SURF reverberation suppression technique is able to reduce reverberations, and have an impact on the final image quality when the image is corrupted by reverberating noise. Elastography images with computer simulated reverberations display a markedly improved elasticity estimate when the SURF reverberation suppression technique is used. Estimating time-delays on a signal with reverberations, the phase-based time-delay algorithm was unable to distinguish any differences in elasticity at all. Estimating time delays on a signal with reverberations and SURF reverberation suppression however, the algorithm was able to clearly estimate differences in strain, and display the presence of an inclusion.

Chapter 11

Further work

As elastic tissue not only experiences compression in the range direction, but in all directions simultaneously, the estimation and imaging of tissue strains is by definition a three dimensional problem. Estimating displacement in lateral and axial directions besides just range may greatly improve the estimates and should be further investigated. The main obstacle will be in keeping the computation time fast enough for the implementation to be done in real time.

Further studies of the effect of reverberations on the estimated elastography images should be conducted. A great challenge is in not loosing too much signal power when imaging through a reverberation model. Emphasis should be put on creating a suitable reverberation model which does not attenuate the signal too much, but also mimics the real life situations as close as possible, in addition to achieving the three kinds of reverberations which are present.

The technique of which the compression is applied greatly affects the quality of the elastography images. By implementing the phase-based timed-delay algorithm on an ultrasound scanner one is able to get real time feedback and hence adjust the compression technique accordingly.

By having the phase-based elastography algorithm implemented on an ultrasound scanner, the next step will be in conducting in vivo experiments and clinical studies. This purpose will most likely give rise to new challenges not easily detected from simulations or when performing in vitro experiments in the laboratory.

Appendix A

Matlab code for phase-based time-delay estimator

```
function [tau, dtau] = phase_based_time_delay_estimation(iqdata,fs_iq,fdemod,method,iterations)
% function [tau, dtau] = phase_based_time_delay_estimation(iqdata,fs_iq,fc,fdemod,method,iteratio
%
% Estimates phase delays between corresponding columns of the two complex images
% contained in iqdata. This function finds either a 'running line' estimate, or a
% polynomial estimate of the delay for each time sample using a weighted least
% mean squares method within a window of 13.2 wavelengths. The estimator
% uses the phase difference and the instantaneous frequency to estimate the
% delay. An updated value for the instantaneous frequency can be found
% through an iterative scheme.
%
% Inputs
%  iqdata       3D-array of two complex images
%  fs_iq        sampling frequency fast time
%  fdemod       demodulation frequency in fast time
%  method       'lin' for linear model, 'poly' for polynomial model
%  iterations   number of iterations for iterative scheme
%
% Outputs
%  tau          matrix of estimated phase delays
%  dtau         matrix of estimated delay slopes (strain data)


%Setting variables
if nargin < 5
    iterations = 1;
end
if nargin < 4
    method = 'lin';
end
[samples, lines, frames] = size(iqdata);
t_interp = (0:samples-1)';
c = 1540;

%Fixed nr of wavelengths for window size
win_length_lambda = 13.2;
win_length_m = win_length_lambda*c/fdemod;
win_length_samples = floor(win_length_m*2*fs_iq/c);
```

```
39
40 %Make sure number of samples for window length is odd
41 win_length_samples = win_length_samples + 1 - mod(win_length_samples,2);
42
43 %Buffering for speed
44 frames = frames-1;
45 tau = zeros(samples,lines,frames,iterations);
46 dtau = zeros(samples,lines,frames,iterations);
47
48 for frame = 1:frames
49
50     %Using two consecutive frames for calculating the delay
51     iq1 = iqdata(:,:,frame);
52     iq2 = iqdata(:,:,frame+1);
53
54     %Compute phase difference psi
55     psi = angle(iq1.*conj(iq2));
56
57     %Compute weight
58     w = abs(iq1.*conj(iq2));
59
60     %Compute instantaneous frequency theta
61     fdemod_phase = fdemod/fs_iq;
62     theta = zeros(samples,lines);
63     theta(2:end-1,:) = 0.25*sum(angle(iqdata(3:end,:,[frame, frame+1])...
64         .*conj(iqdata(1:end-2,:,[frame, frame+1]))),3) + 2*pi*fdemod_phase;
65     theta(1,:)=theta(2,:); theta(end,:)=theta(end-1,:);
66
67     %Half window length
68     win_h = (win_length_samples-1)/2;
69
70     %Window centered around zero
71     n = (-win_h:win_h)';
72
73     %Linear model for the delay
74     if strcmp(method,'lin')
75
76         for line = 1:lines
77
78             theta_new = theta(:,line);
79
80             for iteration = 1:iterations
81
82                 for k = (win_h+1):(samples-win_h)
83
84                     ix = k+n;
85
86                     Theta(:,2) = n.*theta_new(ix);
87                     Theta(:,1) = theta_new(ix);
88
89                     Psi = psi(ix,line);
90                     W = diag(w(ix,line));
91
92                     %Weighted least squares estimate with linear model
93                     beta = inv(Theta'*W*Theta)*Theta'*W*Psi;
94
95                     tau(k,line,frame,iteration) = beta(1);
96                     dtau(k,line,frame,iteration) = beta(2);
97
98                 end
```

```
99
100                 %Assume small or zero delay at the start, interpolate ax+b = (tau_s/win_h)*k
101                 tau(1,line,frame,iteration) = 0.001;
102                 tau(2:win_h,line,frame,iteration) = tau(win_h+1,line,frame,iteration)...
103                     *(2:win_h)/(win_h-1);
104
105                 %Assume last values equal last known value
106                 tau(samples-win_h:samples,line,frame,iteration) = ...
107                     tau(samples-win_h-1,line,frame,iteration);
108
109                 %Update theta values with estimated delay, use an offset of one delay
110                 offset = tau(:,line,frame,iteration);
111                 xi1 = interp1(t_interp,iq1(:,line),t_interp-offset);
112                 yi1 = interp1(t_interp,iq2(:,line),t_interp+offset);
113                 theta_new = ((angle(iq1(:,line).*conj(xi1))+angle(yi1.*conj(iq2(:,line))))...
114                     ./(2*offset))+2*pi*fdemod_phase;
115
116                 %If theta values are non-existent, use old values
117                 theta_new(isnan(theta_new)) = theta(isnan(theta_new),line);
118
119             end
120         end
121
122     %Polynomial model for the delay
123     elseif strcmp(method,'poly')
124
125         order = 2;
126         A = repmat(n,1,order+1).^repmat(0:order,length(n),1);
127
128         for beam=1:lines
129
130             theta_new = theta(:,beam);
131
132             for iteration = 1:iterations
133
134                 for ii=(win_h+1):(samples-win_h)
135                     ix = ii + n;
136
137                     theta_z = theta_new(ix);
138
139                     psi_z = psi(ix,beam);
140                     w_z = w(ix,beam);
141
142                     Theta = A.*repmat(theta_z,1,order+1);
143                     D = diag(w_z);
144
145                     %Weighted least squares estimate with polynomial model
146                     B = Theta'*D*Theta;
147                     y = Theta'*D*psi_z;
148
149                     alpha = B\y;
150
151                     tau(ii,beam,frame,iteration) = alpha(1);
152                     dtau(ii,beam,frame,iteration) = alpha(2);
153                 end
154
155                 %Assume small or zero delay at the start, interpolate ax+b = (tau_s/win_h)*k
156                 tau(1,beam,frame,iteration) = 0.001;
157                 tau(2:win_h,beam,frame,iteration) = tau(win_h+1,beam,frame,iteration)...
158                     *(2:win_h)/(win_h-1);
```

```
159
160                 %Assume last values equal last known value
161                 tau(samples-win_h:samples,beam,frame,iteration) = ...
162                     tau(samples-win_h-1,beam,frame,iteration);
163
164                 %Update theta values with estimated delay, use an offset of one delay
165                 offset = tau(:,beam,frame,iteration);
166                 xi1 = interp1(t_interp,iq1(:,beam),t_interp-offset);
167                 yi1 = interp1(t_interp,iq2(:,beam),t_interp+offset);
168                 theta_new = ((angle(iq1(:,beam).*conj(xi1))+angle(yi1.*conj(iq2(:,beam))))...
169                     ./(2*offset))+2*pi*fdemod_phase;
170
171                 %If theta values are non-existent, use old values
172                 theta_new(isnan(theta_new)) = theta(isnan(theta_new),beam);
173
174             end
175         end
176     end
177 end
```

Appendix B

Matlab code for making elastogram

```
function [elastodata, alfa] = make_elastography(dtau,threshold,nframes,smoothweight,kernel,order)
% function [elastodata, alfa] = make_elastography(dtau,threshold,nframes,smoothweight,kernel,orde
%
% Computes thresholded and smoothed outputs of the strain data which gives
% an elastogram. Thresholding is done on individual frames to maximize the
% dynamic area of each frame. Smoothing is performed both in the time and
% the spatial domain to suppress noise.
%
% Inputs
%  dtau:          3D matrix of strain values
%  threshold:     1x2 matrix of initial threshold values
%  nframes:       Number of frames for time domain smoothing
%  weight:        Weight of frames for time domain smoothing, gauss or average
%  kernel:        Mask for spatial smoothing, uniform, gauss or median
%  order:         Size of the kernel matrix
%
% Outputs
%  elastodata:    3D matrix of elastography data
%  alfa:          Threshold values for individual frames


if nargin < 6
    order = 5;
end

if nargin < 5
    kernel = 'median';
end

if nargin < 4
    smoothweight = 'average';
end

if nargin < 3
    nframes = 5;
end

if nargin < 2
    threshold = [-5e-3 5e-3];
end

```

```
elastodata = dtau;
[samples,lines,frames,iterations] = size(elastodata);

%Change the dynamic area of the data by thresholding values
min_threshold = threshold(1);
max_threshold = threshold(2);

%Initially threshold entire dataset before individual thresholding of frames
elastodata(elastodata > max_threshold) = max_threshold;
elastodata(elastodata < min_threshold) = min_threshold;


%Number of bars for computing individual histogram
bars = 400;

%Alpha-low and alpha-high for each frame is saved in variable alfa
alfa = zeros(frames,iterations,2);

%Individual thresholding of frames
for frame = 1:frames

    for iteration = 1:iterations

        frame1 = elastodata(:,:,frame,iteration);

        %Calculate histogram of individual frames
        [N x_out] = hist(frame1(:),bars);
        N(N==max(N)) = max_threshold;

        %Computing new histogram leaving out already thresholded values
        N = N(2:end-1);x_out=x_out(2:end-1);

        %Find max value and standard deviation
        maxVal = max(N);
        stdVal = std(N);

        %Define threshold value as max value plus/minus 3*standard deviation
        tVal = maxVal-3*stdVal;

        %Find all values above threshold value
        aboveThreshold = find(N>tVal);

        %Define alfaLow and alfaHigh
        alfaLow = x_out(aboveThreshold(1));
        alfaHigh = x_out(aboveThreshold(end));

        %Threshold values that are above or below alpha values
        frame1(frame1 < alfaLow) = alfaLow;
        frame1(frame1 > alfaHigh) = alfaHigh;

        %Replace original frame with thresholded frame
        elastodata(:,:,frame,iteration) = frame1;

        %Save alpha values
        alfa(frame,iteration,:) = [alfaLow alfaHigh];

    end
end

%Computing filter mask
```

```
if strcmp(kernel,'gauss')
    zfactor = round(samples/lines);
    mask = gausswin(order*zfactor)*gausswin(order)';
    mask = mask/sum(mask(:));

elseif strcmp(kernel,'uniform')
    zfactor = round(samples/lines);
    mask = ones(order*zfactor,1)*ones(1,order);
    mask =  mask/sum(mask(:));

elseif strcmp(kernel,'median')
    zfactor = round(samples/lines);
    medsize = [order*zfactor order];

else
    error('Use gauss, uniform or median for kernel')
end

%Compute middle value of number of frames
middleVal = floor(nframes/2);

%Make time-smoothing statement to be executed based on numFramesSmooth
timeSmooth = 'img = ';
for l=1:nframes
    timeSmooth = [timeSmooth 'weight(' num2str(l)...
        ')*elastodata(:,:,k-(' num2str(middleVal-l+1) '))+'];
end
timeSmooth = [timeSmooth(1:end-1) ';'];

%Compute gaussian or average weight for frames
if strcmp(smoothweight,'gauss')
    weight = gausswin(nframes)/sum(gausswin(nframes));
elseif strcmp(smoothweight,'average')
    weight = ones(nframes)/sum(ones(nframes));
else
    error('Use gauss or average for smoothing weight of frames')
end

%Persistence value for frames at the very beginning or very end of sequence
perVal = 0.35;

for k=1:frames

    for iteration=1:iterations

        %Assign value to first frame of sequence
        if k==1
            img = elastodata(:,:,k,iteration);

        %Time smoothing over several frams
        elseif k > middleVal
            %Frames at very end of sequence
            if k > frames-middleVal
                img_k_1 = elastodata(:,:,k-1,iteration);
                img = (1-perVal)*img + perVal*img_k_1;

            %Execute time smoothing statement for all other frames
            else
                eval(timeSmooth)
            end
```

```
162
163             %Frames at very beginning of sequence
164         else
165             img_k_1 = elastodata(:,:,k-1,iteration);
166             img = (1-perVal)*img + perVal*img_k_1;
167         end
168
169         %Spatial smoothing
170         if strcmp(kernel,'median')
171             img = medfilt2(img,medsize);
172         else
173             img = conv2(img,mask,'same');
174         end
175
176         %Store result
177         elastodata(:,:,k,iteration) = img;
178
179     end
180 end
```

Bibliography

[1] Brian Stephen Garra. Imaging and estimation of tissue elasticity by ultrasound. *Ultrasound Quarterly*, 23(4):255–68, December 2007. PMID: 18090836.

[2] CIRS Model 049 elasticity phantom. http://www.cirsinc.com/049_ultra.html.

[3] P J Frinking, A Bouakaz, J Kirkhorn, F J Ten Cate, and N de Jong. Ultrasound contrast imaging: current and new potential methods. *Ultrasound in Medicine & Biology*, 26(6):965–975, July 2000. PMID: 10996696.

[4] S.P. Nasholm, R. Hansen, S.-E. Masoy, T.F. Johansen, and B.A.J. Angelsen. Transmit beams adapted to reverberation noise suppression using dual-frequency SURF imaging. *Ultrasonics, Ferroelectrics and Frequency Control, IEEE Transactions on*, 56(10):2124–2133, 2009.

[5] CIRS Model 050 nearfield phantom. http://www.cirsinc.com/050_ultra.html.

[6] John Cameron Reviewer. Physical properties of tissue. a comprehensive reference book, edited by francis a. duck. *Medical Physics*, 18(4):834, July 1991.

[7] I Edler. Early echocardiography. *Ultrasound in Medicine & Biology*, 17(5):425–431, 1991. PMID: 1962345.

[8] M.K. Eyer, M.A. Brandestini, D.J. Phillips, and D.W. Baker. Color digital echo/doppler image presentation. *Ultrasound in Medicine & Biology*, 7(1):21–31, 1981.

[9] J. Murphy. Down into the deep. *Time*, 128:48–54, August 1986.

[10] B Ward, A C Baker, and V F Humphrey. Nonlinear propagation applied to the improvement of resolution in diagnostic medical ultrasound. *The Journal of the Acoustical Society of America*, 101(1):143–154, 1997. PMID: 9000731.

[11] M.A. Averkiou, D.N. Roundhill, and J.E. Powers. A new imaging technique based on the nonlinear properties of tissues. In *Ultrasonics Symposium, 1997. Proceedings., 1997 IEEE*, volume 2, pages 1561–1566 vol.2, 1997.

[12] W.A.D Anderson. *Pathology*. CW Mosby Co., St. Louis, 1953.

[13] H E V Gierke, H L Oestreicher, E K Franke, H O Parrack, and W W V Wittern. Physics of vibrations in living tissues. *Journal of Applied Physiology*, 4(12):886–900, June 1952. PMID: 14946086.

[14] K.J. Parker, S.R. Huang, R.A. Musulin, and R.M. Lerner. Tissue response to mechanical vibrations for "sonoelasticity imaging". *Ultrasound in Medicine & Biology*, 16(3):241–246, 1990.

[15] R M Lerner, S R Huang, and K J Parker. "Sonoelasticity" images derived from ultrasound signals in mechanically vibrated tissues. *Ultrasound in Medicine & Biology*, 16(3):231–239, 1990. PMID: 1694603.

[16] J Ophir, I Céspedes, H Ponnekanti, Y Yazdi, and X Li. Elastography: a quantitative method for imaging the elasticity of biological tissues. *Ultrasonic Imaging*, 13(2):111–134, April 1991. PMID: 1858217.

[17] Ophir J., Cespedes I., Garra B., Ponnekanti H., Huang Y., and Maklad N. Elastography: ultrasonic imaging of tissue strain and elastic modulus in vivo. *European Journal of Ultrasound*, 3:49–70, 1996.

[18] L S Wilson and D E Robinson. Ultrasonic measurement of small displacements and deformations of tissue. *Ultrasonic Imaging*, 4(1):71–82, 1982. PMID: 7199773.

[19] Joel E Lindop, Graham M Treece, Andrew H Gee, and Richard W Prager. Phase-based ultrasonic deformation estimation. *IEEE Transactions on Ultrasonics, Ferroelectrics, and Frequency Control*, 55(1):94–111, 2008. PMID: 18334317.

[20] L Sandrin, S Catheline, M Tanter, X Hennequin, and M Fink. Time-resolved pulsed elastography with ultrafast ultrasonic imaging. *Ultrasonic Imaging*, 21(4):259–272, October 1999. PMID: 10801211.

[21] Gabriel Montaldo, Mickaël Tanter, Jérémy Bercoff, Nicolas Benech, and Mathias Fink. Coherent plane-wave compounding for very high frame rate ultrasonography and transient elastography. *IEEE Transactions on Ultrasonics, Ferroelectrics, and Frequency Control*, 56(3):489–506, March 2009. PMID: 19411209.

[22] J Bercoff, S Chaffai, M Tanter, L Sandrin, S Catheline, M Fink, J L Gennisson, and M Meunier. In vivo breast tumor detection using transient elastography. *Ultrasound in Medicine & Biology*, 29(10):1387–1396, October 2003. PMID: 14597335.

[23] Jérémy Bercoff, Mickaël Tanter, and Mathias Fink. Supersonic shear imaging: a new technique for soft tissue elasticity mapping. *IEEE Transactions on Ultrasonics, Ferroelectrics, and Frequency Control*, 51(4):396–409, April 2004. PMID: 15139541.

[24] A R Skovorda, A N Klishko, D A Gusakian, V D Ermilova, G A Oranskaia, and A P Sarvazian. Quantitative analysis of mechanical characteristics of pathologically altered soft biological tissues. *Biofizika*, 40(6):1335–1340, December 1995. PMID: 8590726.

[25] J. Ophir, B. Garra, F. Kallel, E. Konofagou, T. Krouskop, R. Righetti, and T. Varghese. Elastographic imaging. *Ultrasound in Medicine & Biology*, 26 Suppl 1:S23–9, May 2000. PMID: 10794867.

[26] Robert A Smith, Debbie Saslow, Kimberly Andrews Sawyer, Wylie Burke, Mary E Costanza, W Phil Evans, Roger S Foster, Edward Hendrick, Harmon J Eyre, and Steven Sener. American cancer society guidelines for breast cancer screening: update 2003. *CA: A Cancer Journal for Clinicians*, 53(3):141–169, June 2003. PMID: 12809408.

[27] Marcelo A Duarte, João C Machado, and Wagner C A Pereira. A method to identify acoustic reverberation in multilayered homogeneous media. *Ultrasonics*, 41(9):683–698, March 2004. PMID: 14996528.

[28] O. Standal, T.A. Tangen, and B.A.J. Angelsen. P2D-4 a phase based approach for estimation and tracking of locally variable delays. In *Ultrasonics Symposium, 2007. IEEE*, page 1583–1585, 2007.

[29] Jingdong Chen, Jacob Benesty, and Yiteng (Arden) Huang. Time delay estimation in room acoustic environments: An overview. *EURASIP Journal on Advances in Signal Processing*, 2006, 2006. Article ID 26503.

[30] Thor Andreas Tangen. Real time delay estimation and correction for a new dual frequency method in ultrasound imaging. *NTNU*, 2006.

[31] T A Krouskop, T M Wheeler, F Kallel, B S Garra, and T Hall. Elastic moduli of breast and prostate tissues under compression. *Ultrasonic Imaging*, 20(4):260–274, October 1998. PMID: 10197347.

[32] Liana Gheorghe, Speranta Iacob, and Cristian Gheorghe. Real-time sonoelastography - a new application in the field of liver disease. *Journal of Gastrointestinal and Liver Diseases: JGLD*, 17(4):469–74, December 2008. PMID: 19104713.

[33] Joel E Lindop, Graham M Treece, Andrew H Gee, and Richard W Prager. 3D elastography using freehand ultrasound. *Ultrasound in Medicine & Biology*, 32(4):529–545, April 2006. PMID: 16616600.

[34] E E Konofagou. Quo vadis elasticity imaging? *Ultrasonics*, 42(1-9):331–6, April 2004. PMID: 15047307.

[35] Jørgen Grythe. Improving elastography using SURF imaging for suppression of reverberations. Project thesis, NTNU, Trondheim, June 2009.

[36] Mathworks. http://www.mathworks.com/.

[37] Simon Perreault and Patrick Hébert. Median filtering in constant time. *IEEE Transactions on Image Processing: A Publication of the IEEE Signal Processing Society*, 16(9):2389–2394, September 2007. PMID: 17784612.

[38] R Hansen and B J Angelsen. SURF imaging for contrast agent detection. *IEEE Transactions on Ultrasonics, Ferroelectrics, and Frequency Control*, 56(2):280–90, February 2009. PMID: 19251515.

[39] Francis A Duck. Nonlinear acoustics in diagnostic ultrasound. *Ultrasound in Medicine & Biology*, 28(1):1–18, 2002. PMID: 11879947.

[40] Robert T. Beyer. Parameter of nonlinearity in fluids. *The Journal of the Acoustical Society of America*, 32(6):719–721, June 1960.

[41] S.-E. Masoy, O. Standal, P. Nasholm, T.F. Johansen, B. Angelsen, and R. Hansen. SURF imaging: In vivo demonstration of an ultrasound contrast agent detection technique. *Ultrasonics, Ferroelectrics and Frequency Control, IEEE Transactions on*, 55(5):1112–1121, 2008.

[42] Myra K Feldman, Sanjeev Katyal, and Margaret S Blackwood. US artifacts. *Radiographics: A Review Publication of the Radiological Society of North America, Inc*, 29(4):1179–1189, August 2009. PMID: 19605664.

[43] SonixRP. http://ultrasonix.com/products/rp.php.